

**Modeling charge transport induced
phenomena in colloidal double quantum
dots and developing new probes for
inter-dot interactions**

Roni Pozner

**Modeling charge transport induced phenomena
in colloidal double quantum dots and developing
new probes for inter-dot interactions**

Research Thesis

In Partial Fulfillment of the Requirements for the
Degree of Doctor of Philosophy

Roni Pozner

Submitted to the Senate of the Technion - Israel
Institute of Technology

Tevet, 5776

Haifa

January, 2016

Acknowledgments

The research thesis was done under the supervision of Prof. Efrat Lifshitz and Prof. Uri Peskin in the Interdepartmental Program of the Nancy and Stephen Grand Technion Energy Program (GTEP).

This work was supported by the Grand Technion Energy Program (GTEP), and comprises part of The Leona M. and Harry B. Helmsley Charitable Trust reports on Alternative Energy series of the Technion, Israel Institute of Technology, and the Weizmann Institute of Science.” Joe Rosen Graduate Fellowship Fund. The generous financial help of the Technion, Schulich Faculty of Chemistry, The Lise Meitner - Minerva Center for Computational Chemistry, and the United States - Israel Binational Science Foundation (BSF) is gratefully acknowledged.

I would like to express my deepest gratitude to my advisors, Prof. Uri Peskin and Prof. Efrat Lifshitz for their continuous support, advice and guidance throughout my PhD research. I thank Prof. Uri Peskin for his personal attention and guidance, for his patience, wealth of knowledge, and for introducing me to the fascinating field of electronic transport. I thank Prof. Efrat Lifshitz for her guidance, encouragement and positive frame of mind and for introducing me to the field of colloidal quantum dots. It has been a great privilege to work alongside such an accomplished scientists.

Special thanks to my dear family and for Tanya Pismenyuk, my girlfriend, for all their love, support and patience. It is for you that I dedicate this thesis.

Publications, Conference talks and Poster presentation

1. "Vertical junction Si cells for concentrating photovoltaics", *R. Pozner, G. Segev, R. Sarfaty, A. Kribus, Y. Rosenwaks, Progress in Photovoltaics 20, 2, 197-208 (2012)*
2. "Charge Transport-Induced Recoil and Dissociation in Double Quantum Dots", *R. Pozner, E. Lifshitz, and U. Peskin, Nano Letters 14, 6244 (2014)*
3. "Negative Differential Resistance Probe for Interdot Interactions in a Double Quantum Dot Array", *R. Pozner, E. Lifshitz, and U. Peskin, The Journal of Physical Chemistry Letters 6, 1521 (2015)*
4. "Triple Quantum Dot NEMS Memory Device", *Roni Pozner, Efrat Lifshitz, Uri Peskin, Appl. Phys. Lett. 107, 113109 (2015)*
5. Conference Paper - "Vertical junction high-efficiency concentrator photovoltaic cells", *26th European Photovoltaic Solar Energy Conference and Exhibition, At Advanced Photovoltaics*
6. Conference Talk – *Zichron Yaakov - Student Presentation - Weizmann (2010)*
7. Conference Talk – *Frontiers in Molecular Sciences – Technion - Zichron Yaakov (2014)*
8. Conference Talk – *First Principles Molecular Dynamics for Multiple Electronic States – Technion (2014)*
9. Conference Talk – *The 9th Schulich Graduate Symposium on Chemistry – Technion (2015)*
10. Poster Presentation – *CCEAM - Quantum Dynamics in Molecular and Nano-Materials: Mechanisms and Functionality – Tel Aviv University (2013)*

-
11. Poster Presentation – *Atomic and Molecular Interactions – Gordon Research Conference – Stone Hill College, MA, USA (2014)*
 12. Poster Presentation – *The Betsheva de Rothschild Seminar on Molecular Electronics – Weizmann – Weizmann Institute of Technology, Jerusalem (2015)*

Contents

Acknowledgments	i
Publications, Conference talks and Poster presentation	ii
Contents	iii
List of Figures	vi
Abbreviations	viii
1 Abstract	1
2 Introduction	3
2.1 Reducing the dimensions of a semiconductor	3
2.2 Quantum confinement	6
2.3 Nanocrystal surface	7
2.4 Quantum dot clusters	8
3 Research Goals	12
4 The QME theory - general overview	14
5 Double Quantum Dot Model	22
6 Results	26
6.1 Charge Transport-Induced Recoil and Dissociation in Double Quantum Dots, Nanoletters, 14, 6244 (2014)	27
6.2 Negative Differential Resistance Probe for Interdot Interactions in a Dou- ble Quantum Dot Array, J. Phys. Chem. Lett, 6, 1521 (2015)	40
6.3 Triple Quantum Dot NEMS Memory Device (2015)	49
7 Results Clarifications and Extensions	55
7.1 Self consistent solution of QME with Canonical Classical Forces	55
7.2 Negative Differential Resistance - Further Derivations	58
7.3 NEMS Memory Device - Additional Discussions	59
8 Discussion	62
A Hamiltonian of a Double Quantum Dot with spin	68

B Hamiltonian Interactions	73
C Negative Differential Resistance	78
Bibliography	84

List of Figures

2.1	Left: Typical optical absorption spectra of GaAs layers placed between thick AlGaAs slabs representing excitations associated with the electron and hole, each in a distinguish n th bound state. The top curve, labeled $L_z = 4000\text{\AA}$, exhibit the bulk form behavior. The bottom layers, labeled $L_z = 210\text{\AA}$ and $L_z = 14\text{\AA}$, are associated with the GaAs thin layers and demonstrating the discrete transitions behavior. Right: Measured L_z versus the measured exciton energies. Each curve represent an excition energy in the respective n th bound state. A scheme of the experiment setup is presented. [1]	3
2.2	Schematic drawing to show the concept of quantum-confined system of different dimensionality [5]: (a) bulk semiconductors (3D); (b) thin film, layer structure, quantum well (2D); (c) linear chain structure, quantum wire (1D); (d) cluster, colloid, nanocrystal, quantum dot (0D). In the bottom, the corresponding density of states $[\Delta(E)]$ versus energy (E) diagram.	4
2.3	(A) Transmission electron microscopy (TEM) image of CdSe nanocrystals; (B) TEM image of cobalt nanocrystals; (C) TEM micrograph of an AB13 superlattice of gamma-Fe2O3 and PbSe nanocrystals [10].	5
2.4	Topographic and spectroscopic of PbSe QDs in a CdSe QD matrix: (A) large scale STM image of a hexagonally packed monolayer of CdSe QDs; (B) STM image of PbSe QDs (marked with black circles) dispersed in a matrix of CdSe QDs [11].	6
2.5	Left: Emission characteristics of QDs with different compositions and sizes. Right: Excitation (top) and emission (bottom) spectra of four CdSe/ZnS QDs of varying sizes [13].	7
2.6	Left: The structure of a quantum dot showing its three main features: core, shell and ligands. Right: PbS CQDs capped with oleic acid (OA). In the organic route, EDT substitutes the long OA ligands and binds to Pb2+ on the surface [15].	8
2.7	TEM images of projections of binary superlattices, self-assembled from different nanoparticles, and modeled unit cells of the corresponding three-dimensional structures (only part of the original results are shown here for brevity) [21].	9
2.8	Left: A Double Quantum Dot (DQD) structure fabricated using electron-beam lithography. The lines in the picture are metallic contacts placed on a semiconductor substrate, defining the DQD structure in the center and two quantum point contacts flanking it. Right: An STM tip-DQD-surface setup scheme using CQDs synthesis for inducing motion and for measuring the forces inside the DQD, controlled by the organic ligands.	11

7.1	The diagonal red terms are adiabatic force terms and the non-diagonal blue terms are non-adiabatic force terms.	56
7.2	Current as a function of interdot distance, q_0 , and bias potentials Φ for an asymmetric (top) and symmetric (bottom) configurations. The colored regions highlight the writing and reading voltage margins for different ligands length which are reflected in q_0 . The white parts are non-operational regions.	60
7.3	The interdot distance (in nm) as a function of asymmetry, $E_A - E_B$ and bias potential. The dark red region indicates switching between a DQD to a SQD configuration under the appropriate lead, for $q_0 = 5nm$	61

Abbreviations

QME	Q uantum M aster E quation
CQD	C olloidal Q uantum D ots
NEMS	N ano E lectro M echanical S ystems
DQD	D ouble q uantum d ot
STM	S canning T unneling M icroscopy
STS	S canning T unneling S pectroscopy
NDR	N egative D ifferential R esistance
NVM	N onvolatile M emory
TQD	T riple Q uantum D ot
FQD	F loating Q uantum D ot
BQD	B ound Q uantum D ot
MBE	M olecular B eam E pitaxy
TEM	T ransmission E lectron M icroscopy
SQD	S ingle Q uantum D ot
SVD	S ingular V alue D ecompoistion
RAM	R andom A ccess M emory
VLSI	V ery L arge S Scale I ntegrated C ircuit
CMOS	C omplementary M etal- O xide- S emiconductor
FET	F ield E ffect T ransistor
CNT	C arbon N anotube
FEM	F inite E lement A nalysis

Chapter 1

Abstract

Colloidal quantum dots (CQDs) are free-standing nanostructures surrounded by capping ligands with chemically tunable electronic properties. The properties of single CQD and the extent to which electrical and mechanical interactions between dots in an array are significant in relation to observed transport properties are highly important. However, it is difficult to assess those interactions because they are controlled by the dots surface chemistry and by the organic ligands that link between separate dots. To date only a few studies have accounted for the ligands structure at the atomistic level and their effect on the mechanical forces between dots was yet to be considered.

In this work, we consider a new scanning tunneling microscopy (STM) tip - double quantum dot (DQD) - surface setup, for measuring ligand-mediated effective interdot forces, for inducing motion of individual CQDs within an array, and for exploring the unique connectivity of this setup in which the tip is coupled to a single dot while the coupling to the surface is shared by two dots.

The theoretical analysis of the DQD structure within this setup reveals for the first time voltage-induced interdot recoil and dissociation of the dots with pronounced changes in the current. By considering realistic microscopic parameters, our approach enables correlating the onset of mechanical motion under bias voltage with the effective ligand-mediated binding forces. The analysis also reveals a unique negative differential resistance (NDR) effect attributed to destructive interference during charge transfer from the DQD to the surface electrode.

Finally we consider a novel concept of nano-electromechanical nonvolatile memory device incorporating a triple quantum dot (TQD) cluster. The device operation is based on the bias induced motion of a floating quantum dot (FQD) located between two bound quantum dots (BQD). The mechanical motion capability of the FQD is used for switching between two stable states, "ON" and "OFF" states, while the ligand-mediated effective interdot forces between the BQDs and the FQD serve to hold the FQD in each stable position under zero bias. Considering realistic microscopic parameters, our theoretical treatment of the TQD reveals the characteristics of the device. Based on this analysis, the operation frequency of the device is estimated to be higher than current non-volatile memory devices.

Chapter 2

Introduction

2.1 Reducing the dimensions of a semiconductor

About half a century ago, C. H. Henry proposed the idea of reducing the dimensions of semiconductor crystals in order to explore size effects and new electronic phenomena [1]. After many struggles, the first successful attempt was achieved in 1974, by using a fabrication methods based on Molecular Beam Epitaxy (MBE). In this experiment, very thin (100\AA) layers of GaAs, placed between very thick slabs of AlGaAs, has been grown (Figure 2.1, right).

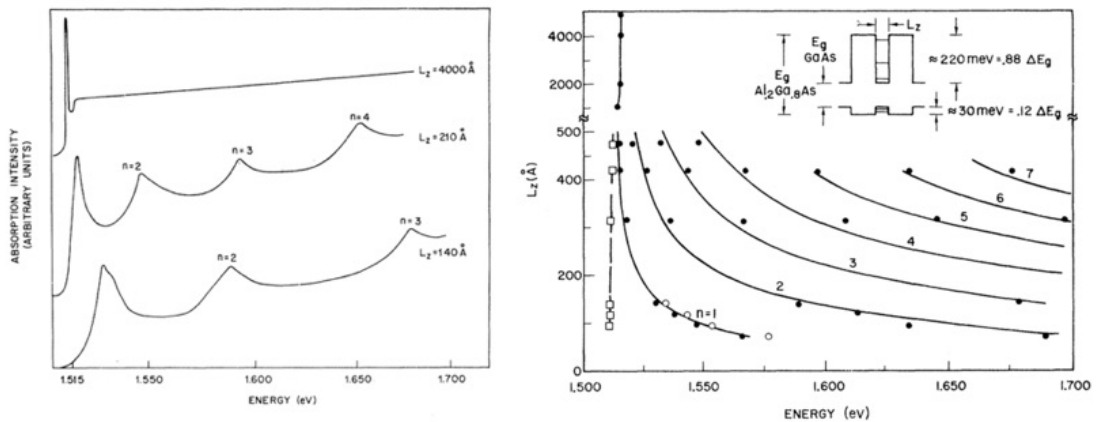


FIGURE 2.1: Left: Typical optical absorption spectra of GaAs layers placed between thick AlGaAs slabs representing excitations associated with the electron and hole, each in a distinguish n th bound state. The top curve, labeled $L_z = 4000\text{\AA}$, exhibit the bulk form behavior. The bottom layers, labeled $L_z = 210\text{\AA}$ and $L_z = 140\text{\AA}$, are associated with the GaAs thin layers and demonstrating the discrete transitions behavior. Right: Measured L_z versus the measured exciton energies. Each curve represent an excition energy in the respective n th bound state. A scheme of the experiment setup is presented.

[1]

These thin layers act as potential wells due to their small dimension and the difference of their bandgap in comparison with the slabs bandgap. In combination, these kind of structures confine the motion of free charges inside the middle layer in the direction which is normal to the growth orientation of the three layers. This one dimension confinement leads to the formation of a quantized energy spectrum which can be directly observed as optical transitions between the quantized states in an experiment (Figure 2.1, left).

The realization of quantum wells [1] gave strong boost to the research of confined systems. Soon enough, research was making strides into the realms of higher dimensionality confinement, with successful attempts in two dimensions confinement (quantum wires [2, 3]) and three-dimensional confinement (quantum dots). In 1981, Ekimov and Onushchenko [4] wrote: "In this letter we report the discovery and a spectroscopic study of a new class of objects that exhibit size effects: three-dimensional microscopic crystals of semiconducting compounds grown in a transparent dielectric matrix." And with this discovery they initiated a new area of full three-dimensional confinement nano-science. Figure 2.2 gives an illustration of the three confinement regimes [5].

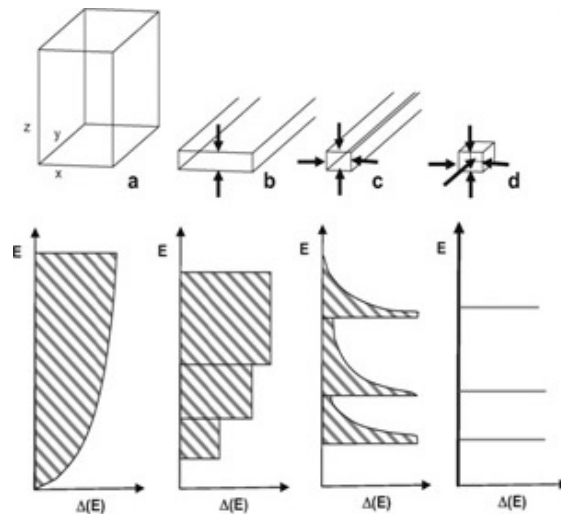


FIGURE 2.2: Schematic drawing to show the concept of quantum-confined system of different dimensionality [5]: (a) bulk semiconductors (3D); (b) thin film, layer structure, quantum well (2D); (c) linear chain structure, quantum wire (1D); (d) cluster, colloid, nanocrystal, quantum dot (0D). In the bottom, the corresponding density of states $[\Delta(E)]$ versus energy (E) diagram.

Few years later, A. Ekimov, L. Brus and Al. Efros [6] started pioneering work on what has become the field of colloidal quantum dots (CQDs). CQDs are semiconductor nanoparticles that are formed of few hundreds to few thousands of atoms. Unlike QDs fabricated using self-assembled growth of QDs by MBE [7], CQDs are synthesized from

precursor compounds dissolved in solutions, much like traditional chemical processes. Since the first synthesis of nearly monodisperse quantum dots in 1983, a lot of progresses have been made, and today CQDs can be synthesized using modern fabrication techniques with atomic precision having size control of tens to hundreds of Angstroms and size dispersion of a few percent [8]. Today, the level of chemical manipulation of CQDs is almost approaching that of regular molecules [9]. Transmission Electron Microscopy (TEM) [10] and Scanning Tunneling Microscope (STM) [11] images of CQDs layers are shown as an example in Figure 2.3 and Figure 2.4 respectively.

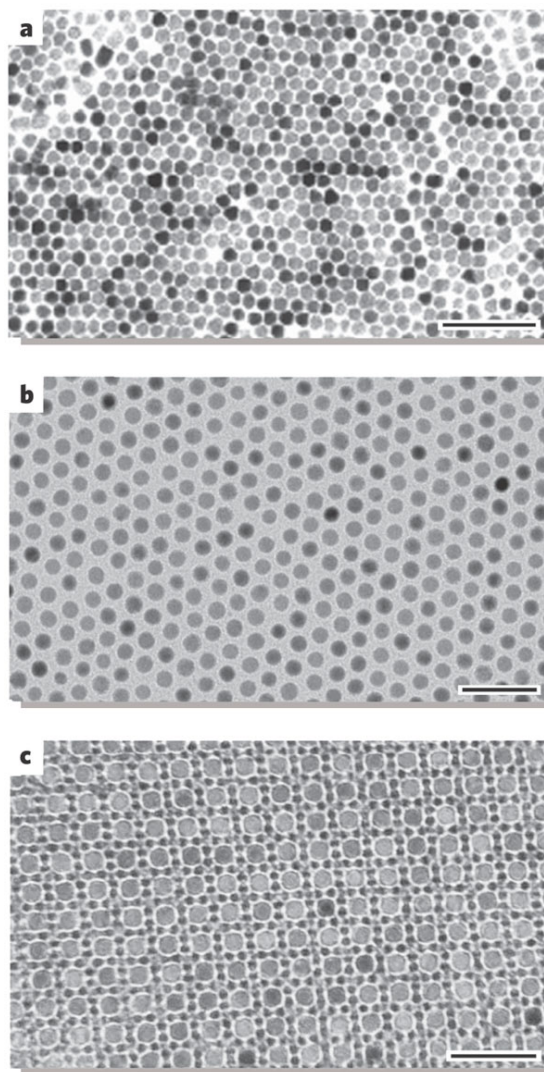


FIGURE 2.3: (A) Transmission electron microscopy (TEM) image of CdSe nanocrystals; (B) TEM image of cobalt nanocrystals; (C) TEM micrograph of an AB13 superlattice of gamma-Fe₂O₃ and PbSe nanocrystals [10].

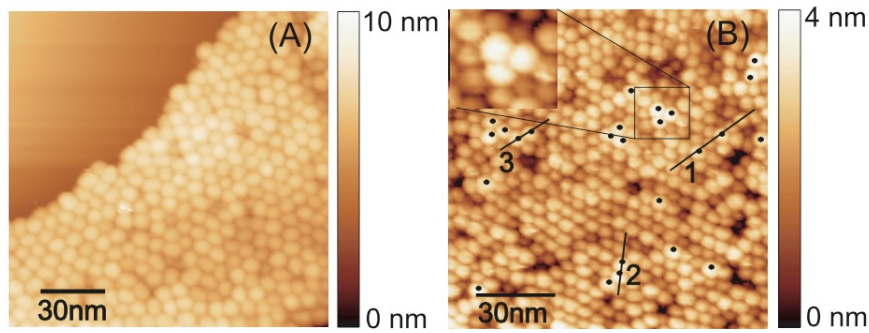


FIGURE 2.4: Topographic and spectroscopic of PbSe QDs in a CdSe QD matrix: (A) large scale STM image of a hexagonally packed monolayer of CdSe QDs; (B) STM image of PbSe QDs (marked with black circles) dispersed in a matrix of CdSe QDs [11].

2.2 Quantum confinement

The electronic properties of a semiconductor nanocrystal begin to deviate from the properties of the bulk form when the size of the nanocrystal is comparable to the typical de-Broglie wavelength of the charge carriers in the bulk. As a thought experiment, one can think of a nanocrystal as a particle-in-a-box model where the size reduction is manifested in the characteristic size of the box. In real materials, the de-Broglie lengths, in a good approximation, is of the order of the distance between quasi-electrons and holes in the bulk. This distance can vary from as low as 5.4 nm for GaAs nanocrystal, 24 nm for Si nanocrystal, to as high as 40nm for PbSe nanocrystal [12].

The change of the semiconductor size and composition bring about the build up of a quantized energy spectrum and in particular variation of the energy gap. It also leads to increased localization of the charge carriers and subsequently the development of additional kinetic energy of the carriers (Figure 2.5) [13]. This additional energy is the well-known confinement energy which results in further shifting of the quantized states to higher energies. Together, these phenomena represent the celebrated Quantum Size Effects and are responsible for the modified optical, electronic, chemical and thermodynamics properties [14] of the nanocrystal.

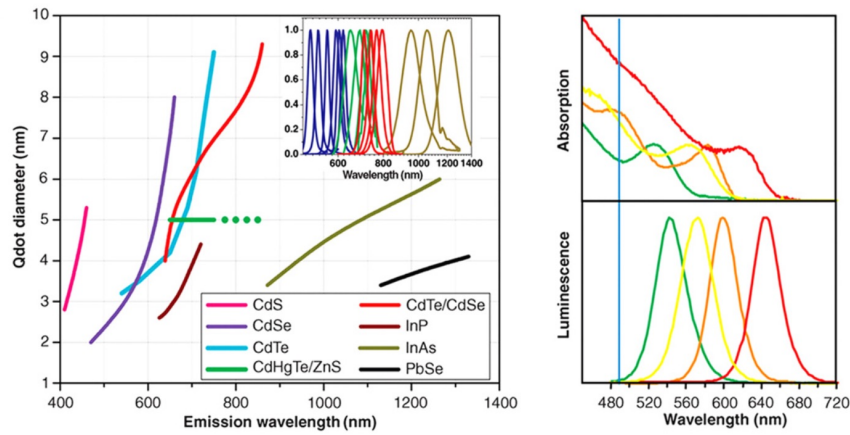


FIGURE 2.5: Left: Emission characteristics of QDs with different compositions and sizes. Right: Excitation (top) and emission (bottom) spectra of four CdSe/ZnS QDs of varying sizes [13].

These adjustable properties can be used for the engineering of optimized light emitters or light harvester, for use in state of the art applications. For example, the peak absorption wavelengths can be adjusted such that it will be correlated with the emission spectrum of the sun. This kind of optimization is carried out in a range of photovoltaic devices that are based on CQDs [12]. It is important to emphasize that the realization of these kind of applications could not take off at the level of understanding of a single nanocrystal, but rather by synchronized understanding of the mutual coupling between nanocrystals and the quantized spectrum in large nanocrystals cluster, and in particular the understanding of the nanocrystals surface passivation which controls this mutual coupling.

2.3 Nanocrystal surface

The importance of the nanocrystal surface becomes increasingly pronounced as the size of the nanocrystal is reduced. Whereas in bulk materials, the surface area constitutes only a very small fraction of the entire volume, in typical CQDs, the surface to volume ratio can reach tens of percent. Hence, a large fraction of the CQDs atoms are placed on the surface. These surface atoms constitute a serious problem because they are adding trap states inside the energy gap of the nanocrystal due to their unsaturated bonds. These trap states can influence negatively the desired properties of the nanocrystal such as the optical properties of a single nanocrystal [15, 16] or the transport properties of a

cluster of CQDs. In order to alleviate this problem, at least partially, the unsaturated bonds are partially passivated by organic ligand capping (Figure 2.6) [15],

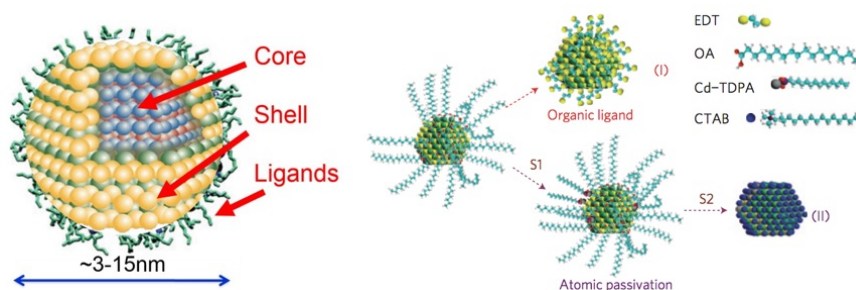


FIGURE 2.6: Left: The structure of a quantum dot showing its three main features: core, shell and ligands. Right: PbS CQDs capped with oleic acid (OA). In the organic route, EDT substitutes the long OA ligands and binds to Pb^{2+} on the surface [15].

Apart from relieving the effect of trapping, ligands of different lengths and building blocks can be engineered intelligently in order to optimize their other role as the connecting links between adjacent CQDs in a cluster [17]. This capability represents additional degree of freedom in terms of engineering of a cluster properties. Taking into account the possibility of ligands engineering in combination with quantum confinement effects, size-controlled electronic properties and chemical flexibility properties, CQDs can be thought of as artificial atoms whose properties can be engineered to suit a particular aim.

2.4 Quantum dot clusters

Using surface ligands [18–20], capped CQDs can be attached to each other, or can be incorporated into different types of organic and inorganic matrices. They can also be assembled into different types of ordered and disordered clusters, mimicking natural solids, forming granular materials, two-dimensional arrays, and three-dimensional clusters (Figure 2.7) [21].

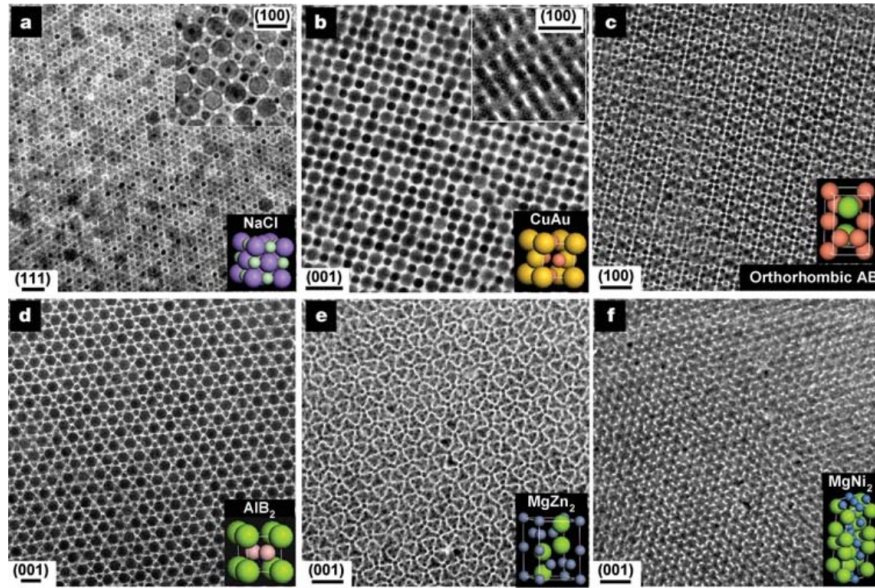


FIGURE 2.7: TEM images of projections of binary superlattices, self-assembled from different nanoparticles, and modeled unit cells of the corresponding three-dimensional structures (only part of the original results are shown here for brevity) [21].

Such CQDs clusters have the potential to initiate the development of new generation of devices. The number of teams in the world working on CQDs clusters and their applications is growing every year, with the first large scale productions in view. CQDs clusters can be used for applications utilizing single, double and triple quantum dot clusters [22] as well as building blocks for large clusters applications such as photovoltaic cells [12, 23–25], fluorescence imaging, light-emitting diodes [26, 27], lasers [28–31], and field-effect transistors [32–34].

Charge transport of CQDs in such clusters depend on the properties of single dots [35–40] as well as on chemical, electronic, magnetic and mechanical coupling between adjacent dots [17, 41]. And while mechanical coupling should not be manifested in rigid clusters made by lithography techniques, in which electron-beam lithography is used to write metal electrode structures that are used to define QDs in an underlying 2DEG heterostructure grown by MBE, CQDs clusters should in principle be influenced by mechanical forces between the CQDs themselves in both small and large clusters. Thus, deep understanding of the effect of mechanical coupling can lead to improvement of CQDs applications by either taking into account undesirable mechanical effect which can degrade the overall performance, or by exploiting these novel mechanical effects for the development of new class of applications.

Ligands should play a key role in characterizing mechanical forces between CQDs and between CQDs to surfaces, but unfortunately they are not easy to characterize and therefore not a lot is known about their influence on the general properties of CQDs clusters, and especially their effect on mechanical properties. Yet, the ability to manipulate the ligands using wet chemistry techniques [14] suggests that it is crucial to understand their mechanical characteristics.

Putting mechanical forces aside, studies on large clusters such as single layer CQDs films, modeled using well-established granular transport theories [42], have provided understanding of the collective transport phenomena using models such as Efros and Shklovskii Variable Range Hopping (ES-VRH) or Mott-VRH [42–45] with adjusted parameters which depends on the influence of temperature, dot sizes and material composition, nearest-neighbor hopping, activation energies, deviation from arrhenius behavior and more. Studies on small clusters such as double quantum dot (DQD) [46–48] and triple quantum dot (TQD) structures have also supplied a wealth of knowledge. The strong e-e interactions in such clusters give rise to a variety of intriguing phenomena of a prominent many-body nature such as NDR effects [49–56], Coloumb blockade [35, 36, 57, 58], Franck-Condon blockade [59, 60], Spin blockade [61–63] and Kondo effects [64–67].

CQDs have opened the possibility to study quantum transport effects under a controlled environment. Concurrently, in order to study and validate any of these quantum transport effects, strides in the computational costs efficiency and the accuracy of advanced transport theories had to be made. In this thesis our main aim is the study of mechanical forces and non-linear effects in a Double Quantum Dot structure [56, 68] (See Figure 2.8 for examples) using the Quantum Master Equation (QME) theorem [69].

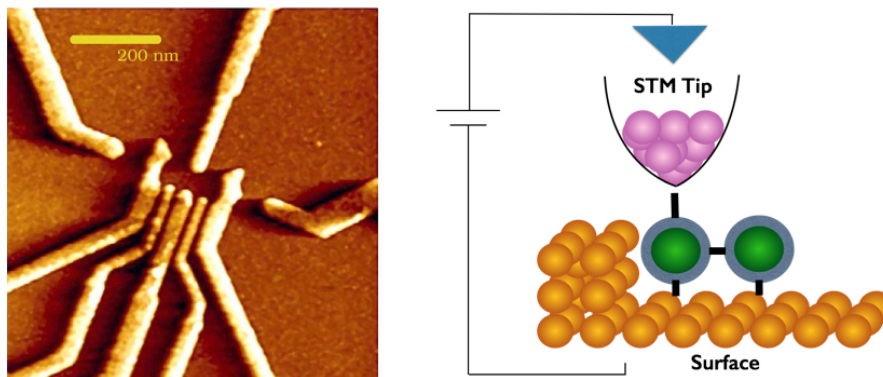


FIGURE 2.8: Left: A Double Quantum Dot (DQD) structure fabricated using electron-beam lithography. The lines in the picture are metallic contacts placed on a semiconductor substrate, defining the DQD structure in the center and two quantum point contacts flanking it. Right: An STM tip-DQD-surface setup scheme using CQDs synthesis for inducing motion and for measuring the forces inside the DQD, controlled by the organic ligands.

Chapter 3

Research Goals

The general purpose of the present research is to model charge transport induced phenomena in colloidal double quantum dots (CQD) and to develop new probes for inter-dot interactions. To achieve that, we apply the Quantum Master Equation theory for the investigation of the intertwined electronic and mechanical transport characteristics in small cluster of CQDs. The goals are outlined as follows:

1. **Proposal of a new STM tip-dot-substrate setup.** We construct a new setup for inducing mechanical motion of CQDs synthesized using "wet chemistry" techniques, and for characterizing the effective forces that control their mechanical response. Motion is induced and simultaneously evaluated by applying bias voltage and measuring the currents through coupled CQDs in this architecture.
2. **Mechanical recoil and dissociation.** Hardly anything is known about the mechanical coupling between CQDs and the role of the ligands in this context. Only a few studies account for their structure at the atomistic level, and their effect on the mechanical forces between dots was not yet considered. Our experimental setup allows to evaluate the mechanical strength between coupled QDs.
3. **The extent to which single dot properties and the interactions between dots in an array are of significance in relation to the observed transport properties.** The intermediate regime of several interacting CQDs in which specific interdot interactions could be manifested in transport measurements is studied. These transport properties are controlled by the surface chemistry of the dots and by the organic ligands that link between the dots.

4. Extension of single QD experimental studies to coupled QDs experiments.

The theoretical analysis demonstrates how a unique dark state and its related NDR phenomenon lead to a nonlinear feature in the current through the coupled QD, which can be used to reveal the magnitude of interdot electronic interactions. The study also demonstrates the possibilities for the construction of innovating NEMS devices by exploiting the combination of mechanical motion and electronic effects. It also emphasizes the unique versatilities of QDs and the surrounding ligands which can enable the realization of such class of devices.

Chapter 4

The QME theory - general overview

We study a model in which a DQD cluster is connected to two macroscopic electrodes. The full Hamiltonian of this system is defined in a full Hilbert space representing the entire system. In view of the very different physical nature of the DQD and the electrodes, it is convenient to divide the entire Hilbert space into three complementary parts, defined by appropriate projection operators. The identity operator in the full space is decomposed into three parts, spanned by orthogonal projections [69–71],

$$I = L + S + R; \quad L^2 = L, S^2 = S, R^2 = R; \quad LS = LR = RS = 0 \quad (4.1)$$

For example, we define the projector operators for a single particle Hilbert space (we later move to many-particle system) as:

$$L = \begin{pmatrix} 1_n & 0 & 0 \\ 0 & 0_m & 0 \\ 0 & 0 & 0_{N-m-n} \end{pmatrix}; S = \begin{pmatrix} 0_n & 0 & 0 \\ 0 & 1_m & 0 \\ 0 & 0 & 0_{N-m-n} \end{pmatrix}; R = \begin{pmatrix} 0_n & 0 & 0 \\ 0 & 0_m & 0 \\ 0 & 0 & 1_{N-m-n} \end{pmatrix} \quad (4.2)$$

Denoting the full Hamiltonian as H , 1_n is an $n \times n$ identity matrix and L projects onto the upper left $n \times n$ part of the Hamiltonian, S projects onto the middle $m \times m$ part of the Hamiltonian, and R projects onto the lower right $(N - m - n) \times (N - m - n)$ part

of the Hamiltonian. S defines the DQD subspace and L and R define the left and the right electrodes, respectively.

We can now write the full Hamiltonian expression as,

$$H = (L + S + R)H(L + S + R) = LHL + LHS + LHR + SHL + SHS + SHR + RHL + RHS + RHR. \quad (4.3)$$

By applying the assumption that the direct coupling between the two separate electrodes vanishes, i.e.,

$$(LHR)^\dagger = RHL = 0 \quad (4.4)$$

the exact Hamiltonian becomes,

$$H = LHL + SHS + RHR + (SHR + SHL + h.c.). \quad (4.5)$$

We can use the identity,

$$\Psi = (L + S + R)\Psi; \quad (4.6)$$

with the vector Ψ , for the eigenvalue problem,

$$H\Psi = E\Psi \quad (4.7)$$

to separate the set of coupled linear equations into three distinct sets,

$$\begin{aligned} LHL \cdot L\Psi + LHS \cdot S\Psi + 0 &= E \cdot L\Psi \\ SHL \cdot L\Psi + SHS \cdot S\Psi + RHS \cdot S\Psi &= E \cdot S\Psi \\ 0 + SHR \cdot S\Psi + RHR \cdot R\Psi &= E \cdot R\Psi \end{aligned} \quad (4.8)$$

and obtain the corresponding Hamiltonian matrix form,

$$H = \begin{pmatrix} LHL & LHS & 0 \\ SHL & SHS & SHR \\ 0 & RHS & RHR \end{pmatrix}. \quad (4.9)$$

Finally, we define the Hamiltonian as

$$H = H_L + H_R + (H_{LS} + H_{RS} + h.c.) + H_S. \quad (4.10)$$

where the external two electrodes are defined as,

$$H_L + H_R = LHL + RHR = \sum_{\sigma=\alpha,\beta} \sum_k \epsilon_{k,L} b_{k,L}^\dagger b_{k,L} + \sum_{\sigma=\alpha,\beta} \sum_k \epsilon_{k,R} b_{k,R}^\dagger b_{k,R} \quad (4.11)$$

and the electrodes-DQD coupling is,

$$H_{RS} + H_{LS} = SHR + SHL = \sum_{m,K} Z_{m,k,R} a_m^\dagger b_{k,R} + \sum_{m,K} Z_{m,k,L} a_m^\dagger b_{k,L} \quad (4.12)$$

$$Z_{m,k,J} = \langle \epsilon_m | H | \epsilon_{k,J} \rangle$$

$$a_m^\dagger b_{k,J} = |\epsilon_m\rangle \langle \epsilon_{k,J}|.$$

$Z_{m,k,J}$ is assumed to have a product form,

$$Z_{m,k,J} = \nu_{m,J} \cdot u_{k,J} \quad (4.13)$$

hence,

$$H_{RS} + H_{LS} = \left(\sum_{m=1}^M \nu_{m,R} a_m^\dagger \sum_k u_{k,R} b_{k,R} \right) + \left(\sum_{m=1}^M \nu_{m,L} a_m^\dagger \sum_k u_{k,L} b_{k,L} \right). \quad (4.14)$$

The many-particle system is characterized by creation and annihilation operators of an electron in the single particle states. a_i^\dagger and a_i ($a_i^\dagger, a_j = \delta_{i,j}$) create and annihilate an electron in the i^{th} spin-orbital, $|i\rangle \equiv |\phi_i\rangle \otimes |\sigma_i\rangle$, and $b_{k,J}^\dagger$ and $b_{k,J}$ create and annihilate an electron in electrode state $|\epsilon_{k,J}\rangle \otimes |\sigma_i\rangle$. The operators satisfy the common commutation relations for Fermions.

The full (non-relativistic) Hamiltonian for the many electron DQD reads (see Appendix A for the explicit derivation),

$$H_S = SHS = \sum_{i,j=1}^M \langle i | \hat{h} | j \rangle a_i^\dagger a_j + \sum_{i,j,k,l=1}^M \langle i, j | k, l \rangle a_i^\dagger a_j^\dagger a_l a_k. \quad (4.15)$$

and the coefficients have the following form,

$$\begin{aligned}\langle i|\hat{h}|j\rangle &= \delta_{\sigma_i,\sigma_j} \int d\mathbf{r} \phi_i^*(\mathbf{r}) \left[-\frac{\hbar^2}{2m_e} \nabla_{\mathbf{r}}^2 + V(\mathbf{r}) \right] \phi_j(\mathbf{r}) \\ \langle i,j|k,l\rangle &= \delta_{\sigma_i,\sigma_k} \delta_{\sigma_j,\sigma_l} \int d\mathbf{r}_1 \int d\mathbf{r}_2 \phi_i^*(\mathbf{r}_1) \phi_j^*(\mathbf{r}_2) \frac{Ke^2}{|\mathbf{r}_1 - \mathbf{r}_2|} \phi_k(\mathbf{r}_1) \phi_l(\mathbf{r}_2).\end{aligned}\quad (4.16)$$

Each electrode is regarded as an electron reservoir, represented as a grand-canonical ensemble. The electrode density, $\hat{\rho}_J$, is defined at thermal equilibrium as

$$\hat{\rho}_J = e^{-\frac{1}{K_B T} \sum_K (\epsilon_{k,J} - \mu_J) b_{k,J}^\dagger b_{k,J}} / \text{tr} \left[e^{-\frac{1}{K_B T} \sum_K (\epsilon_{k,J} - \mu_J) b_{k,J}^\dagger b_{k,J}} \right] \quad (4.17)$$

where T is the temperature, and μ_J is the electrochemical potential.

When the coupling is switched on, the DQD can exchange particles with the electrodes. Each electrode tends to drive the DQD to a different electronic population according to its macroscopic quasi-equilibrium state. Therefore the open DQD cluster reaches a non-equilibrium steady-state, in which the rate of charge transport (current) from one of the electrodes into the DQD, equals the rate of charge transport from the DQD into the other electrode. This current would remain constant as long as the bias (which depends on the temperature and the electrochemical potential) between the electrodes is fixed.

The steady-state of the DQD cluster is calculated by following the time-evolution of the system's full density matrix starting from an arbitrary initial state. Here we consider an initial density in a product form,

$$\hat{\rho}(0) = \hat{\rho}_S(0) \otimes \hat{\rho}_B(0); \hat{\rho}_B(0) = \hat{\rho}_R \otimes \hat{\rho}_L \quad (4.18)$$

where the bath density, ρ_B , satisfies the following properties,

$$\begin{aligned}[\hat{\rho}_B(0), \hat{H}_B] &= 0 \\ \text{tr}[\hat{\rho}_B(0), \hat{H}_{SB}] &= 0\end{aligned}\quad (4.19)$$

and $\hat{\rho}_S(0)$ is any normalized system density with $\text{tr}[\hat{\rho}_S(0)] = 1$, where $\text{tr}[\dots]$ denotes a trace over the DQD cluster subspace.

The time-evolution of the full density operator is given by the Liouville-von Neumann equation of motion,

$$\frac{d}{dt}\hat{\rho}(t) = -\frac{i}{\hbar}[\hat{H}, \hat{\rho}(t)]. \quad (4.20)$$

and the coupling between the DQD and the electrodes is assumed to be weak so that the perturbation to the DQD is small (a Markovian approximation). Following this assumptions, the well-known closed Redfield equation for $\hat{\rho}_S(t)$, can be derived [69],

$$\frac{d}{dt}\hat{\rho}_S(t) = -\frac{i}{\hbar}[\hat{H}, \hat{\rho}_S(t)] - \frac{1}{\hbar^2} \int_0^t dt' \text{tr}_B[\hat{H}_{SB}, [\hat{H}_{SB}(t-t'), \hat{\rho}_B(0)\hat{\rho}_S(t)]] \quad (4.21)$$

where

$$\begin{aligned} \hat{H}_{SB}(\tau) &\equiv e^{-\frac{i}{\hbar}(\hat{H}_S + \hat{H}_B)\tau} \hat{H}_{SB} e^{\frac{i}{\hbar}(\hat{H}_S + \hat{H}_B)\tau} \\ \hat{H}_{SB} &= \sum_{J=R,L} [\hat{V}_{S,J} \hat{U}_{B,J} + \hat{U}_{B,J}^\dagger \hat{V}_{S,J}^\dagger] \end{aligned} \quad (4.22)$$

or, more explicitly, by using the bath density operator (4.17) and the Fermion anti-commutation relations,

$$\begin{aligned} \frac{d}{dt}\hat{\rho}_S(t) &= -\frac{i}{\hbar}[\hat{H}_S, \hat{\rho}_S(t)] + \sum_{J=L,R} [\hat{F}_J(t)\hat{\rho}_S(t) - \hat{\rho}_S(t)\hat{F}_J^\dagger(t), \hat{V}_{S,J}] + h.c. \\ \hat{F}_J(t) &= \frac{1}{\hbar^2} \int_0^t d\tau C_J(\tau) \hat{V}_{S,J}^\dagger(\tau) \\ \hat{F}_J^\dagger(t) &= \frac{1}{\hbar^2} \int_0^t d\tau \tilde{C}_J(\tau) \hat{V}_{S,J}(\tau) \end{aligned} \quad (4.23)$$

where $C_J(\tau)$ and $\tilde{C}_J(\tau)$ are bath correlation functions,

$$\begin{aligned} C_J(\tau) &= \sum_K |u_{k,J}|^2 e^{-\frac{i}{\hbar}\epsilon_{k,J}\tau} [1 - f_J(\epsilon_{k,J})] \\ \tilde{C}_J(\tau) &= \sum_K |u_{k,J}|^2 e^{\frac{i}{\hbar}\epsilon_{k,J}\tau} [f_J(\epsilon_{k,J})]. \end{aligned} \quad (4.24)$$

Since \hat{H}_S commutes with the number operator, $\hat{N}_S = \sum_{m=1}^M a_m^\dagger a_m$, its eigenstates $\{|n\rangle\}$ are associated with well defined occupations of the single particle states,

$$\hat{H}_S |n\rangle = \epsilon_n |n\rangle; |n\rangle = \prod_{m=1}^M |n_m\rangle; \epsilon_n = \sum_{m=1}^M \epsilon_m n_m \quad (4.25)$$

where $|n_m\rangle$ denotes the occupation of the m state, with $n_m = 0$ or 1 .

Each diagonal matrix element of the reduced conductor density $[\hat{\rho}_S(t)]_{n,n'}$, represents the probability of electronic occupation at the state denoted as $|n\rangle$, where off-diagonal matrix elements represent coherences between different occupation states [69].

Finally we apply the "secular approximation" (neglecting the off-diagonal elements, i.e. ignoring the effect of the coherences on the population transfer) where the reduced density is restricted to a diagonal form (see additional discussion in section 6.1),

$$\begin{aligned} \frac{d}{dt}[\hat{\rho}_S(t)]_{n,n} &= \sum_{J=L,R} \sum_{l \neq n} [k_{l,n}^{(J)}(t) + \tilde{k}_{l,n}^{(J)}(t)][\hat{\rho}_S(t)]_{l,l} - [k_{n,l}^{(J)}(t) + \tilde{k}_{n,l}^{(J)}(t)][\hat{\rho}_S(t)]_{n,n} \\ k_{n,l}^{(J)}(t) &\equiv 2\text{Re}([\hat{V}_{S,J}]_{n,l}[\hat{F}_J(t)]_{l,n}) \\ \tilde{k}_{n,l}^{(J)}(t) &\equiv 2\text{Re}([\hat{V}_{S,J}^\dagger]_{n,l}[\hat{F}_J(t)]_{l,n}). \end{aligned} \quad (4.26)$$

Let us now consider the change in the charge on the conductor, $\frac{dQ_S}{dt} = 2e\text{tr}_S[\hat{N}_S \frac{d}{dt}\hat{\rho}_S(t)]$. Since the number operator, \hat{N}_S , is diagonal in the system Hamiltonian eigenstates representation,

$$\hat{N}_S|n\rangle = n|n\rangle; n = \sum_{m=1}^S n_m; N_S(t) = \text{tr}[\hat{N}_S \hat{\rho}(t)] \quad (4.27)$$

one has,

$$\frac{dQ_S}{dt} = 2e \sum_n [n \frac{d}{dt}\hat{\rho}_S(t)]_{n,n}. \quad (4.28)$$

Using eq. 4.23 for the change of electronic populations we obtain the following continuity equation for the flow of charge from the electrodes into the DQD cluster,

$$\frac{dQ_S}{dt} = I_R(t) + I_L(t) \quad (4.29)$$

where the transient current from the J^{th} electrode into the system is identified as,

$$I_J(t) = 2e \sum_n n \cdot \sum_{l \neq n} [k_{l,n}^{(J)}(t) + \tilde{k}_{l,n}^{(J)}(t)][\hat{\rho}_s(t)]_{l,l} - [k_{n,l}^{(J)}(t) + \tilde{k}_{n,l}^{(J)}(t)][\hat{\rho}_s(t)]_{n,n}. \quad (4.30)$$

The steady state is associated with the infinite time limit in which $\frac{dQ_s}{dt} = 0$, or,

$$I_{L \rightarrow R} = I_L(\infty) = -I_R(\infty) \quad (4.31)$$

and an explicit expression for the steady-state current can be obtained,

$$I_{L \rightarrow R} = 2e \sum_n n \cdot \underbrace{\sum_{l \neq n} [k_{l,n}^{(J)} + \tilde{k}_{l,n}^{(J)}(t)] [\hat{\rho}_s(t)]_{l,l} - [k_{n,l}^{(J)} + \tilde{k}_{n,l}^{(J)}] [\hat{\rho}_s]_{n,n}}_{K^{(J)} \hat{\rho}_s} \quad (4.32)$$

where the state-to-state rate constants are defined as,

$$\begin{aligned} k_{n,l}^{(J)} &= |[\hat{V}_{S,J}]_{n,l}|^2 \frac{\Gamma_{n,l}^{J,h}}{\hbar} \\ \tilde{k}_{n,l}^{(J)} &= |[\hat{V}_{S,J}^\dagger]_{n,l}|^2 \frac{\Gamma_{n,l}^{J,e}}{\hbar} \end{aligned} \quad (4.33)$$

$$\begin{aligned} \Gamma_{n,l}^{J,h} &= 2\pi \sum_k |u_{k,J}|^2 [1 - f_J(\epsilon_{k,J})] \delta(\epsilon_{k,J} - (\epsilon_n - \epsilon_l)) \\ \Gamma_{n,e}^{J,h} &= 2\pi \sum_k |u_{k,J}|^2 [f_J(\epsilon_{k,J})] \delta(\epsilon_{k,J} - (\epsilon_l - \epsilon_n)). \end{aligned} \quad (4.34)$$

We define $J_J(\epsilon)$, the continuous spectral density function,

$$J_J(\epsilon) = 2\pi |u_J(\epsilon)|^2 \rho_J(\epsilon) \quad (4.35)$$

for which $u_J(\epsilon_{k,J}) = u_{k,J}$, and $\rho_J(\epsilon) = \frac{dk_J}{d\epsilon_{k,J}} = \sum_k \delta(\epsilon - \epsilon_{k,J})$. Hence,

$$\begin{aligned} \Gamma_{n,l}^{J,h} &= [1 - f_J(\epsilon_n - \epsilon_l)] J_J(\epsilon_n - \epsilon_l) \\ \Gamma_{n,e}^{J,h} &= [f_J(\epsilon_l - \epsilon_n)] J_J(\epsilon_l - \epsilon_n). \end{aligned} \quad (4.36)$$

In this context, it is instructive to write a representative expression for the rate matrix $K^{(J)}$ (eq. 4.32). For the case of the DQD cluster, the rate matrix takes the following 4 by 4 matrix form,

$$K^{(J)} = \begin{bmatrix} -\sum_1^4 K_{n,1}^{(J)} & K_{1,2}^{(J)} & K_{1,3}^{(J)} & K_{1,4}^{(J)} \\ K_{2,1}^{(J)} & -\sum_1^4 K_{n,2}^{(J)} & K_{2,3}^{(J)} & K_{2,4}^{(J)} \\ K_{3,1}^{(J)} & K_{3,2}^{(J)} & -\sum_1^4 K_{n,3}^{(J)} & K_{3,4}^{(J)} \\ K_{4,1}^{(J)} & K_{4,2}^{(J)} & K_{4,3}^{(J)} & -\sum_1^4 K_{n,4}^{(J)} \end{bmatrix}. \quad (4.37)$$

Note that $[\hat{V}_{S,J}]_{n,l}$ vanishes identically, unless the state $|n\rangle$ has exactly one extra electron with respect to the state $|l\rangle$. Similarly, $[\hat{V}_{S,J}^\dagger]_{n,l}$ vanishes identically, unless the state $|n\rangle$ has exactly one less electron than the state $|l\rangle$. Therefore, $k_{n,l}^{(L)}$ and $\tilde{k}_{n,l}^{(L)}$ correspond to processes of single electron hopping from the DQD cluster to the (left) electrode and from the electrode to the cluster, respectively.

The electrodes in our model are modeled as semi-infinite linear chains [69]. Restricting the coupling between the electrode and the DQD subspace to a specific site, $|\chi_j^{(S)}\rangle$, $\hat{S}\hat{H}\hat{J} = \xi_J |\chi_1^{(S)}\rangle \langle \phi_1^{(J)}|$, the electrode-DQD coupling parameters take the form,

$$\begin{aligned} \nu_{m,J} &= \langle \epsilon_m | \chi_1^{(S)} \rangle \\ u_{k,J} &= \xi_J \langle \psi_1^{(J)} | \epsilon_{k,J} \rangle. \end{aligned} \quad (4.38)$$

Using an explicit form of the single particle electrode's eigenstates, the following is obtained,

$$u_J(\epsilon_{k,J}) = u_{k,J} = \xi_J \sqrt{\frac{2}{N+1}} \sin\left(\frac{k\pi}{N+1}\right) \quad (4.39)$$

and by using $\epsilon = \mu_J - 2|\beta_J| \cos[\frac{k\pi}{N+1}]$ (as derived for semi-infinite linear chains) for the corresponding single particle energy inside the band, $\rho_J(\epsilon) = \frac{dk}{d\epsilon} = \frac{N+1}{\pi} \frac{1}{\sqrt{4|\beta_J|^2 - (\epsilon - \mu_J)^2}}$, and $|u_J(\epsilon)|^2 = \frac{\xi_J^2}{2\beta_J^2(N+1)} [4\beta_J^2 - (\epsilon - \mu_J)^2]$, the final explicit form of the electrode's spectral density (eq. 4.35 and 4.36) in the band reads,

$$J_J(\epsilon) = 2\pi |u_J(\epsilon)|^2 \rho_J(\epsilon) = \frac{\xi_J^2}{\beta_J^2} \sqrt{4\beta_J^2 - (\epsilon - \mu_J)^2}. \quad (4.40)$$

Chapter 5

Double Quantum Dot Model

Considering the case of two (real) spatial orbital without spin, $i, j, k, l \in \{1, 2\}$, $\{\phi_1, \phi_2\} \in \mathbf{R}$, representing the Double Quantum Dot (DQD) cluster, the general case (eq. 4.15) reduces to (see Appendix A for the full derivation *including* Spin),

$$\hat{H} = E_1 d_1^\dagger d_1 + E_2 d_2^\dagger d_2 + t_{12} d_1^\dagger d_2 + t_{21} d_2^\dagger d_1 + (U_{12} - U_{ex}) d_1^\dagger d_1 d_2^\dagger d_2 \quad (5.1)$$

where E_1 and E_2 are the on-site energies of the left and right dots respectively, t is the hopping terms between the dots, and U_{12} , U_{ex} are the Coulomb and exchange interactions respectively. Our model consists of two Gaussian orbitals centered at \mathbf{R}_a and \mathbf{R}_b (in three dimensions),

$$\begin{aligned} \chi_a(\mathbf{r}) &= \left(\frac{\alpha}{\pi}\right)^{3/4} e^{-\frac{\alpha}{2}(\mathbf{r}-\mathbf{R}_a)^2} \\ \chi_b(\mathbf{r}) &= \left(\frac{\alpha}{\pi}\right)^{3/4} e^{-\frac{\alpha}{2}(\mathbf{r}-\mathbf{R}_b)^2} \end{aligned} \quad (5.2)$$

hence the DQD Hamiltonian in 5.1 is expressed in a localized sites representation. The "effective width" of each dot can be associated with the standard deviation σ parameter, where $\alpha = \frac{1}{2\sigma^2}$, and the corresponding overlap integral of the two Gaussian orbitals is,

$$\begin{aligned} S &= \int d\mathbf{r} \chi_a(\mathbf{r}) \chi_b(\mathbf{r}) = \int d\mathbf{r} \left(\frac{\alpha}{\pi}\right)^{3/4} e^{-\frac{\alpha}{2}(\mathbf{r}-\mathbf{R}_a)^2} \left(\frac{\alpha}{\pi}\right)^{3/4} e^{-\frac{\alpha}{2}(\mathbf{r}-\mathbf{R}_b)^2} \\ &= \int d\mathbf{r} \left(\frac{\alpha}{\pi}\right)^{3/2} e^{-\frac{\alpha}{4}(\mathbf{R}_a-\mathbf{R}_b)^2} e^{-\frac{\alpha}{2}(\mathbf{r}-[\mathbf{R}_a+\mathbf{R}_b]/2)^2} = e^{-\frac{\alpha}{4}(\mathbf{R}_a-\mathbf{R}_b)^2}. \end{aligned} \quad (5.3)$$

Without considering the details of the single particle Hamiltonian \hat{h} , we associate two of its eigenstates $i \in \{1, 2\}$ with orthonormal super positions of the two localized Gaussians

orbitals,

$$\begin{aligned}\phi_1(\mathbf{r}) &= c_{A1}\chi_a(\mathbf{r}) + c_{B1}\chi_b(\mathbf{r}) \\ \phi_2(\mathbf{r}) &= c_{A2}\chi_a(\mathbf{r}) + c_{B2}\chi_b(\mathbf{r})\end{aligned}\tag{5.4}$$

or in second quantization,

$$\begin{aligned}\hat{a}_1 &= c_{A1}\hat{d}_1 + c_{B1}\hat{d}_2 \\ \hat{a}_2 &= c_{A2}\hat{d}_1 + c_{B2}\hat{d}_2.\end{aligned}\tag{5.5}$$

Upon normalization of ϕ_1 and ϕ_2 , the coefficients take the following form,

$$\begin{aligned}c_{A1} &= \frac{a_1}{\sqrt{a_1^2 + b_1^2 + 2Sa_1b_1}}; c_{B1} = \frac{b_1}{\sqrt{a_1^2 + b_1^2 + 2Sa_1b_1}} \\ c_{A2} &= \frac{a_2}{\sqrt{a_1^2 + b_1^2 + 2Sa_1b_1}}; c_{B2} = \frac{b_2}{\sqrt{a_1^2 + b_1^2 + 2Sa_1b_1}}\end{aligned}\tag{5.6}$$

where orthogonally implies that,

$$\frac{b_2}{a_2} = \frac{1 + S\frac{b_1}{a_1}}{\frac{b_1}{a_1} + S}.\tag{5.7}$$

The expansion coefficients (a_1, a_2, b_1, b_2) and the single particle eigenvalues, ϵ_1 and ϵ_2 , are uniquely defined by solving the generalized eigenvalue problem [72], $[\mathbf{H} - \epsilon\mathbf{S}]\mathbf{C} = \mathbf{0}$, where \mathbf{H} is the single particle Hamiltonian matrix,

$$\mathbf{H} = \begin{pmatrix} E_1 & t(q) \\ t(q) & E_2 \end{pmatrix},$$

\mathbf{S} is the overlap matrix,

$$\mathbf{S} = \begin{pmatrix} 1 & S(q) \\ S(q) & 1 \end{pmatrix},$$

and \mathbf{C} is the expansion coefficients matrix,

$$\mathbf{C} = \begin{pmatrix} c_{A1} & c_{A2} \\ c_{B1} & c_{B2} \end{pmatrix}.$$

Notice that since \mathbf{H} and \mathbf{S} (or the single particle states $\phi_1(\mathbf{r})$ and $\phi_2(\mathbf{r})$) depend on the inter-dot distance, so do the single particle energies ϵ_1 and ϵ_2 as well as the expansion coefficients.

The orthonormal DQD orbitals (eq. 5.4) define an electronic Fock space, and the projection of the DQD Hamiltonian onto this space reads,

$$\hat{H} = \epsilon_1(q)a_1^\dagger a_1 + \epsilon_2(q)a_2^\dagger a_2 + (U_{12} - U_{ex})a_1^\dagger a_1 a_2^\dagger a_2 \quad (5.8)$$

where the single particle energies terms (eq. 4.16) are,

$$\begin{aligned} \epsilon_1 &= \int d\mathbf{r} \phi_1^*(\mathbf{r}) \left[-\frac{\hbar^2}{2m_e} \nabla_{\mathbf{r}}^2 + V(\mathbf{r}) \right] \phi_1(\mathbf{r}) \\ \epsilon_2 &= \int d\mathbf{r} \phi_2^*(\mathbf{r}) \left[-\frac{\hbar^2}{2m_e} \nabla_{\mathbf{r}}^2 + V(\mathbf{r}) \right] \phi_2(\mathbf{r}), \end{aligned} \quad (5.9)$$

the Coulomb and exchange interactions energy terms (eq. 4.16) are,

$$\begin{aligned} U_{12} &= \int d\mathbf{r}_1 \int d\mathbf{r}_2 \phi_1^*(\mathbf{r}_1) \phi_2^*(\mathbf{r}_2) \frac{Ke^2}{|\mathbf{r}_1 - \mathbf{r}_2|} \phi_1(\mathbf{r}_1) \phi_2(\mathbf{r}_2) \\ U_{ex} &= \int d\mathbf{r}_1 \int d\mathbf{r}_2 \phi_1^*(\mathbf{r}_1) \phi_2^*(\mathbf{r}_2) \frac{Ke^2}{|\mathbf{r}_1 - \mathbf{r}_2|} \phi_2(\mathbf{r}_1) \phi_1(\mathbf{r}_2). \end{aligned} \quad (5.10)$$

and the hopping term, t , equals zero. Pay attention that the Hamiltonian is represented in the eigenstates representation as opposed to the initial localized sites representation in eq 5.1.

Denoting the inter dot distance as $q = |\mathbf{R}_a - \mathbf{R}_b|$, we can obtain explicit expressions for the Coulomb integrals (eq. 5.10) as a function of q . (see Appendix B for the full derivation of all Coulomb integrals *including* spin)

$$\begin{aligned} U_{12}(q) &= \langle 1, 2 | 1, 2 \rangle = \\ &= \frac{Ke^2}{(a_1^2 + b_1^2 + 2Sa_1b_1)(a_2^2 + b_2^2 + 2Sa_2b_2)} \cdot \left[\sqrt{\frac{2\alpha}{\pi}} (a_1^2 a_2^2 + b_1^2 b_2^2 + 4a_1 a_2 b_1 b_2 e^{-\frac{\alpha}{2} q^2}) \right. \\ &+ \frac{\text{erf}[\sqrt{\frac{\alpha}{2}} q]}{q} (a_1^2 b_2^2 + b_1^2 a_2^2) + e^{-\frac{\alpha}{4} q^2} \frac{\text{erf}[\sqrt{\frac{\alpha}{2}} q/2]}{|q/2|} \\ &\left. \cdot [a_1^2 (a_2 b_2 + b_2 a_2) + b_1^2 (a_2 b_2 + b_2 a_2) + a_2^2 (a_1 b_1 + b_1 a_1) + b_2^2 (a_1 b_1 + b_1 a_1)] \right] \end{aligned} \quad (5.11)$$

$$\begin{aligned}
U_{ex}(q) = \langle 1, 2 | 2, 1 \rangle = & \\
& \frac{K e^2}{(a_1^2 + b_1^2 + 2S a_1 b_1)(a_2^2 + b_2^2 + 2S a_2 b_2)} \cdot \left[\sqrt{\frac{2\alpha}{\pi}} (a_1^2 a_2^2 + b_1^2 b_2^2 + (a_1 b_2 + a_2 b_1) e^{-\frac{\alpha}{2} q^2}) \right. \\
& \left. + \frac{\text{erf}[\sqrt{\frac{\alpha}{2}} q]}{q} 2(a_1 a_2 b_1 b_2) + e^{-\frac{\alpha}{4} q^2} \frac{\text{erf}[\sqrt{\frac{\alpha}{2}} q/2]}{|q/2|} [2(a_1 a_2 + b_1 b_2)(a_1 b_2 + b_1 a_2)] \right]. \quad (5.12)
\end{aligned}$$

Each of the 2 dots, represented by the single localized spin orbital, is modeled under the following assumptions: (i) Degeneracies of the neutral quantum dot orbitals are removed upon charging by an extra electron [73, 74], (ii) multiple charging of each dot is excluded due to intra-dot Coulomb interaction, (iii) spin is conserved during transport and a single spin model is sufficient. (iv) electronic interactions during double occupancy of each sub-system structure are fully accounted for, and (v) detailed structure of the electronic envelope functions, as well as the rapid oscillations associated with the semiconductor periodicity [75, 76], are disregarded but can be readily included for CQDs of specific shape and chemical compositions.

The DQD cluster is used in an STM tip-DQD-substrate architecture (Article 6.1, Figure 1) where the tip (T) and substrate (S) serve as the electrodes. The left dot is coupled to the tip and the surface while the right dot is coupled only to the surface. The STM setup is solve using the QME theorem presented in chapter 4. Pay attention to the unique connectivity in which the surface is shared by the two dots (unless stated otherwise explicitly).

Chapter 6

Results

Presented below are the following papers:

1. Charge Transport-Induced Recoil and Dissociation in Double Quantum Dots, *Nano Lett.*, 14, 6244 (2014).
2. Negative Differential Resistance Probe for Interdot Interactions in a Double Quantum Dot Array, *J. Phys. Chem. Lett.*, 6, 1521 (2015).
3. Triple Quantum Dot NEMS Memory Device *Appl. Phys. Lett.* (2015).

6.1 Charge Transport-Induced Recoil and Dissociation in Double Quantum Dots, Nanoletters, 14, 6244 (2014)

Charge Transport-Induced Recoil and Dissociation in Double Quantum Dots

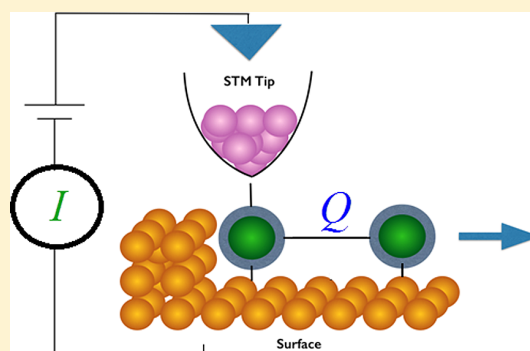
Roni Pozner,^{†,§,||} Efrat Lifshitz,^{†,§,||} and Uri Peskin^{*,†,‡,||}

[†]Schulich Faculty of Chemistry, [‡]the Lise Meitner Center for Computational Quantum Chemistry, [§]Solid State Institute, and ^{||}Russell Berrie Nanotechnology Institute, Technion-Israel Institute of Technology, Haifa 32000, Israel

Supporting Information

ABSTRACT: Colloidal quantum dots (CQDs) are free-standing nanostructures with chemically tunable electronic properties. This combination of properties offers intriguing new possibilities for nanoelectromechanical devices that were not explored yet. In this work, we consider a new scanning tunneling microscopy setup for measuring ligand-mediated effective interdot forces and for inducing motion of individual CQDs within an array. Theoretical analysis of a double quantum dot structure within this setup reveals for the first time voltage-induced interdot recoil and dissociation with pronounced changes in the current. Considering realistic microscopic parameters, our approach enables correlating the onset of mechanical motion under bias voltage with the effective ligand-mediated binding forces.

KEYWORDS: Colloidal quantum dots, double quantum dots, electromechanical response, charge transport, scanning tunneling microscopy



During past years, interest in colloidal quantum dots (CQDs)^{1,2} has increased dramatically, as they offer new propositions to a variety of applications such as electronic and light emitting devices,^{3,4} photovoltaic cells,^{5–7} and biological labeling.^{8,9} Unlike rigid structures made by lithography techniques,^{10,11} CQDs offer an intriguing possibility of inducing mechanical motion of the dots themselves on the nanoscale. This possibility was not yet explored because the mechanical forces between CQDs and between CQDs to surfaces are not easy to characterize, owing to the organic ligand capping that controls the interdot interactions. Yet, the ability to manipulate the ligands using “wet chemistry” techniques¹ suggests new possibilities for electromechanical devices that exploit the unique properties of capped CQDs.

Recent studies suggest that charge transport in granular materials, two-dimensional arrays, and three-dimensional assemblies¹² depends on the single CQDs properties as well as on their chemical, electronic, or magnetic coupling.¹³ Hardly anything is known about the mechanical coupling between CQDs. Ligands should play a key role in this context, but only a few studies account for their structure at the atomistic level,^{14–16} and their effect on the mechanical forces between dots was not yet considered.

In this work, we propose a new setup for inducing mechanical motion of CQDs and for characterizing the effective forces that control their mechanical response. The motion is induced and simultaneously evaluated by applying bias voltage and measuring the currents through coupled CQDs in a scanning tunneling microscopy (STM) tip–dot–substrate architecture. Charge transport through a single quantum dot

has already been characterized using scanning tunneling spectroscopy, revealing the discrete electronic levels structure^{17–19} and electron–phonon coupling.²⁰ Transport measurements through large quantum dots arrays^{21–25} revealed the importance of interdot interactions and order/disorder on the transport properties of such arrays. The intermediate regime of several interacting CQDs in which specific interdot interactions could be manifested in transport measurements was studied much less.

As a prototype system, we consider double quantum dot (DQD)^{26–28} structures in an STM tip–DQD–substrate architecture (see Figure 1). The model introduced below accounts explicitly for the dependence of electronic tunneling matrix elements and electronic correlation terms (Coulomb and exchange) on the distance between the dots and therefore elucidates the relation between electronic transport and mechanical motion within the DQD for parameters chosen in consistency with typical dimensions of CQDs structures. Using a mixed quantum-classical approach to the coupled electro-mechanical dynamics, we demonstrate correlation between the measured current and the mechanical motion, which enables to estimate the effective ligand-mediated force between the dots. For a given force, the applied voltage controls the mechanical response, which varies from voltage-induced recoil to DQD dissociation.

Received: July 8, 2014

Revised: September 22, 2014

Published: September 26, 2014



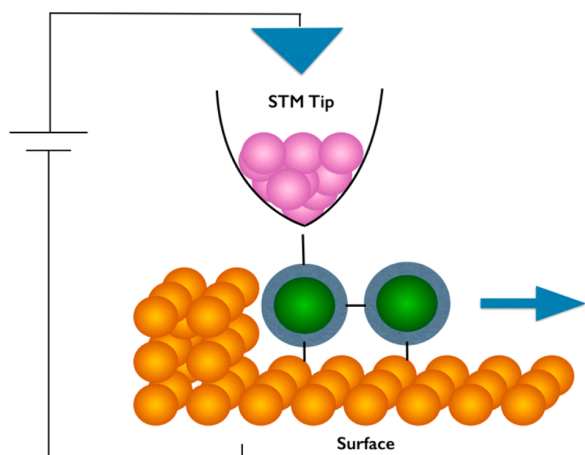


Figure 1. An STM tip–DQD–surface setup for inducing interdot motion and for measuring the interdot forces controlled by the organic ligands. The tip is coupled to one (immobile) dot that is coupled to a second (mobile) dot on the surface.

The model for the DQD assumes the following: Single electron charging of each dot is represented by occupation in a single spin orbital, localized on the dot, $\chi_A(\mathbf{r}) = (2\sigma^2\pi)^{-3/4}e^{-(r-R_A)^2/(4\sigma^2)}$ and $\chi_B(\mathbf{r}) = (2\sigma^2\pi)^{-3/4}e^{-(r-R_B)^2/(4\sigma^2)}$, where \mathbf{R}_A and \mathbf{R}_B are the center of mass coordinates of the dots and \mathbf{r} is the electronic coordinate. Hence, (i) degeneracies of the neutral quantum dot orbitals are removed upon charging by an extra electron;^{29,30} (ii) multiple charging of each dot is excluded due to intradot Coulomb interaction; (iii) spin is conserved during transport and a single spin model is sufficient; and (iv)

electronic interactions during double occupancy of the DQD structure are fully accounted for.

The detailed structure of the electronic envelope function, as well as the rapid oscillations associated with the semiconductor periodicity,^{31,32} are disregarded but can be readily included for CQDs of specific shape and chemical compositions. The dots' dimensions are captured in σ , the standard deviation of the respective probability distributions, $|\chi_{A/B}(\mathbf{r})|^2$. Setting, $\mathbf{R}_A \equiv (0,0,q/2)$, and $\mathbf{R}_B \equiv (0,0,-q/2)$, the interdot distance, $|\mathbf{R}_A - \mathbf{R}_B| = q$, defines the overlap between these two localized orbitals, $S(q) = \int d\mathbf{r} \chi_A(\mathbf{r})\chi_B(\mathbf{r}) = e^{-q^2/(8\sigma^2)}$, and the effective single electron Hamiltonian matrix in the basis of, $\chi_{A/B}(\mathbf{r})$, is assumed to be of a generic form,

$$H(q) = \begin{pmatrix} E_A & t_0 e^{-\gamma(q-q_0)} \\ t_0 e^{-\gamma(q-q_0)} & E_B \end{pmatrix}; \quad S(q) = \begin{pmatrix} 1 & S(q) \\ S(q) & 1 \end{pmatrix} \quad (1)$$

Therefore, E_A, E_B , are considered as the LUMO energies of the two separated dots at $q \rightarrow \infty$. (The choice $E_A \neq E_B$ accounts for differences between the dots owing to composition, size, shape, local external fields, etc.). The electronic coupling set by nanoparticle boundaries and the surrounding ligands^{1,33} is assigned a typical exponential decay form.

The mechanical forces binding the two dots are attributed to interligand and ligand-surface interactions. While the details of the interaction may strongly depend on these specificities, the mechanical contribution to the interdot interaction potential should reflect a universal short-range repulsion and a weak long-term attraction between the ligands. We therefore invoke a generic Morse potential, $V(q) = D(e^{-2\alpha(q-q_0)} - 2e^{-\alpha(q-q_0)} + 1)$, where D and α are respectively the interdot binding energy and

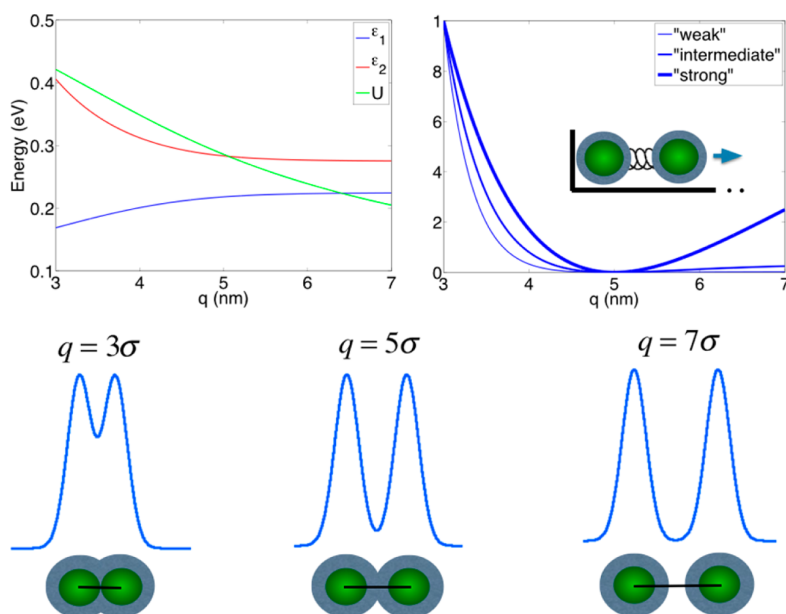


Figure 2. Left: The dependence of the DQD single particle energies ($\epsilon_1(q), \epsilon_2(q)$) and of the two particle repulsion, $U(q)$, on the interdot distance, q . The equilibrium interdot distance is $q_0 = 5\sigma$, which corresponds to an overlap integral, $S(q_0) = 0.044$. The Hamiltonian parameters were set to $E_A = E_B = 0.25$ eV, $t_0 = -0.01$ eV, and $\gamma = 0.4$ nm⁻¹, which correspond to an energy splitting, $\epsilon_1(q_0) - \epsilon_2(q_0) = 2(SE_A - t_0)/(1 - S^2) \sim 0.042$ eV, between the two DQD orbitals at the equilibrium geometry. Right: Three different interdot binding potentials with $V(q_0) = 0$ and $V(q_0 - 2\sigma) = 1$ eV. The different binding interactions are associated with $V(q_0 + 2\sigma) = 0.0025, 0.025, 0.25$ eV, as indicated on the plot. Bottom: Illustrative plots for the ligands-mediated electronic and mechanical interactions.

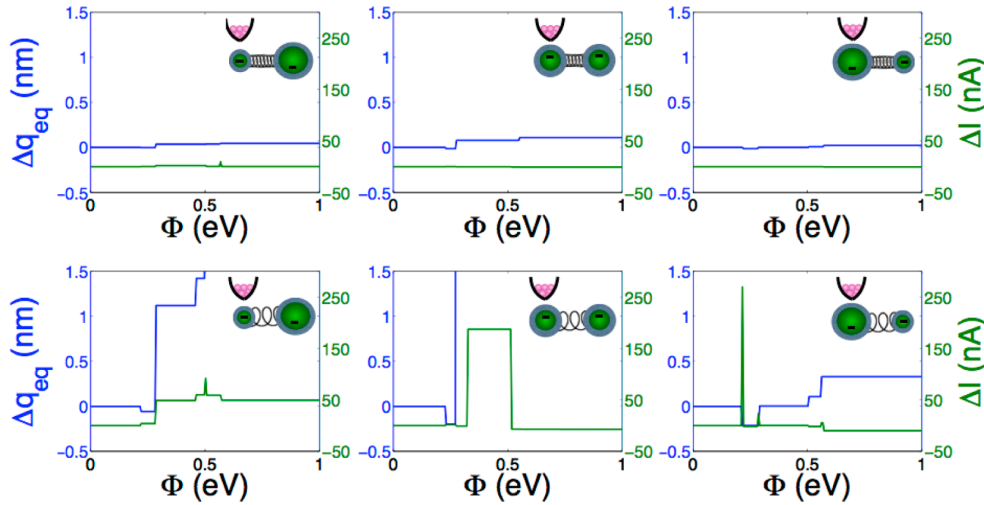


Figure 3. Changes of the interdot distance (Δq , blue) and the steady-state current (ΔI , green) in nonrigid DQDs with respect to their values in rigid DQDs, as functions of the applied bias voltage. Δq values larger than 1.5 nm (corresponding to DQD dissociation) are not included in the plot. The top and bottom rows correspond to strong and weak ligands-mediated interdot binding potential ($V(q_0 + 2\sigma) = 0.25, 0.0025$ eV, respectively). In each case, three DQDs of different asymmetry are considered. In the left column, the tip is positioned above the smaller of two dots, in the middle column, the two dots are identical, and in the right column, the tip is positioned above the larger of two dots ($E_A - E_B = -0.05, 0, 0.05$ eV, for left, middle, and right, respectively). The other model parameters are $\sigma = 1$ nm, $q_0 = 5\sigma$, $(E_A + E_B)/2 = 0.25$ eV, $t_0 = -0.01$ eV, and $\gamma = 0.4$ nm $^{-1}$, $\beta_T = \beta_S = 5$ eV, and $\xi_S = \xi_T = 0.05$ eV, $K_B T = 0.001$ eV, $\mu_S = 0$. Sharp spikes in ΔI are due to minor displacement of the transport channels thresholds (see Supporting Information).

interaction range parameters, which control the transition from “weak” to “strong” binding potentials (see Figure 2). q_0 is the equilibrium interdot distance.

Single particle energies as functions of the interdot distance, $\varepsilon_1(q)$, $\varepsilon_2(q)$, can be calculated using the standard linear variation principle,³⁴ $\det[H(q) - \varepsilon(q)S(q)] = 0$. The respective orthonormal DQD orbitals, $\varphi_1(q, r) = c_{A1}(q)\chi_A(r) + c_{B1}(q)\chi_B(r)$, and $\varphi_2(q, r) = c_{A2}(q)\chi_A(r) + c_{B2}(q)\chi_B(r)$, define an electronic Fock space, and the projection of the DQD Hamiltonian onto this space reads

$$\hat{H}_{\text{DQD}} = \varepsilon_1(q)a_1^\dagger a_1 + \varepsilon_2(q)a_2^\dagger a_2 + U(q)a_1^\dagger a_1 a_2^\dagger a_2 + \frac{p^2}{2\mu} + V(q) \quad (2)$$

a_m^\dagger is the creation operator for an electron in the m th orbital, μ is the reduced mass of the two dots, and p is the momentum associated with the interdot motion. Electronic coupling to this motion is inherent via the explicit dependence of the single electron energies and the electronic interaction term on q (see Figure 2 and Supporting Information). Notice that the DQD orbitals are superpositions of the localized functions that provide a convenient basis for interpretation (see below). The DQD is coupled to the STM tip (T) and to the surface (S), both regarded as reservoirs of noninteracting electrons,³⁵ $\hat{H}_{\text{leads}} = \sum_{K=T,S} \sum_{k \in K} \varepsilon_{k,K} b_{k,K}^\dagger b_{k,K}$ where $b_{k,K}^\dagger$ is the creation operators for an electron in the k th state of the K th reservoir. The coupling corresponds to electron hopping between the localized orbitals ($\chi_{A/B}(r)$) and the lead states, $\hat{H}_{\text{DQD-leads}} = \sum_{m=1,2} \sum_{k=T,S} \sum_{K \in K} u_{k,K} \eta_{n,K} d_n^\dagger b_{k,K}^\dagger + h.c.$ The annihilation operator of an electron at the n th dot orbital is d_n and $\eta_{n,K}$ equals one or zero if the K th lead is coupled or uncoupled to the n th dot, respectively (Figure 1 corresponds to $\eta_{1,T} = \eta_{1,S} = \eta_{2,S} = 1, \eta_{2,T} = 0$). The coupling parameters are associated with a semi elliptic band model with a bandwidth, $4\beta_K$, and a chemical potential, μ_K , where the spectral density reads,³⁶ $J_K(\varepsilon) =$

$2\pi \sum_{k \in K} |u_{k,K}|^2 \delta(\varepsilon - \varepsilon_{k,K}) = (\xi_K^2 / \beta_K^2) [4\beta_K^2 - (\varepsilon - \mu_K)^2]^{1/2}$. Notice that using the expansion of $\chi_{A/B}(r)$ in terms of the DQD orbitals, $\varphi_{1/2}(q, r)$, the coupling operator becomes q -dependent (see Supporting Information), $d_n = \sum_m D_{n,m}(q) a_m$. The full Hamiltonian finally reads

$$\hat{H} = \hat{H}_{\text{DQD}} + \hat{H}_{\text{leads}} + \hat{H}_{\text{DQD-leads}} \quad (3)$$

Considering typical quantum dot masses (10^5 – 10^6 amu) and the relevant values for the ligand-mediated interdot binding force constants (see below), the mechanical motion within the DQD can be treated classically, where q and p are the classical position and momentum, that is, $\dot{p} = -\langle d\hat{H}/dq \rangle$; $\dot{q} = \langle d\hat{H}/dp \rangle$, and $\langle \dots \rangle$ implies tracing over the electronic system density.^{37,38} For typical electronic tunneling barriers between the DQD and the STM tip and between the DQD and the surface, the dynamics of the DQD density can be approximated in the weak DQD-lead coupling limit, using the density matrix approach.^{36,39} The reduced DQD density is represented in the basis of \hat{H}_{DQD} eigenstates. Since \hat{H}_{DQD} commutes with the electronic number operator, each eigenstate is associated with occupation numbers of the DQD orbitals, $m, n \in 0, 1$, where, $\hat{H}_{\text{DQD}}(p, q) |mn\rangle = E_{mn}(p, q) |mn\rangle$, and the respective orbitals and orbital energies depend on the classical variables. The leads are assumed to maintain a quasi-equilibrium density, while the DQD system evolves according to the reduced Liouville equation to second order in the coupling to the leads. Notice that coherences between the DQD eigenstates should be insignificant at steady state in view of the relative eigenvalues separation and in view of the electronic interactions,²⁸ which is a source of decoherence when $U(q)$ exceeds the levels broadening by the DQD-leads coupling and the temperature. The effect of coupling to the leads therefore amounts to changes in the DQD eigenstate populations induced by electron hopping events,³⁶ $dP_{mn}(q, t)/dt = \sum_{m'n'} [k^{(S)} + k^{(T)}]_{mm'n'} P_{m'n'}(q, t)$. Here $P_{mn}(q, t)$ is the population of the respective eigenstate of the DQD Hamiltonian, and $[k^{(K)}]_{mm'n'}$

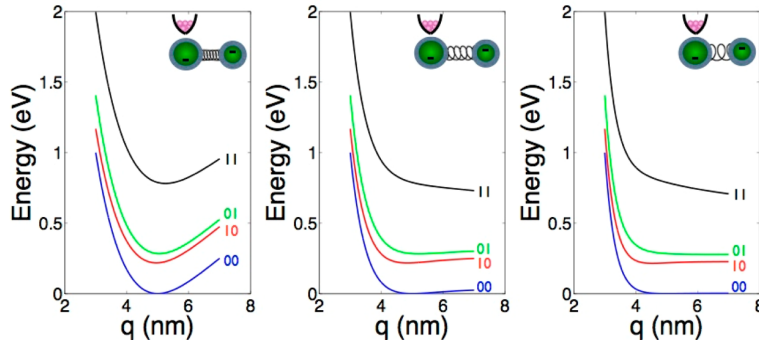


Figure 4. Eigen values of the interacting DQD Hamiltonian (BO potential energy surfaces for the mechanical motion) as functions of the interdot distance, q , in steady-state conditions ($p = 0$) for an asymmetric DQD ($E_A - E_B = 0.05$ eV). The left, middle, and right plots correspond to decreasing interdot ligand mediated binding interactions, that is, $V(q_0 + 2\sigma) = 0.25, 0.025, 0.0025$ eV, respectively. Each many-body eigenstate is marked according to the electronic occupation of the two DQD orbitals, “00”, “10”, “01”, “11” with the corresponding electronic energies: $0, \varepsilon_1, \varepsilon_2, \varepsilon_1 + \varepsilon_2 + U$.

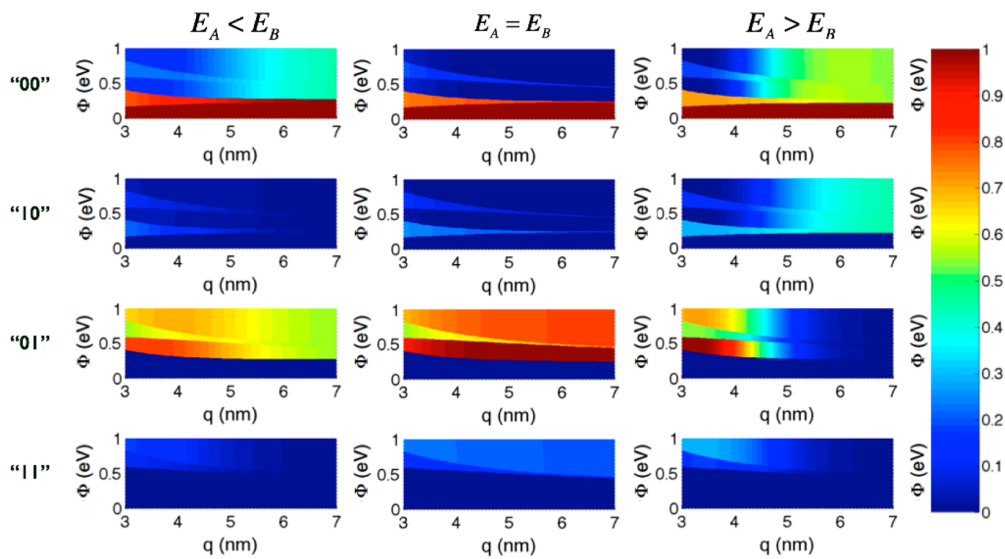


Figure 5. Steady-state populations (between zero and one, see color map) of electronic eigenstates versus the potential bias between the tip and the surface, and the (fixed) interdot distance, q . The left, middle, and right columns correspond to three DQDs of different asymmetry. In the left column, the tip is positioned above the smaller of two dots; in the middle column, the two dots are identical; and in the right column, the tip is positioned above the larger of two dots ($E_A - E_B = -0.05, 0, 0.05$ eV, for left, middle, and right, respectively). The four rows correspond to the different eigenstates of the DQD Hamiltonian “00”, “10”, “01”, “11”.

are rates of transitions induced by the K th lead,⁴⁰ $[k^{(K)}]_{mm,m'n'} = (1 - \delta_{mn,m'n'}) (\Gamma_{mn,m'n'}^{(K);h} + \Gamma_{mn,m'n'}^{(K);e}) - \delta_{mn,m'n'} \sum_{m'n' \neq m'n'} (\Gamma_{m'n',m'n'}^{(K);h} + \Gamma_{m'n',m'n'}^{(K);e})$, where $\Gamma_{mn,m'n'}^{(K);e/h} \equiv |[\sum_{j=1,2} \sum_i D_{ij} \Gamma_{1,k} a_j]_{mm,m'n'}|^2 f_e^{(K)}(E_{m'n'} - E_{mn}) / (E_{m'n'} - E_{mn})$ and $f_e^{(K)}(\varepsilon) = 1 / (1 + e^{(\varepsilon - \mu_S) / (k_B T)})$, and, $f_h^{(K)}(\varepsilon) = 1 - f_e^{(K)}(\varepsilon)$ are the Fermi distribution functions. Notice that the transition rate constants depend explicitly on the interdot distance via $D_{ij}(q)$ and $E_{mn}(p, q)$.

A steady-state response of the system to applied bias voltage between the tip and the substrate is associated with a self-consistent solution of the coupled electromechanical dynamical equations under the constraint, $\dot{q} = \dot{p} = \dot{P}_{00}(q, t) = \dot{P}_{10}(q, t) = \dot{P}_{01}(q, t) = \dot{P}_{11}(q, t) = 0$. These equations define the interdot distance and the current from the tip to the surface, $I_{T \rightarrow S}(q) = 2e \lim_{t \rightarrow \infty} \sum_{mm,m'n'} [k_{mm,m'n'}^{(T)}(q)] P_{m'n'}(q, t) N_{mm}$ where N_{mm} is the electrons number in the (nm) th DQD eigenstate. Notice that in principle there are multiple steady-state solutions. In particular, there is always a solution with $p = 0$ and $q \rightarrow \infty$ that corresponds to transport through a single dot. The results

below relate to the steady-state values of q , which are nearest to the equilibrium distance, q_0 .

The self-consistent electromechanical response of the DQD to an applied bias voltage is expressed in deviations of both the interdot distance, $\Delta q = q - q_0$, and the steady-state current, $\Delta I = I_{T \rightarrow S}(q) - I_{T \rightarrow S}(q_0)$, from their values for a rigid structure at $q = q_0$, as plotted in Figure 3 for different DQDs models (for the corresponding plots of the currents, $I_{T \rightarrow S}(q)$, see Supporting Information). For strong interdot binding interaction (top row), the changes in q are minor for any bias, regardless of the DQD symmetry (compare left, middle, and right plots in Figure 3). For weak binding (bottom row), the mechanical response becomes apparent where steps in Δq reflect the onset of charge transport channels,⁴¹ associated with the potential bias, $\mu_T - \mu_S = \varepsilon_1(q), \varepsilon_2(q), \varepsilon_1(q) + U(q), \varepsilon_2(q) + U(q)$. The respective changes in the interdot distances depend on the DQD symmetry (compare left, middle and bottom left plots) dissociation

of the DQD is observed after a certain critical voltage. Notice that the mechanical response is accompanied by apparent variations in the current, ΔI , where a dissociation of the DQD implies that the charge transport is essentially restricted to a single (immobile) dot between the tip and the surface (see scheme in Figure 1).

The response of the different DQDs to a bias can be rationalized using a Born–Oppenheimer (BO) picture.^{34,42} Indeed, neglecting coherences in the steady state (see above), the reduced system density matrix is diagonal in the basis of \hat{H}_{DQD} eigenstates, and the quantum mechanical trace gives

$$\begin{aligned} \dot{p} &= -\left\langle \frac{d}{dq} \hat{H} \right\rangle \\ &= -[P_{00}(q)E'_{00}(q) + P_{10}(q)E'_{10}(q) + P_{01}(q)E'_{01}(q) + P_{11}(q)E'_{11}(q)] \end{aligned} \quad (4)$$

where, $E_{00}(q) = V(q)$, $E_{10}(q) = V(q) + \varepsilon_1(q)$, $E_{01}(q) = V(q) + \varepsilon_2(q)$, and $E_{11}(q) = V(q) + \varepsilon_1(q) + \varepsilon_2(q) + U(q)$. The eigenvalues of \hat{H}_{DQD} for $p = 0$ define potential energy curves for the interdot mechanical motion (see an example in Figure 4), from which mechanical forces are derived. The net force is the average of these forces weighted according to the populations of the different many body eigenstates, $P_{mn}(q)$. For strong binding, all four potential curves are attractive. For intermediate binding the potential curve associated with the “11” state becomes repulsive (i.e., does not have a minimum for finite q) and for weak binding both the “01” and the “11” curves are repulsive. Mechanical recoil between the two dots becomes apparent when the averaged force is repulsive, due to population transfer into the repulsive states. Notice the two different contributions to the repulsion. The “01” state (see $\varepsilon_2(q)$ in Figure 2) is associated with single electron population in an “anti-bonding” DQD orbital, having a nodal plane between the dots centers, while the “11” state (which gets populated at higher bias voltages) is associated with an additional two-body (electrostatic) repulsion (see $U(q)$ in Figure 2).

Considering the different DQD structures, the strong mechanical response observed for weak binding in the cases $E_A < E_B$ (the tip is coupled to the smaller dot) and $E_A = E_B$ is indeed correlated with a relatively significant population of the repulsive electronic states (“01” and “11”), as demonstrated in the middle and left columns of Figure 5. In contrast, for $E_A > E_B$ where the tip is coupled to the larger dot, the mechanical response is insignificant, in accordance with low steady-state populations of the repulsive states. This is attributed to the small probability density of the antibonding orbital at the DQD–tip contact in this setup, which implies that charging the repulsive states from the tip is much slower than discharging them to the surface. We emphasize that the effective couplings of the DQD to the surface and the tip are different for the bonding and antibonding orbitals (see Figure 6 for an analogy with heuristic RC schemes). Our analysis shows that transport-induced recoil and/or dissociation requires that the contact resistance at the tip will not be much larger than the contact resistance at the surface for the antibonding orbital. A more detailed discussion of the dependence of the steady-state populations on particular DQD structure is beyond our scope here and will be given elsewhere.

In conclusion, a new setup is proposed for inducing controlled mechanical motions of CQDs on a surface and for extracting information on the elusive (hard to characterize) ligand-mediated effective interdot forces. The electromechan-

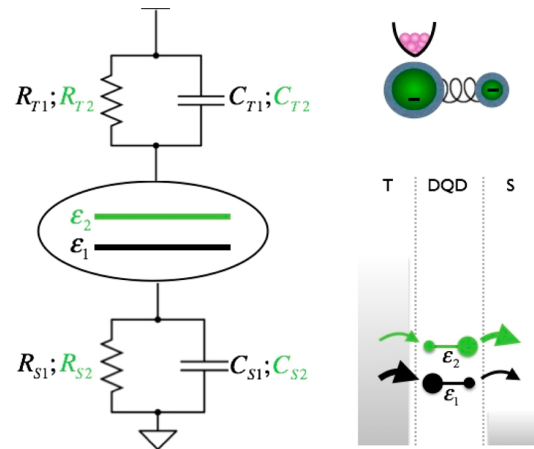


Figure 6. Left: A double-barrier tunneling junction model of the tip–DQD–surface system. Each one of the DQD orbitals ($n = 1, 2$) has a different effective resistance and capacitance at the contacts to the tip (R_{Tn}, C_{Tn}) and to the surface (R_{Sn}, C_{Sn}). The effective contact resistance increases as the probability density of the orbital decreases at that contact. When the tip is coupled to the larger dot (top right plot), the probability density of the antibonding orbital ($n = 2$) at the contact to the tip is small (as indicated by the relative sizes of the green circles at the bottom right plot), meaning $R_{S2}/R_{T2} \ll 1$. This results in low population of this orbital at steady state.

ical coupling is accounted for by considering explicitly the dependence of the electronic terms on the interdot distance. In particular, the single electron (tunneling) coupling and the many body (Coulomb and exchange) interaction terms are calculated self-consistently with the interdot mechanical response within a mixed quantum-classical reduced density matrix formulation. A Born–Oppenheimer interpretation of the steady-state response formulates the average electromechanical force in terms of specific forces attributed to specific electronic many-body states of the system, weighted by their steady-state populations.

Our model calculations suggest that charge transport can indeed induce mechanical recoil and/or dissociation of DQDs, and the calculations predict that dissociation should be observed when the interdot binding force constant is in the range, $K \equiv [(\partial^2 V)/(\partial q^2)]|_{q_0} \lesssim 10^{-2}$ N/m. Moreover, the dissociation should be reflected in apparent changes in the steady-state current through the DQD. Experimental realization of the proposed setup for inducing and measuring DQD dynamics is currently being examined. Different DQD structures can be formed either by a mutual push of individual QD with an AFM tip toward its neighbor, or by random dispersion on an appropriate substrate. A more elaborate account of the electronic and spatial structure of particular dots and interdot ligand-mediated binding needs to be included in future investigations using the methodology presented in this work in order to compare with specific experiments, to refine our understanding of transport and mechanical response on the nanoscale, and for the design of novel electromechanical devices.

■ ASSOCIATED CONTENT

Supporting Information

The explicit dependence of the electronic interaction and the DQD-leads coupling on the interdot distance is developed in Section A. The steady-state currents (I – V curves) calculated

through different nonrigid QDs are plotted in Section B. This material is available free of charge via the Internet at <http://pubs.acs.org>.

AUTHOR INFORMATION

Corresponding Author

*(U.P.) E-mail: uri@tx.technion.ac.il.

Notes

The authors declare no competing financial interest.

ACKNOWLEDGMENTS

Rainer Haertle is acknowledged for useful comments and discussions. This research was supported by the German Israeli Foundation Grant 1154-119.5/2011 (U.P.) and Grant I-1049-97.5 (E.L.), as well as by the European community FP7 NMP "SANS" project. R.P. acknowledges support by the Nancy & Stephan Grand Technion Energy Program (GTEP) center.

REFERENCES

- (1) Talapin, D. V.; Lee, J.-S.; Kovalenko, M. V.; Shevchenko, E. V. *Chem. Rev.* **2010**, *110*, 389.
- (2) Kim, J. Y.; Voznyy, O.; Zhitomirsky, D.; Sargent, E. H. *Adv. Mater.* **2013**, *25*, 4986.
- (3) Cho, K.-S.; Lee, E. K.; Joo, W.-J.; Jang, E.; Kim, T.-H.; Lee, S. J.; Kwon, S. J.; Han, J. Y.; Kim, B.-K.; Choi, B. L.; Kim, J. M. *Nat. Photonics* **2009**, *3*, 341.
- (4) Caruge, J. M.; Halpert, J. E.; Wood, V.; Bulovic, V.; Bawendi, M. G. *Nat. Photonics* **2008**, *2*, 247.
- (5) Nozik, A. J.; Beard, M. C.; Luther, J. M.; Law, M.; Ellingson, R. J.; Johnson, J. C. *Chem. Rev.* **2010**, *110*, 6873.
- (6) Kamat, P. V. *J. Phys. Chem. C* **2008**, *112*, 18737.
- (7) Barkhouse, D. A. R.; Debnath, R.; Kramer, I. J.; Zhitomirsky, D.; Pattantyus-Abraham, A. G.; Levina, L.; Etgar, L.; Grätzel, M.; Sargent, E. H. *Adv. Mater.* **2011**, *23*, 3134.
- (8) Alivisatos, P. *Nat. Biotechnol.* **2004**, *22*, 47.
- (9) Medintz, I. L.; Uyeda, H. T.; Goldman, E. R.; Mattoussi, H. *Nat. Mater.* **2005**, *4*, 435.
- (10) Michler, P. *Single Quantum Dots: Fundamentals, Applications and New Concepts*; Physics and Astronomy Online Library; Springer: New York, 2003.
- (11) Rodina, A. V.; Alekseev, A. Y.; Efros, A. L.; Rosen, M.; Meyer, B. K. *Phys. Rev. B* **2002**, *65*, 125302.
- (12) Shevchenko, E. V.; Talapin, D. V.; Kotov, N. A.; O'Brien, S.; Murray, C. B. *Nature* **2006**, *439*, 55.
- (13) Vanmaekelbergh, D.; Liljeroth, P. *Chem. Soc. Rev.* **2005**, *34*, 299.
- (14) Inerbaev, T. M.; Masunov, A. E.; Khondaker, S. I.; Dobrinescu, A.; Plamadă, A. V.; Kawazoe, Y. *J. Chem. Phys.* **2009**, *131*, 044106.
- (15) Morris-Cohen, A. J.; Malicki, M.; Peterson, M. D.; J. Slavin, W. J.; Weiss, E. A. *Chem. Mater.* **2012**, *25*, 1155.
- (16) Bealing, C. R.; Baumgardner, W. J.; Choi, J. J.; Hanrath, T.; Hennig, R. G. *ACS Nano* **2012**, *6*, 2118.
- (17) Overgaag, K.; Liljeroth, P.; Grandidier, B.; Vanmaekelbergh, D. *ACS Nano* **2008**, *2*, 600.
- (18) Nguyen, T. H.; et al. *Phys. Rev. B* **2011**, *84*, 195133.
- (19) Banin, U.; Cao, Y.; Katz, D.; Millo, O. *Nature* **1999**, *400*, 542.
- (20) Sun, Z.; Swart, I.; Delerue, C.; Vanmaekelbergh, D.; Liljeroth, P. *Phys. Rev. Lett.* **2009**, *102*, 196401.
- (21) Williams, K. J.; Tisdale, W. A.; Leschkes, K. S.; Haugstad, G.; Norris, D. J.; Aydil, E. S.; Zhu, X.-Y. *ACS Nano* **2009**, *3*, 1532.
- (22) Jdira, L.; Overgaag, K.; Gerritsen, J.; Vanmaekelbergh, D.; Liljeroth, P.; Speller, S. *Nano Lett.* **2008**, *8*, 4014.
- (23) Ou, Y.-C.; Wu, J.-J.; Fang, J.; Jian, W.-B. *J. Phys. Chem. C* **2009**, *113*, 7887.
- (24) Guyot-Sionnest, P. *J. Phys. Chem. Lett.* **2012**, *3*, 1169.
- (25) Mentzel, T. S.; Porter, V. J.; Geyer, S.; MacLean, K.; Bawendi, M. G.; Kastner, M. A. *Phys. Rev. B* **2008**, *77*, 075316.
- (26) van der Wiel, W. G.; Franceschi, S. D.; Elzerman, J. M.; Fujisawa, T.; Tarucha, S.; Kouwenhoven, L. P. *Rev. Mod. Phys.* **2002**, *75*, 1.
- (27) Fransson, J. *Phys. Rev. B* **2004**, *69*, 201304.
- (28) Härtle, R.; Cohen, G.; Reichman, D. R.; Millis, A. J. *Phys. Rev. B* **2013**, *88*, 235426.
- (29) Romero, H. E.; Drndic, M. *Phys. Rev. Lett.* **2005**, *95*, 156801.
- (30) Waugh, F. R.; Berry, M. J.; Mar, D. J.; Westervelt, R. M.; Campman, K. L.; Gossard, A. C. *Phys. Rev. Lett.* **1995**, *75*, 705.
- (31) Vaxenburg, R.; Lifshitz, E. *Phys. Rev. B* **2012**, *85*, 075304.
- (32) *Semiconductor Nanocrystals: From Basic Principles to Applications*; Ęfros, A. L., Lockwood, D. J., Tsybeskov, L., Eds.; Nanostructure Science and Technology; Springer: New York, 2003.
- (33) Talapin, D. V.; Murray, C. B. *Science* **2005**, *310*, 86.
- (34) Szabo, A.; Ostlund, N. S. *Modern Quantum Chemistry: Introduction to Advanced Electronic Structure Theory*; Dover Books on Chemistry Series; Dover Publications: Mineola, NY, 1996.
- (35) Meir, Y.; Wingreen, N. S.; Lee, P. A. *Phys. Rev. Lett.* **1993**, *70*, 2601.
- (36) Peskin, U. *J. Phys. B: At., Mol. Opt. Phys.* **2010**, *43*, 153001.
- (37) Brüggemann, J.; Weick, G.; Pistolesi, F.; von Oppen, F. *Phys. Rev. B* **2012**, *85*, 125441.
- (38) Dzhioev, A. A.; Kosov, D. J. *Chem. Phys.* **2011**, *135*, 074701.
- (39) Breuer, H. P.; Petruccione, F. *The Theory of Open Quantum Systems*; Oxford University Press: Oxford, 2002.
- (40) Volkovich, R.; Hartle, R.; Thoss, M.; Peskin, U. *Phys. Chem. Chem. Phys.* **2011**, *13*, 14333.
- (41) Wunsch, B.; Braun, M.; König, J.; Pfannkuche, D. *Phys. Rev. B* **2005**, *72*, 205319.
- (42) Worth, G. A.; Cederbaum, L. S. *Annu. Rev. Phys. Chem.* **2004**, *55*, 127.

Charge Transport Induced Recoil and Dissociation in Double Quantum Dots

*Roni Pozner^{1,3,4}, Efrat Lifshitz^{1,3,4} and Uri Peskin^{*1, 2,4}*

*¹Schulich Faculty of Chemistry, ²the Lise Meitner Center for Computational Quantum
Chemistry, ³Solid State Institute and ⁴Russell Berrie Nanotechnology Institute,
Technion-Israel Institute of Technology, Haifa 32000, Israel*

* Corresponding author contact information: uri@tx.technion.ac.il

Supplementary Material

A. The dependence of the electronic parameters on the inter-dot distance

We start by associating the eigenstates of the electronic single particle dimer Hamiltonian with orthonormal super positions of local dot orbitals,

$$\begin{aligned}\varphi_1(\mathbf{r}) &= c_{A1}\chi_A(\mathbf{r}) + c_{B1}\chi_B(\mathbf{r}) \\ \varphi_2(\mathbf{r}) &= c_{A2}\chi_A(\mathbf{r}) + c_{B2}\chi_B(\mathbf{r})\end{aligned}\tag{A1}$$

$\chi_A(\mathbf{r})$ and $\chi_B(\mathbf{r})$ are non-orthogonal, normalized, three-dimensional Gaussians, $\chi_A(\mathbf{r}) = \left(\frac{1}{2\sigma^2\pi}\right)^{\frac{3}{4}} e^{\frac{-1}{4\sigma^2}(\mathbf{r}-\mathbf{R}_A)^2}$ and $\chi_B(\mathbf{r}) = \left(\frac{1}{2\sigma^2\pi}\right)^{\frac{3}{4}} e^{\frac{-1}{4\sigma^2}(\mathbf{r}-\mathbf{R}_B)^2}$, with an overlap integral, $S = \int d\mathbf{r}\chi_A(\mathbf{r})\chi_B(\mathbf{r}) = e^{\frac{-q^2}{8\sigma^2}}$, where $q = |\mathbf{R}_A - \mathbf{R}_B|$ is the inter-dot distance.

Using the normalization of $\varphi_1(\mathbf{r})$ and $\varphi_2(\mathbf{r})$, we rewrite,

$$\begin{aligned}c_{A1} &= \frac{a_1}{\sqrt{a_1^2 + b_1^2 + 2Sa_1b_1}} & ; & & c_{B1} &= \frac{b_1}{\sqrt{a_1^2 + b_1^2 + 2Sa_1b_1}} \\ c_{A2} &= \frac{a_2}{\sqrt{a_2^2 + b_2^2 + 2Sa_2b_2}} & ; & & c_{B2} &= \frac{b_2}{\sqrt{a_2^2 + b_2^2 + 2Sa_2b_2}}\end{aligned}\tag{A2}$$

and the orthogonality of $\varphi_1(\mathbf{r})$ and $\varphi_2(\mathbf{r})$ implies,

$$\frac{b_2}{a_2} = -\frac{1 + S\frac{b_1}{a_1}}{\frac{b_1}{a_1} + S}.\tag{A3}$$

The coefficients (a_1, a_2, b_1, b_2) and the respective single particle energies (defined as $\varepsilon_1, \varepsilon_2$) are uniquely defined by the generalized eigenvalue problem according to the standard linear variation principle,

$$[\mathbf{H} - \varepsilon \mathbf{S}] \mathbf{C} = \mathbf{0} . \quad (\text{A4})$$

\mathbf{H} is the single particle Hamiltonian matrix, \mathbf{S} is the overlap matrix as defined in Eq. 1 in the text, and \mathbf{C} is the coefficients matrix,

$$\mathbf{C} = \begin{bmatrix} c_{A1} & c_{A2} \\ c_{B1} & c_{B2} \end{bmatrix} \quad (\text{A5})$$

Notice that the matrices \mathbf{H} and \mathbf{S} depend explicitly on the inter-dot distance, q , and therefore the solutions to the generalized eigenvalue problem, i.e. the respective single particle energies $(\varepsilon_1, \varepsilon_2)$ and the expansion coefficients (a_1, a_2, b_1, b_2) also depend on the inter-dot distance.

Within the Fock space spanned by the two orthonormal single particle states, the electronic many-body dimer Hamiltonian reads,

$$\hat{H} = \varepsilon_1(q) a_1^\dagger a_1 + \varepsilon_2(q) a_2^\dagger a_2 + U(q) a_1^\dagger a_1 a_2^\dagger a_2 , \quad (\text{A6})$$

$U(q)$ is the two electron interaction term,

$$U(q) = U_{12}(q) - U_{ex}(q) , \quad (\text{A7})$$

where $U_{12}(q)$ and $U_{ex}(q)$ are respectively the coulomb and exchange integrals. Considering the explicit form of the local orbitals and the expansion coefficient, these integrals can be calculated as follows,

$$\begin{aligned}
U_{12}(q) &= \int d\mathbf{r}_1 \int d\mathbf{r}_2 \varphi_1^*(\mathbf{r}_1) \varphi_2^*(\mathbf{r}_2) \frac{Ke^2}{|\mathbf{r}_1 - \mathbf{r}_2|} \varphi_1(\mathbf{r}_1) \varphi_2(\mathbf{r}_2) \\
&= \frac{Ke^2}{(a_1^2 + b_1^2 + 2Sa_1b_1)(a_2^2 + b_2^2 + 2Sa_2b_2)} \cdot \\
&\quad \left\{ \sqrt{\frac{1}{\pi\sigma^2}} (a_1^2 a_2^2 + b_1^2 b_2^2 + 4a_1 b_1 a_2 b_2 e^{\frac{-q^2}{4\sigma^2}}) \right. \\
&\quad \left. + \frac{\text{erf}[q/2\sigma]}{q} (a_1^2 b_2^2 + b_1^2 a_2^2) \right. \\
&\quad \left. + e^{\frac{-q^2}{8\sigma^2}} \frac{\text{erf}[q/4\sigma]}{q/2} [(a_1^2 + b_1^2)2a_2 b_2 + 2a_1 b_1 (a_2^2 + b_2^2)] \right\}
\end{aligned} \tag{A8}$$

$$\begin{aligned}
U_{ex}(q) &= \int d\mathbf{r}_1 \int d\mathbf{r}_2 \varphi_1^*(\mathbf{r}_1) \varphi_2^*(\mathbf{r}_2) \frac{Ke^2}{|\mathbf{r}_1 - \mathbf{r}_2|} \varphi_2(\mathbf{r}_1) \varphi_1(\mathbf{r}_2) \\
&= \frac{Ke^2}{(a_1^2 + b_1^2 + 2Sa_1b_1)(a_2^2 + b_2^2 + 2Sa_2b_2)} \\
&\quad \cdot \left\{ \sqrt{\frac{1}{\pi\sigma^2}} (a_1^2 a_2^2 + b_1^2 b_2^2 + (a_1 b_2 + b_1 a_2)^2 e^{\frac{-q^2}{4\sigma^2}}) + \frac{\text{erf}[q/2\sigma]}{q} 2a_1 a_2 b_1 b_2 \right. \\
&\quad \left. + e^{\frac{-q^2}{8\sigma^2}} \frac{\text{erf}[q/4\sigma]}{q/2} [2a_1 a_2 (a_2 b_1 + b_2 a_1) + 2b_1 b_2 (a_2 b_1 + b_2 a_1)] \right\}
\end{aligned} \tag{A9}$$

The dependence of $U_{12}(q)$ and $U_{ex}(q)$ on the inter-dot distance is therefore uniquely determined by the specific single particle model invoked in the text.

Finally, we consider the dependence of the dimer-lead coupling on q . The coupling between the DQD and the STM tip(T) and the surface(S), corresponds to electron hopping between the localized orbitals ($\chi_{A/B}(\mathbf{r})$) and the lead states, $\hat{H}_{DQD-leads} = \sum_{n=1,2} \sum_{K=T,S} \sum_{k \in K} u_{k,K} \eta_{n,K} d_n b_{k,K}^\dagger + h.c.$, where d_n is the annihilation operator of an electron at the n^{th} dot orbital. Expanding the dot orbital in terms of the orthonormal DQD orbitals, $d_n = \sum_m D_{n,m}(q) a_m$, the coupling term becomes dependent on the inter-dot distance. Using Eq.(A1), it follows that

$$\begin{pmatrix} \chi_A(\mathbf{r}) \\ \chi_B(\mathbf{r}) \end{pmatrix} = \mathbf{C}^{-1}(q) \begin{pmatrix} \varphi_1(\mathbf{r}) \\ \varphi_2(\mathbf{r}) \end{pmatrix}, \quad (\text{A10})$$

and therefore we identify, $D_{m,n}(q) \equiv [\mathbf{C}(q)^{-1}]_{m,n}$.

B. Steady state currents through different double quantum dots

Fig. S1 depicts results for steady state currents through different DQD structures as functions of the applied bias voltage. The top and bottom rows correspond to strong and weak ligands-mediated inter-dot binding potential ($V(q_0 + 2\sigma) = 0.25, 0.0025$ eV, respectively), and left, middle and right plot in each row correspond to different symmetry of the DQD, i.e., $E_A - E_B = -0.05, 0, 0.05$ eV, respectively (illustrated by drawings). The other model parameters are $\sigma = 1$ nm, $q_0 = 5\sigma$, $(E_A + E_B)/2 = 0.25$ eV, $t_0 = -0.01$ eV, and $\gamma = 0.4$ nm⁻¹, $\beta_T = \beta_S = 5$ eV, and $\xi_S = \xi_T = 0.05$ eV, $K_B T = 0.001$ eV, $\mu_S = 0$.

In all cases steps in the current reflect the onset of four transport channels through the DQD at voltages $\mu_T - \mu_S = \varepsilon_1(q), \varepsilon_2(q), \varepsilon_1(q) + U(q), \varepsilon_2(q) + U(q)$. The respective step heights reflect the details of the DQD symmetry, and will be discussed elsewhere. The currents through a mechanically responsive DQD (solid) are compared to the currents for a rigid DQD (dashed). The differences between these curves are plotted in Fig. 3 in the text and reveal the manifestation of the effect of the mechanical recoil and dissociation on the measured currents. Small deviations in the threshold energies due to changes in the steady state inter-dot distance lead to the picks in Fig. 3. Notice that the sharp steps are due to the weak coupling between the DQD and the leads and the low temperature. We note that the reduced density matrix

approximation invoked in this work underestimates the step widths under these conditions[38].

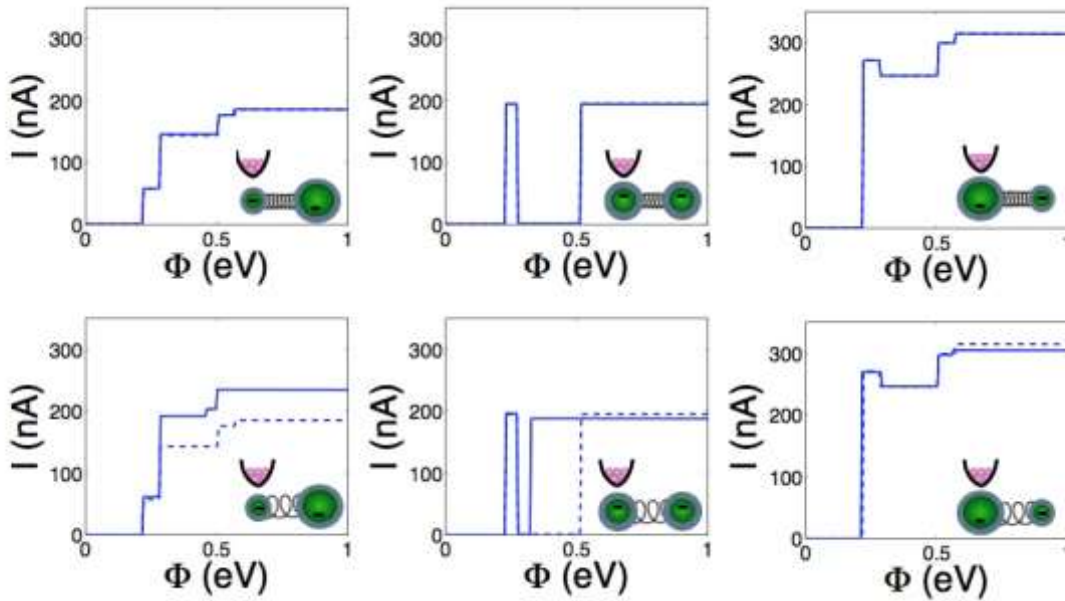


Figure S1: Steady state currents. Solid and dashed lines correspond to responsive and rigid DQD respectively. The tip-DQD-surface setup is illustrated by drawings for each case.

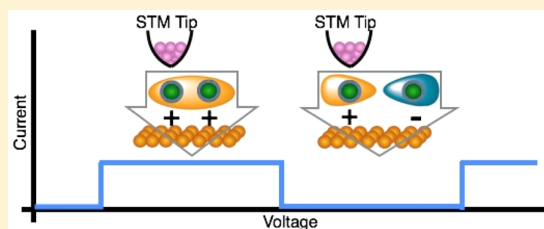
- 6.2 Negative Differential Resistance Probe for Interdot Interactions in a Double Quantum Dot Array, J. Phys. Chem. Lett, 6, 1521 (2015)**

Negative Differential Resistance Probe for Interdot Interactions in a Double Quantum Dot Array

Roni Pozner,^{†,‡,¶,||} Efrat Lifshitz,^{†,‡,¶,||} and Uri Peskin^{*,†,‡,¶,||}

[†]Schulich Faculty of Chemistry, [‡]Solid State Institute, [¶]Russell Berrie Nanotechnology Institute, and ^{||}Lise Meitner Center for Computational Quantum Chemistry, Technion-Israel Institute of Technology, Haifa 32000, Israel

ABSTRACT: Colloidal quantum dots are free-standing nanostructures with chemically tunable electronic properties. In this work, we consider a new STM tip–double quantum dot (DQD)–surface setup with a unique connectivity, in which the tip is coupled to a single dot and the coupling to the surface is shared by both dots. Our theoretical analysis reveals a unique negative differential resistance (NDR) effect attributed to destructive interference during charge transfer from the DQD to the surface. This NDR can be used as a sensitive probe for interdot interactions in DQD arrays.



The field of electronic transport through different quantum dots arrays¹ has been given much attention in recent years both experimentally and theoretically in search of different nonlinear effects. The focus has shifted between several key phenomena, such as coulomb blockade,^{2–5} spin blockade,^{6–9} Franck–Condon blockade,^{10,11} and negative differential resistance (NDR).^{12,13}

The observation of NDR, where the current decreases with increasing bias potential, has found various rationalizations and was studied in single quantum dots (SQDs), double quantum dots (DQDs), and triple quantum dots (TQDs) systems. A comprehensive review by Hettler et al.¹⁴ elucidates extensively the main mechanisms leading to NDR within SQD and DQD systems. In the extreme case, NDR can lead to vanishingly small currents. This is the case when dark states are involved, that is, when quantum mechanical superposition leads to decoupling between potentially conducting states and the leads. The effect of dark states, initially researched for the case of photon excitations,^{15–18} was studied at length in recent years for the analogue electronic cases of TQD^{19–24} and molecular junctions,^{25–27} where internal transport pathways interfere destructively within the device. In colloidal SQD or DQD, the internal structure does not support destructively interfering pathways. However, destructive interference of different pathways at the DQD–surface interface can give rise to a yet unexplored dark state, as discussed below.

Colloidal quantum dots (CQDs)^{28,29} with their chemically tunable electronic properties are of special interest for numerous electronic and optoelectronics applications. Ongoing research deals with the extent to which single dot properties^{30,31} and the interactions between dots in an array^{1,32} are of significance in relation to the observed transport properties and nonlinear effects in particular. Yet, the interdot interactions are difficult to assess, specifically when CQDs are concerned, because the interaction between CQDs is often controlled by their surface chemistry and by the organic ligands that link between the dots.

In this work, we study nonlinear effects in transport through arrays of CQDs. We address an extension of the well-established experimental studies of transport through SQDs^{33–39} to the case of coupled DQDs, as proposed in ref 40. The new setup of STM tip–DQD–surface⁴⁰ is shown to give rise to a new NDR effect, attributed to destructive interference during charge transport through the DQD. Our theoretical analysis below demonstrates how a unique dark state and the related NDR phenomenon lead to an appreciable nonlinear feature in the current through the DQD, which reveals the magnitude of interdot electronic interactions.

The model for the STM tip–DQD–surface configuration was recently introduced in ref 40 and is reviewed here for clarity. Each dot is represented by a single localized spin orbital, given the following assumptions: (i) Degeneracies of the neutral quantum dot orbitals are removed upon charging by an extra electron,^{41,42} (ii) multiple charging of each dot is excluded due to intradot Coulomb interaction, and (iii) spin is conserved during transport, and a single spin model is sufficient. The single dot orbitals are modeled here as 3D Gaussians, $\chi_A(r) = (2\sigma^2\pi)^{-3/4}e^{-(r-R_A)^2/(4\sigma^2)}$ and $\chi_B(r) = (2\sigma^2\pi)^{-3/4}e^{-(r-R_B)^2/(4\sigma^2)}$, where R_A and R_B are the dots center of mass coordinates and r is the electronic coordinate. The dots dimensions are captured in σ , the standard deviation of the respective probability distributions, $|\chi_{A/B}(r)|^2$. Setting $R_A \equiv (0,0,q/2)$ and $R_B \equiv (0,0,-q/2)$, the interdot distance, $|R_A - R_B| = q$, defines the overlap between these two localized orbitals, $s(q) = \int dr \chi_A(r)\chi_B(r) = e^{-q^2/(8\sigma^2)}$, and the effective single-electron Hamiltonian matrix in the basis of $\chi_{A/B}(r)$ is assumed to be of a generic form

$$H(q) = \begin{pmatrix} E_A & t_0 e^{-\gamma(q-q_0)} \\ t_0 e^{-\gamma(q-q_0)} & E_B \end{pmatrix} \quad \mathbb{S}(q) = \begin{pmatrix} 1 & s(q) \\ s(q) & 1 \end{pmatrix} \quad (1)$$

Received: March 1, 2015

Accepted: April 2, 2015



Thereby, E_A and E_B are considered as the LUMO energies of the two separated dots at $q \rightarrow \infty$. (The choice $E_A \neq E_B$ accounts for differences between the dots owing to the composition, local external fields, etc.) The electronic coupling set by nanoparticle boundaries and the surrounding ligands^{43,44} is assigned a typical exponential decay form, where q_0 is the interdot distance, for which the interdot hopping parameter equals t_0 , and γ defines the decay of the hopping interaction as the interdot distance increases.

The single-particle energies ϵ_1 and ϵ_2 can be calculated using the generalized linear variation principle,⁴⁵ $[H - \epsilon S]C = 0$, where C is the coefficients matrix

$$C = \begin{pmatrix} c_{A1} & c_{A2} \\ c_{B1} & c_{B2} \end{pmatrix} \quad (2)$$

where the respective orthonormal DQD orbitals read

$$\begin{aligned} \phi_1(r) &= c_{A1}\chi_A(r) + c_{B1}\chi_B(r) \\ \phi_2(r) &= c_{A2}\chi_A(r) + c_{B2}\chi_B(r) \end{aligned} \quad (3)$$

Denoting the electron creation and annihilation operators for the n th orbital as \hat{a}_n^\dagger and \hat{a}_n , respectively, the projection of the DQD Hamiltonian on the Fock space defined by the two orbitals reads

$$\hat{H}_{\text{DQD}} = \epsilon_1 \hat{a}_1^\dagger \hat{a}_1 + \epsilon_2 \hat{a}_2^\dagger \hat{a}_2 + U \hat{a}_1^\dagger \hat{a}_1 \hat{a}_2^\dagger \hat{a}_2 \quad (4)$$

U is the two-particle interaction term, $U = \iint dr_1 dr_2 \phi_1(r_1)\phi_2(r_2) \times [1/|r_1 - r_2|][\phi_1(r_1)\phi_2(r_2) - \phi_2(r_1)\phi_1(r_2)]$, which depends on the interdot distance via the orbital coefficients (eqs 1–3).

The DQD is coupled to the STM tip (T) and to the surface (S), both regarded as reservoirs of noninteracting electrons⁴⁶

$$\hat{H}_{\text{leads}} = \sum_{K=T,S} \sum_{k \in K} \epsilon_{k,K} \hat{b}_{k,K}^\dagger \hat{b}_{k,K} \quad (5)$$

where $\hat{b}_{k,K}^\dagger$ is the electron creation operator in the k th state of the K th reservoir.

The coupling between the reservoirs and the DQD corresponds to electron hopping between the localized orbitals ($\chi_{A/B}(r)$) and the lead states

$$\hat{H}_{\text{DQD-leads}} = \sum_{n=1,2} \sum_{K=T,S} \sum_{k \in K} u_{k,K} \eta_{n,K} \hat{a}_n^\dagger \hat{b}_{k,K}^\dagger + \text{h.c.} \quad (6)$$

\hat{a}_n is the electron annihilation operator at the n th dot sites, and the matrix equation that correlates between the n th dot and m th orbital takes the form

$$\begin{pmatrix} \hat{a}_1 \\ \hat{a}_2 \end{pmatrix} = \begin{pmatrix} D_{11} & D_{12} \\ D_{21} & D_{22} \end{pmatrix} \begin{pmatrix} \hat{a}_1 \\ \hat{a}_2 \end{pmatrix} \quad (7)$$

where $D_{m,n} \equiv [C^{-1}]_{m,n}$ (see eq 2). The DQD–leads connectivity is defined by $\{\eta_{n,K}\}$, which equals one or zero if the K th lead is coupled or uncoupled to the n th dot, respectively

$$\begin{pmatrix} \hat{f}_T \\ \hat{f}_S \end{pmatrix} = \begin{pmatrix} \eta_{1,T} & \eta_{2,T} \\ \eta_{1,S} & \eta_{2,S} \end{pmatrix} \begin{pmatrix} \hat{a}_1 \\ \hat{a}_2 \end{pmatrix} \quad (8)$$

where \hat{f}_T and \hat{f}_S are the annihilations operators of an electron in a superposition of dot states for the tip and surface contacts, respectively. The leads coupling parameters are associated with a semielliptic band model with a bandwidth, $|4\beta_K|$, and a chemical potential, μ_K , where the spectral density reads⁴⁷ $J_K(\epsilon) = 2\pi \sum_{k \in K} |u_{k,K}|^2 \delta(\epsilon - \epsilon_{k,K}) = (\xi_K^2/\beta_K^2)(|4\beta_K|^2 - (\epsilon - \mu_K)^2)^{1/2}$. μ_T and μ_S are

the chemical potentials for the STM tip and the surface, respectively, where μ_S is set to zero in the calculations presented below. The full Hamiltonian finally reads

$$\hat{H} = \hat{H}_{\text{DQD}} + \hat{H}_{\text{leads}} + \hat{H}_{\text{leads-DQD}} \quad (9)$$

For typical electronic tunnelling barriers between the DQD and the STM tip and between the DQD and the surface, the dynamics of the DQD density can be approximated in the weak electronic coupling limit, using the density matrix approach.⁴⁷ The reduced DQD density is represented in the basis of the \hat{H}_{DQD} eigenstates. \hat{H}_{DQD} commutes with the electronic number operator, and each eigenstate is associated with occupation numbers of the DQD orbitals, $m, n \in 0, 1$, where, $\hat{H}_{\text{DQD}}|mn\rangle = E_{mn}|mn\rangle$. The leads are assumed to maintain a quasi-equilibrium density, while the DQD system evolves according to the reduced Liouville equation to second order in the coupling to the leads. Coherences between the DQD eigenstates should be insignificant at steady state due to the relatively large separation between the system eigenvalues, and due to the electronic interactions,⁴⁸ which are a source of decoherence when U exceeds the level broadening caused by the DQD–leads coupling and the temperature. The effect of coupling to the leads therefore amounts to changes in the DQD eigenstate populations induced by electron hopping events⁴⁷

$$\frac{d}{dt} P_{mn}(t) = \sum_{m'n'} [\kappa^{(S)} + \kappa^{(T)}]_{mn,m'n'} P_{m'n'}(t) \quad (10)$$

where $P_{mn}(t)$ is the population of the respective eigenstate of the DQD Hamiltonian and $[\kappa^{(K)}]_{mn,m'n'}$ are rates of transitions induced by the K th lead⁴⁹

$$\begin{aligned} [\kappa^{(K)}]_{mn,m'n'} &= (1 - \delta_{mn,m'n'}) \frac{(\Gamma_{mn,m'n'}^{(K);h} + \Gamma_{mn,m'n'}^{(K);e})}{\hbar} \\ &\quad - \delta_{mn,m'n'} \sum_{m''n'' \neq mn} \frac{(\Gamma_{m''n'',m'n'}^{(K);h} + \Gamma_{m''n'',m'n'}^{(K);e})}{\hbar} \end{aligned} \quad (11)$$

The charge hopping energies are given as

$$\Gamma_{mn,m'n'}^{(K);e/h} \equiv V_{mn,m'n'}^2 f_e^{(K)}(E_{m'n'} - E_{mn}) J_{(K)}(E_{m'n'} - E_{mn}) \quad (12)$$

where $V_{mn,m'n'}^2 = |[\sum_{j=1,2} \sum_l D_{lj} \eta_{l,K} \alpha_j]_{mn,m'n'}|^2$ and $f_e^{(K)}(\epsilon) = 1/(1 + e^{(\epsilon - \mu_K)/(k_B T)})$ and $f_h^{(K)}(\epsilon) = 1 - f_e^{(K)}(\epsilon)$ are the Fermi distribution functions.

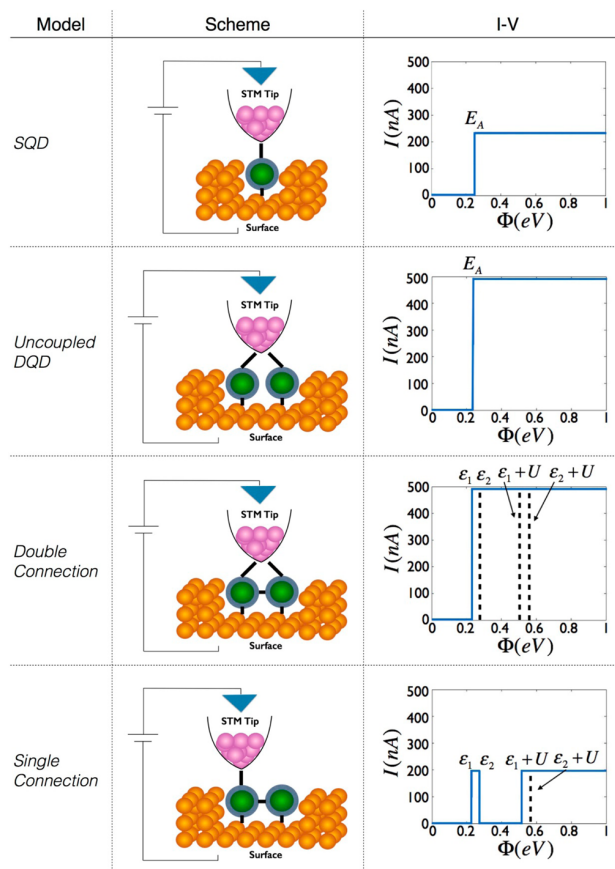
The current from the tip to the surface is

$$I_{T \rightarrow S} = 2e \lim_{t \rightarrow \infty} \sum_{mn,m'n'} [\kappa_{mn,m'n'}^{(T)}] P_{m'n'}(t) N_{mn} \quad (13)$$

where N_{mn} is the electron number in the (nm) th DQD eigenstate.

We begin our discussion by comparing the transport through a SQD to transport through a symmetric DQD, $E_A = E_B$, coupled to an STM tip and a surface (see Table 1) in different connection schemes. Following eq 8, the “double connection” scheme is assigned by the following connectivity matrix, $\eta_{1,T} = \eta_{2,T} = \eta_{1,S} = \eta_{2,S} = 1$, while the “single connection” scheme is assigned by $\eta_{1,T} = \eta_{1,S} = \eta_{2,S} = 1$ and $\eta_{2,T} = 0$. In the absence of interactions (both single- and two-electron interactions) between the dots, the I – V curve reflects the behavior of a single transport channel with a single threshold energy at E_A . Comparing the case of a single dot (Table 1, first row) to the case of two uncoupled dots (Table 1, second row), there is no change in the threshold voltage, E_A , but the current doubles due to the presence of a

Table 1. STM Tip–DQD–Surface Setup Schemes (top row) and Their Corresponding Steady-State Currents versus the Tip–Surface Potential Bias ($\Phi = \mu_T$; $\mu_S = 0$) (bottom row)^a



^aThe first and second rows illustrate a single on-site energy E_A threshold for a single dot and double uncoupled dots. The current step in the first row is half of the current step in the second row. The third and fourth rows illustrate the behaviour of the coupled double dot systems. The double connection scheme (third row) reveals only a single threshold at ϵ_1 , which is shifted with respect to E_A due to the interdot electronic interaction. The single connection scheme (fourth row) exhibits three thresholds and a pronounced NDR effect that depends on the interdot coupling. The Hamiltonian parameters were set to $E_A = E_B = 0.25$ eV, $t_0 = -0.01$ eV, $\gamma = 0.4$ nm⁻¹, $\sigma = 1$ nm, $q_0 = 5\sigma$, $\beta_T = \beta_S = -5$ eV, $\xi_T = \xi_S = -0.05$ eV, $K_B T = 0.001$ eV, $\mu_S = 0$, which corresponds to $U(q_0) = 0.286$ eV, $\epsilon_2(q_0) = 0.272$ eV, $\epsilon_1(q_0) = 0.230$ eV, and energy splitting, $\Delta\epsilon = 0.042$ eV. (Thresholds that are not reflected in the current are marked by dotted vertical lines.)

second dot. In the presence of interdot interactions, in the double connection scheme (Table 1, third row; the tip is coupled to both dots), there is a shift of the threshold step that is indicative of the interdot coupling strength t , whereas in the single connection scheme (Table 1, fourth row; the tip is coupled only to the left dot), there is a dramatic change where the current drops at the second threshold, ϵ_2 , and exhibits a pronounced NDR effect.

The coupled DQD systems (Table 1, third and fourth rows) have four distinctive eigenstates: at zero energy, (00) indicates an empty state; at $\epsilon_1 = (E_A - t)/(1 - s)$, (10) is associated with a single electron populating a symmetric DQD orbital without a nodal plane (bonding state $c_{A1} = c_{B1}$); at $\epsilon_2 = (E_A + t)/(1 + s)$, (01) is associated with an electron populating an antisymmetric DQD orbital having a nodal plane between the dot centers

(antibonding state $c_{A2} = -c_{B2}$); and finally, at $\epsilon_1 + \epsilon_2 + U$, (11) is associated with two-electron population and an additional two-body (electrostatic) repulsion. Steps in the current reflect the onset of charge-transport channels⁵⁰ associated with transitions between these states at the bias potentials, $\Phi = \mu_T = \epsilon_1, \epsilon_2, \epsilon_1 + U, \epsilon_2 + U$, setting μ_S to zero.

The single and double connection cases will be further elaborated here for different bias potentials. Table 2 depicts the energetically allowed transition rates (top row) and the underlying coupling matrix elements (bottom rows) in the two cases, where blue and red correspond to the single connection, while green and purple correspond to the double connection. Processes that are blocked due to the destructive interference at the coupling to the contacts are indicated by dashed arrows.

In the single connection scheme (Table 1, fourth row), the first step observed in the current, at $\epsilon_2 > \Phi > \epsilon_1$, ensues due to the coupling between the empty DQD state and the bonding state (10) (denoted V_0^2 in Table 2, first column, third row). As the bias potential increases to the next step at $\epsilon_1 + U > \Phi > \epsilon_2$ (Table 2, second column), the antibonding state ϵ_2 also gains a finite probability for occupation. Due to the unique connectivity in this case, charging and discharging rates of the state ϵ_2 are dramatically different. While charging from the tip has a positive probability, discharging to the surface is blocked by destructive interference due to the opposite signs of the probability amplitudes on the two dots. Therefore, the electron in the ϵ_2 state is trapped in a “dark state” with respect to the coupling to the surface, and this channel is not contributing to the current. In order for the ϵ_1 state to be occupied in this case, a finite charging energy of $\epsilon_1 + U$ is needed, but the tip chemical potential is too low, and hence, the ϵ_1 state remains empty. No channel is contributing to the current, and for that reason, the current drops to zero, giving rise to a pronounced NDR. As the bias potential increases to a higher level, $\epsilon_2 + U > \Phi > \epsilon_1 + U$ (Table 2, third column), a new channel for transport is opened, $\epsilon_1 + U$, and the current builds up again. Interestingly, although the mechanism leading to the steady-state current changes in this bias regime (see Table 2, third and fourth columns), the currents before and after the NDR window are equal.

Notice that the NDR feature is absent in the double connection scheme (Table 1, third row; Table 2, green and purple arrows). Indeed, only a single threshold is observed in the current (at $\Phi = \mu_T = \epsilon_1$), which ensues due to the coupling between the empty DQD state and the bonding state (10) . The antibonding state ϵ_2 in this scheme is blocked for charging as well as for discharging due to destructive interference at both the surface and the tip. Therefore, the ϵ_2 state stays empty permanently, and because of that, only the ϵ_1 state contributes to the current for any bias.

The above analysis suggests that the current in the single connection scheme can provide a sensitive probe for the interdot interaction. Indeed, at low temperatures, ($K_B T \ll |\epsilon_2 - \epsilon_1|$), the NDR leads to a distinctive plateau between the two thresholds, ϵ_2 and ϵ_1 , in the current–voltage curve (see Table 1). Subtracting the threshold energies (both measurable in this case), $\Delta\epsilon = \epsilon_2 - \epsilon_1 = (2(sE_A - t)/(1 - s^2))$, the value of the interaction can be revealed, provided that the overlap between the two localized orbitals, s , is sufficiently small.

Notice that NDR in transport through tunneling barriers can originate from different physical phenomena. For example, NDR through a double-barrier resonance in lateral quantum wells was attributed to classical charging of the intermediate well where the resonant tunneling level reaches the bottom of the emitter

Table 2. Transition Rates (top row) and Coupling Matrix Elements (two bottom rows) for Different Bias Potentials for the DQD in the Two Connection Schemes^a

Bias	$\varepsilon_2 > \Phi > \varepsilon_1$	$\varepsilon_1 + U > \Phi > \varepsilon_2$	$\varepsilon_2 + U > \Phi > \varepsilon_1 + U$	$\Phi > \varepsilon_2 + U$
Transition rates				
Coupling Matrix Elements, Double Connection Scheme				
Coupling Matrix Elements, Single Connection Scheme				

^aBlue (red) corresponds to transitions into (out of) the DQD in the single connection, and green (purple) corresponds to transitions into (out of) the DQD in the double connection. Coupling strengths are expressed in units of $V_0^2 \equiv V_{00,10}^2$, which denotes the $00 \rightarrow 10$ transition (the value $4V_0^2$ is a correct approximation for $s \ll 1$). We mark interference-blocked transitions using dashed arrows. The first column shows the transport through the first bonding orbital, ε_1 . The second column accounts for a higher bias where the second antibonding orbital, ε_2 , becomes energetically accessible. Notice that this orbital is blocked due to an interference effect in the coupling to the surface (and also to the tip in the double connection), leading to the NDR. The third and fourth columns describe additional transport channels that rebuild the current at higher bias (see ref S1 for details).

conductance band⁵² or to electron trapping by phonon emission.^{53,54} These mechanisms can be supported by experimental studies involving AC frequency current dependency or temperature changes, respectively. Indeed, from the experimental point of view, the unique impact of the interdot coupling on the observed NDR should be verified prior to deduction of the coupling strength parameter from the measured signal. The distance between the DQDs can be used as an experimental control parameter for this purpose, as discussed below.

As noted in the model (eq 1), the electronic coupling terms depend on the interdot distance q (see also ref 40). This dependence leads to a shift in the position of the steps in the $I-V$ curve and, in particular, to increasing or decreasing width of the NDR plateau upon decreasing and increasing q , respectively, as can be seen in Figure 1. In colloidal DQD, the interdot distance is controlled by the capping ligands. Observed sensitivity of the NDR signal to the interdot distance would indicate that this signal indeed originates from the dark state mechanism discussed above because no other known NDR mechanism predicts such distance dependence. Moreover, the NDR signal can be used in this case as a probe for the arrangement of the ligands around and between the dots. In turn, different ligands can be used in order to manipulate the NDR signal for nanoelectronic applications.

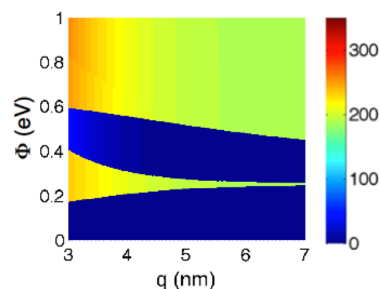


Figure 1. Steady-state currents versus the tip-surface potential (Φ) bias and interdot distance (q) for a symmetric DQD model. The model parameters are given in Table 1.

So far, we considered the case of a symmetric DQD. However, nonsymmetric DQDs can be obtained by using CQDs with different sizes and compositions.⁴⁰ Within the present model, the difference between the dots is reflected in different LUMO energies, that is, $E_A \neq E_B$. Figure 2A depicts the current as a function of bias potential and the DQD asymmetry parameter ($E_A - E_B$). The characteristics of the current for three representative cross sections at $E_A < E_B$, $E_A = E_B$, and $E_A > E_B$ are shown in Figure 2B–D, respectively, for the interdot distance fixed at a reference value, $q = q_0$ (see Table 1 for the model

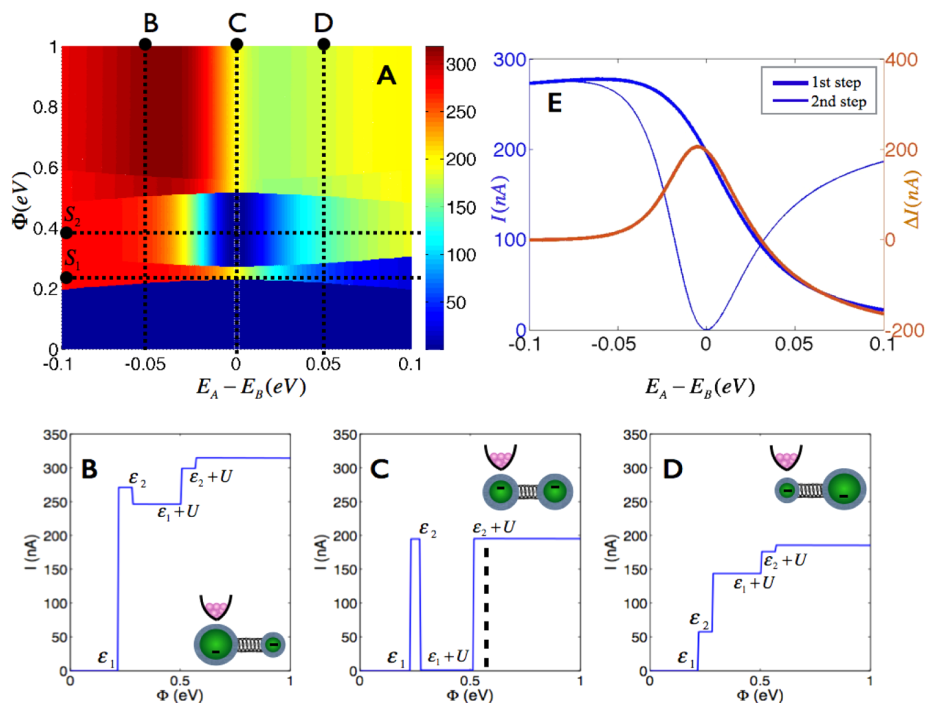


Figure 2. Steady-state currents. The top left plot is a color map of I - V curves for different values of the energy mismatch between the two dots. The bottom plots, from left to right, are selected I - V curves for $E_A - E_B = -0.05, 0, 0.05$, respectively. The top right plot includes in blue a cross section of the current through the DQD system at two distinctive bias potentials (0.25 and 0.4 eV), chosen specifically to exhibit the turning point between NDR and non-NDR as a function of the asymmetry parameter $E_A - E_B$. The brown curve shows the difference between the two steps and highlights the fact that the maximal gap between the curves is obtained in the vicinity of the symmetric case. The interdot distance is fixed at a reference value, $q = q_0$. The model parameters are given in Table 1.

parameters). Unlike in the symmetric case (Figure 2C) discussed in detail above, the NDR is less pronounced in nonsymmetric cases. Only a small drop in the current is observed when the tip is placed above the larger of the two dots (Figure 2B), and the NDR is completely missing when the tip is placed above the smaller dot (Figure 2D).

The dependence of the NDR effect on the asymmetry parameter is illustrated in Figure 2E, which brings to light two cross-sectional plots of the current in Figure 2A for two selected bias potentials. The first cross section represents the first step in the current, where the transport occurs only through the bonding DQD orbital. The second cross section represents the second step, where either the bonding or the nonbonding DQD orbitals are energetically accessible. The NDR is associated with a current drop from the first to the second step. As can be seen in Figure 2E, the maximal drop is obtained near the symmetric configuration, $E_A \approx E_B$. This is due to the perfectly destructive interference in the coupling between the DQD and the surface in the symmetric configuration. However, the NDR is maintained also over a range of nonsymmetric structures, where $|E_A - E_B| \lesssim 30$ meV.

On the basis of the relations in eqs 7 and 8, a unified formulation of the symmetric and asymmetric single connection scheme can be obtained by expressing the coupling operators of the DQD to the surface and to the tip in terms of the DQD operators, \hat{a}_1 and \hat{a}_2

$$\begin{pmatrix} \hat{J}_T \\ \hat{f}_S \end{pmatrix} = \begin{pmatrix} 1 & 0 \\ 1 & 1 \end{pmatrix} \begin{pmatrix} D_{11} & D_{12} \\ D_{21} & D_{22} \end{pmatrix} \begin{pmatrix} \hat{a}_1 \\ \hat{a}_2 \end{pmatrix} \equiv \begin{pmatrix} F_{T,1} & F_{T,2} \\ F_{S,1} & F_{S,2} \end{pmatrix} \begin{pmatrix} \hat{a}_1 \\ \hat{a}_2 \end{pmatrix} \quad (14)$$

where F is the matrix of coupling between the DQD orbitals and the leads (tip and surface). In the symmetric case, the relation between the DQD orbitals and the localized dots orbitals (eq 7) takes the form

$$\begin{pmatrix} D_{11} & D_{12} \\ D_{21} & D_{22} \end{pmatrix} = \frac{1}{\sqrt{2}} \begin{pmatrix} \sqrt{1+s} & \sqrt{1-s} \\ \sqrt{1+s} & -\sqrt{1-s} \end{pmatrix} \quad (15)$$

Assigning the values of the symmetric case to the coupling terms gives $F_{T,1} = F_{T,2}$, while $F_{S,1} \neq F_{S,2} = 0$. The second orbital (ϵ_2) is therefore connected to the tip but disconnected from the surface (a dark state). Charging this orbital from the tip leads to the NDR, as discussed above. For a strongly asymmetric DQD, when the tip is on top of the larger QD (Figure 2B), similar considerations show that $|F_{T,2}| \ll |F_{S,2}|$. Because charging of the ϵ_2 orbital from the tip becomes much slower than discharging to the surface in this case, the steady-state population of the ϵ_2 orbital becomes small, and NDR becomes insignificant. When the tip is placed above the smaller QD (Figure 2D), one has $|F_{S,2}| \approx |F_{S,1}| \gg |F_{T,1}|$. This implies that the current through the ϵ_1 orbital is much smaller than the current through the ϵ_2 orbital, excluding the possibility for NDR in this case.

The above discussion suggests that strongly asymmetric DQDs will not show NDR. However, the NDR can still be pronounced for weakly asymmetric DQD structures. It is instructive in this context to look into the sensitivity of the NDR to the distance between the QDs. Figure 3 presents the orbital-leads coupling matrix elements (F (eq 14)) for different asymmetries and different interdot distances. In the lower right plot, $F_{S,2}$ is shown to equal zero for $E_A = E_B$ regardless of the interdot distance q , in accordance with the analysis above. Notice that for smaller interdot distances, the

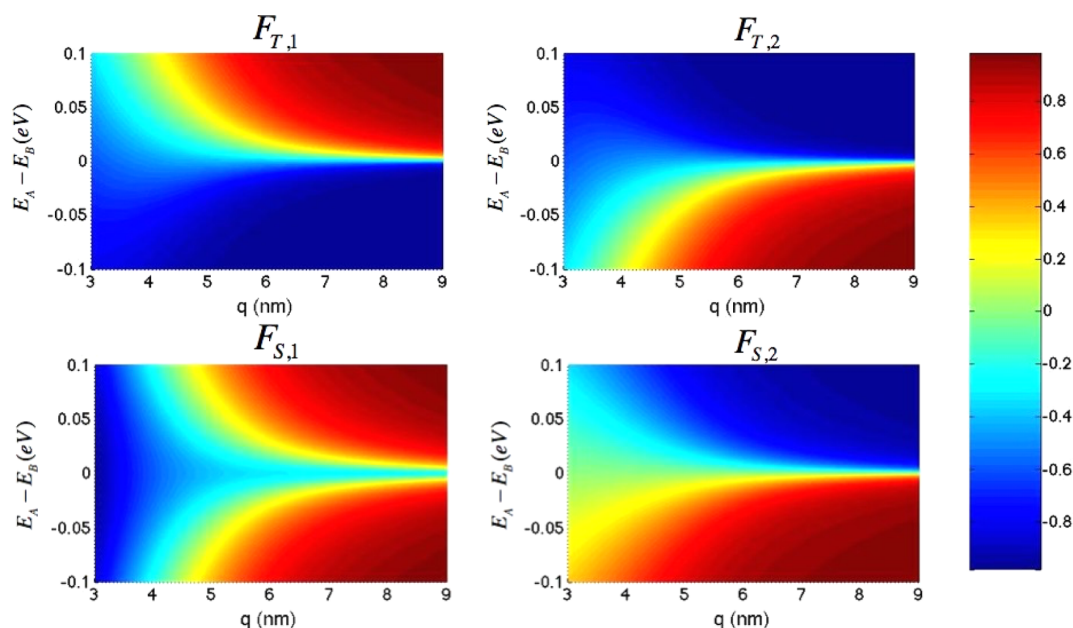


Figure 3. Orbital coupling to the tip and surface, (as defined in eq 14), as functions of the asymmetry parameter ($E_A - E_B$) and the interdot distance q . The green color accounts for vanishing coefficients.

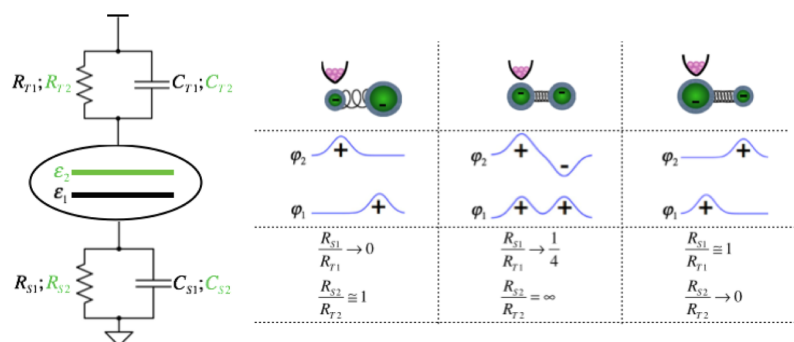


Figure 4. A double-barrier tunnelling junction model of the tip–DQD–surface system. Each one of the DQD orbitals ($n = 1, 2$) has different effective resistance and capacitance at the contacts to the tip (R_{Tn}, C_{Tn}) and to the surface (R_{Sn}, C_{Sn}). The effective contact resistance increases as the probability density of the orbital decreases at that contact. When the tip is coupled to the smaller (larger) dot (left/right column), the probability density of the antibonding orbital ($n = 2$) at the contact to the tip is small (large), meaning $R_{S2}/R_{T2} \cong 1$ ($R_{S2}/R_{T2} \ll 1$), respectively. This results in high/low population of this orbital.⁴⁰ When the dots are equal (middle column), the coupling to the surface goes to zero due to the interference effect, meaning $R_{S2}/R_{T2} = \infty$.

range of asymmetric structures for which $F_{S,2} \approx 0$ (the green-colored area) becomes larger, implying that a dark-like state and the resulting NDR are expected to be observed also for asymmetric DQD structures at short distances.

We end our discussion with a heuristic RC scheme⁴⁰ of transport through the DQD. In contrast to orthodox RC schemes,^{55,56} where the two dots are modeled as separate entities connected by incoherent transition rates, the coherence relation between the dots within a DQD hinders the use of a classical kinetic description. Because of that, in our model, each of the single-electron orbitals, and not each dot, affixes with different RC parameters, as illustrated in the double-barrier tunnelling junction model of the tip–DQD–surface system in Figure 4, left. In this scheme, each one of the DQD orbitals ($n = 1, 2$) has different effective resistance and capacitance at the contacts to the tip (R_{Tn}, C_{Tn}) and to the surface (R_{Sn}, C_{Sn}). The probability density of an orbital at each contact determines the effective contact resistance.

Exploring once more the different DQD asymmetries, the ratios between the contact resistance of the different DQD orbitals to the tip and the surface are summarized in the third row of Figure 4, right. We wish to emphasize that the different asymmetries imply also different DQD–tip/DQD–surface coupling ratios for the different transport channels, as illustrated in the second row of Figure 4, right. For strongly asymmetric DQD, only one of the two conducting DQD states is strongly coupled to the tip, while both states are coupled to the surface. For example, when the tip is above the larger QD (rightmost column in Figure 4), the bonding state is coupled to both the tip and surface, and the antibonding state is coupled mostly to the surface but weakly to the tip. Therefore, the contact resistance at the tip is larger than the contact resistance at the surface for the antibonding orbital ($n = 2$), $R_{S2}/R_{T2} \ll 1$, while the resistances are approximately equal for the bonding orbital, $R_{S2}/R_{T2} \cong 1$. Similar considerations apply for the ratios for the opposite

antisymmetric case. When the two dots are equal, the resistance of the antibonding to the surface goes to infinity, $R_{S2}/R_{T2} = \infty$ because of the destructive interference effect, and the resistance of the bonding orbital is smaller by a factor of 4 to the surface than to the tip due to constructive interference at the coupling to the surface.

In conclusion, a unique NDR is predicted within a unique STM setup for measuring transport through colloidal DQDs. The special setup enables coherent (phase-preserving) coupling between the DQD states and the substrate and local coupling between the STM tip and one of the QDs. In cases of symmetric (or nearly symmetric) DQDs, the current through this setup reveals interference between different pathways of charge transport from the tip to the surface, attributed to delocalized orbitals of the neighboring CQDs. In particular, destructive interference through an antibonding-like DQD orbital results in charging of a dark state that blocks the current through the DQD via Coulomb repulsion, resulting in an appreciable NDR and a corresponding distinctive signal in the current–voltage curve. Our theoretical analysis shows that an accurate measurement of the interdot interaction can be based on the measurement of this NDR signal, providing valuable information on the intricate electronic interaction between two neighboring dots in a DQD array. Experimental realization of the NDR phenomena in this particular setup is currently being pursued, which may provide a new route for direct measurements of the interdot electronic interaction. Finally, the NDR discussed here, in combination with the DQD dissociation effect presented elsewhere⁴⁰ for the same setup, could be used for the design of novel electromechanical devices such as electromechanical memory devices or devices for measuring mechanical coupling between DQDs surrounded with capping ligands. This will be discussed elsewhere.

AUTHOR INFORMATION

Corresponding Author

*E-mail: uri@tx.technion.ac.il.

Notes

The authors declare no competing financial interest.

ACKNOWLEDGMENTS

This research was supported by the German Israeli Foundation Grant 1154-119.5/2011 (U.P.). The research work at E.L.'s laboratory was supported by the Volkswagen Stiftung Project 88116, the Niedersachsen-Deutsche Technion Gesellschaft E.V Project ZN2916, and the Focal Area Technology (FTA) - Council For Higher Education Project 872967. R.P. acknowledges support by the Nancy and Stephan Grand Technion Energy Program (GTEP) center.

REFERENCES

- (1) Guyot-Sionnest, P. Electrical Transport in Colloidal Quantum Dot Films. *J. Phys. Chem. Lett.* **2012**, *3*, 1169–1175.
- (2) Livermore, C.; Crouch, C. H.; Westervelt, R. M.; Campman, K. L.; Gossard, A. C. The Coulomb Blockade in Coupled Quantum Dots. *Science* **1996**, *274*, 1332–1335.
- (3) Matveev, K. A.; Glazman, L. I.; Baranger, H. U. Coulomb Blockade of Tunneling through a Double Quantum Dot. *Phys. Rev. B* **1996**, *54*, 5637–5646.
- (4) Banin, U.; Millo, O. Tunneling and Optical Spectroscopy of Semiconductor Nanocrystals. *Annu. Rev. Phys. Chem.* **2003**, *54*, 465–492.
- (5) Millo, O.; Katz, D.; Cao, Y.; Banin, U. Scanning Tunneling Spectroscopy of InAs Nanocrystal Quantum Dots. *Phys. Rev. B* **2000**, *61*, 16773–16777.
- (6) Weber, B.; Matthias, T. H.; Mahapatra, S.; Watson, T. F.; Ryu, H.; Rahman, R.; H.C. L.; Klimeck, G.; Simmons, M. Y. Spin Blockade and Exchange in Coulomb-Confined Silicon Double Quantum Dots. *Nature Nanotechnol.* **2014**, *9*, 430–435.
- (7) Iñarrea, J.; Platero, G.; MacDonald, A. H. Electronic Transport through a Double Quantum Dot in the Spin-Blockade Regime: Theoretical Models. *Phys. Rev. B* **2007**, *76*, 085329.
- (8) Amaha, S.; Izumida, W.; Hatano, T.; Tarucha, S.; Kono, K.; Ono, K. Spin Blockade in a Double Quantum Dot Containing Three Electrons. *Phys. Rev. B* **2014**, *89*, 085302.
- (9) Delgado, F.; Shim, Y.-P.; Korkusinski, M.; Gaudreau, L.; Studenikin, S. A.; Sachrajda, A. S.; Hawrylak, P. Spin-Selective Aharonov–Bohm Oscillations in a Lateral Triple Quantum Dot. *Phys. Rev. Lett.* **2008**, *101*, 226810.
- (10) Sapmaz, S.; Jarillo-Herrero, P.; Blanter, Y. M.; Dekker, C.; van der Zant, H. S. J. Tunneling in Suspended Carbon Nanotubes Assisted by Longitudinal Phonons. *Phys. Rev. Lett.* **2006**, *96*, 026801.
- (11) Leturcq, R.; Stampfer, C.; Inderbitzin, K.; Durrer, L.; Hierold, C.; Mariani, E.; Schultz, M. G.; von Oppen, F.; Ensslin, K. Franck–Condon Blockade in Suspended Carbon Nanotube Quantum Dots. *Nat. Phys.* **2009**, *5*, 327–331.
- (12) Esaki, L. New Phenomenon in Narrow Germanium $p-n$ Junctions. *Phys. Rev.* **1958**, *109*, 603–604.
- (13) Esaki, L.; Tsu, R. Superlattice and Negative Differential Conductivity in Semiconductors. *IBM J. Res. Dev.* **1970**, *14*, 61–65.
- (14) Pedersen, J. N.; Lassen, B.; Wacker, A.; Hettler, M. H. Coherent Transport through an Interacting Double Quantum Dot: Beyond Sequential Tunneling. *Phys. Rev. B* **2007**, *75*, 235314.
- (15) Borges, H. S.; Sanz, L.; Villas-Bôas, J. M.; Alcalde, A. M. Robust States in Semiconductor Quantum Dot Molecules. *Phys. Rev. B* **2010**, *81*, 075322.
- (16) Ibáñez Berganza, M.; Petri, A.; Coletti, P. Dynamic Metastability in the Two-Dimensional Potts Ferromagnet. *Phys. Rev. E* **2014**, *89*, 052115.
- (17) Stinaff, E. A.; Scheibner, M.; Bracker, A. S.; Ponomarev, I. V.; Korenev, V. L.; Ware, M. E.; Doty, M. F.; Reinecke, T. L.; Gammon, D. Optical Signatures of Coupled Quantum Dots. *Science* **2006**, *311*, 636–639.
- (18) Kim, D.; Carter, S. G.; Greulich, A.; Bracker, A. S.; Gammon, D. Ultrafast Optical Control of Entanglement between Two Quantum-Dot Spins. *Nat. Phys.* **2011**, *7*, 229.
- (19) Michaelis, B.; Emary, C.; Beenakker, C. W. J. All-Electronic Coherent Population Trapping in Quantum Dots. *Europhys. Lett.* **2006**, *73*, 677.
- (20) Schijven, P.; Müllen, O. Avoiding Dark States in Open Quantum Systems by Tailored Initializations. *Phys. Rev. E* **2012**, *85*, 062102.
- (21) Brandes, T.; Renzoni, F. Current Switch by Coherent Trapping of Electrons in Quantum Dots. *Phys. Rev. Lett.* **2000**, *85*, 4148–4151.
- (22) Emary, C. Dark States in the Magnetotransport through Triple Quantum Dots. *Phys. Rev. B* **2007**, *76*, 245319.
- (23) Weymann, I.; Bulka, B. R.; Barnaś, J. Dark States in Transport through Triple Quantum Dots: The Role of Cotunneling. *Phys. Rev. B* **2011**, *83*, 195302.
- (24) Emary, C. Dark-States in Multi-Mode Multi-Atom Jaynes–Cummings Systems. *J. Phys. B: At., Mol. Opt. Phys.* **2013**, *46*, 224008.
- (25) Baratz, A.; Baer, R. Nonmechanical Conductance Switching in a Molecular Tunnel Junction. *J. Phys. Chem. Lett.* **2012**, *3*, 498–502.
- (26) Baratz, A.; White, A. J.; Galperin, M.; Baer, R. Effects of Electromagnetic Coupling on Conductance Switching of a Gated Tunnel Junction. *J. Phys. Chem. Lett.* **2014**, *5*, 3545–3550.
- (27) Blobner, F.; Coto, P. B.; Allegretti, F.; Bockstedte, M.; Rubio-Pons, O.; Wang, H.; Allara, D. L.; Zharnikov, M.; Thoss, M.; Feulner, P. Orbital-Symmetry-Dependent Electron Transfer through Molecules Assembled on Metal Substrates. *J. Phys. Chem. Lett.* **2012**, *3*, 436–440.
- (28) Talapin, D. V.; Lee, J.-S.; Kovalenko, M. V.; Shevchenko, E. V. Prospects of Colloidal Nanocrystals for Electronic and Optoelectronic Applications. *Chem. Rev.* **2010**, *110*, 389–458.

- (29) Kim, J. Y.; Voznyy, O.; Zhitomirsky, D.; Sargent, E. H. 25th Anniversary Article: Colloidal Quantum Dot Materials and Devices: A Quarter-Century of Advances. *Adv. Mater.* **2013**, *25*, 4986–5010.
- (30) Liljeroth, P.; Jdira, L.; Overgaag, K.; Grandidier, B.; Speller, S.; Vanmaekelbergh, D. Can Scanning Tunneling Spectroscopy Measure the Density of States of Semiconductor Quantum Dots? *Phys. Chem. Chem. Phys.* **2006**, *8*, 3845–3850.
- (31) Bekenstein, Y.; Vinokurov, K.; Levy, T. J.; Rabani, E.; Banin, U.; Millo, O. Periodic Negative Differential Conductance in a Single Metallic Nanocage. *Phys. Rev. B* **2012**, *86*, 085431.
- (32) Vortman, S.; Ben-dor, O.; Yochelis, S.; Amit, Y.; Paltiel, Y. Mapping the Energy Band Structure of Nanocrystal Monolayers under Ambient Conditions. *J. Phys. Chem. C* **2013**, *117*, 22245–22249.
- (33) Grinbom, G. A.; Saraf, M.; Saguy, C.; Bartnik, A. C.; Wise, F.; Lifshitz, E. Density of States in a Single PbSe/PbS Core–Shell Quantum Dot Measured by Scanning Tunneling Spectroscopy. *Phys. Rev. B* **2010**, *81*, 245301.
- (34) Nguyen, T. H.; Habinshuti, J.; Justo, Y.; Gomes, R.; Mahieu, G.; Godey, S.; Nys, J. P.; Carrillo, S.; Hens, Z.; Robbe, O.; Turrell, S.; Grandidier, B. Charge Carrier Identification in Tunneling Spectroscopy of Core–Shell Nanocrystals. *Phys. Rev. B* **2011**, *84*, 195133.
- (35) Liljeroth, P.; van Emmichoven, P. A. Z.; Hickey, S. G.; Weller, H.; Grandidier, B.; Allan, G.; Vanmaekelbergh, D. Density of States Measured by Scanning-Tunneling Spectroscopy Sheds New Light on the Optical Transitions in PbSe Nanocrystals. *Phys. Rev. Lett.* **2005**, *95*, 086801.
- (36) Liljeroth, P.; Jdira, L.; Overgaag, K.; Grandidier, B.; Speller, S.; Vanmaekelbergh, D. Can Scanning Tunneling Spectroscopy Measure the Density of States of Semiconductor Quantum Dots? *Phys. Chem. Chem. Phys.* **2006**, *8*, 3845–3850.
- (37) Vaxenburg, R.; Lifshitz, E. Alloy and Heterostructure Architectures as Promising Tools for Controlling Electronic Properties of Semiconductor Quantum Dots. *Phys. Rev. B* **2012**, *85*, 075304.
- (38) Williamson, A. J.; Grossman, J. C.; Hood, R. Q.; Puzder, A.; Galli, G. Quantum Monte Carlo Calculations of Nanostructure Optical Gaps: Application to Silicon Quantum Dots. *Phys. Rev. Lett.* **2002**, *89*, 196803.
- (39) Reimann, S. M.; Manninen, M. Electronic Structure of Quantum Dots. *Rev. Mod. Phys.* **2002**, *74*, 1283–1342.
- (40) Pozner, R.; Lifshitz, E.; Peskin, U. Charge Transport-Induced Recoil and Dissociation in Double Quantum Dots. *Nano Lett.* **2014**, *14*, 6244–6249.
- (41) Waugh, F. R.; Berry, M. J.; Mar, D. J.; Westervelt, R. M.; Campman, K. L.; Gossard, A. C. Single-Electron Charging in Double and Triple Quantum Dots with Tunable Coupling. *Phys. Rev. Lett.* **1995**, *75*, 705–708.
- (42) Romero, H. E.; Drndic, M. Coulomb Blockade and Hopping Conduction in PbSe Quantum Dots. *Phys. Rev. Lett.* **2005**, *95*, 156801.
- (43) Talapin, D. V.; Lee, J.-S.; Kovalenko, M. V.; Shevchenko, E. V. Prospects of Colloidal Nanocrystals for Electronic and Optoelectronic Applications. *Chem. Rev.* **2010**, *110*, 389–458.
- (44) Talapin, D. V.; Murray, C. B. PbSe Nanocrystal Solids for n- and p-Channel Thin Film Field-Effect Transistors. *Science* **2005**, *310*, 86–89.
- (45) Szabo, W. A.; Ostlund, W. N. S. *Modern Quantum Chemistry: Introduction to Advanced Electronic Structure Theory*; Dover Publications: Mineola, NY, 1996.
- (46) Meir, Y.; Wingreen, N. S.; Lee, P. A. Low-Temperature Transport through a Quantum Dot: The Anderson Model out of Equilibrium. *Phys. Rev. Lett.* **1993**, *70*, 2601–2604.
- (47) Peskin, U. An Introduction to the Formulation of Steady-State Transport through Molecular Junctions. *J. Phys. B: At., Mol. Opt. Phys.* **2010**, *43*, 153001.
- (48) Härtle, R.; Cohen, G.; Reichman, D. R.; Millis, A. J. Decoherence and Lead-Induced Interdot Coupling in Nonequilibrium Electron Transport through Interacting Quantum Dots: A Hierarchical Quantum Master Equation Approach. *Phys. Rev. B* **2013**, *88*, 235426.
- (49) Volkovich, R.; Hartle, R.; Thoss, M.; Peskin, U. Bias-Controlled Selective Excitation of Vibrational Modes in Molecular Junctions: A Route Towards Mode-Selective Chemistry. *Phys. Chem. Chem. Phys.* **2011**, *13*, 14333–14349.
- (50) Wunsch, B.; Braun, M.; König, J.; Pfannkuche, D. Probing Level Renormalization by Sequential Transport through Double Quantum Dots. *Phys. Rev. B* **2005**, *72*, 205319.
- (51) Notice that in the third column of Table 2, there is a unique situation in which a backward transition of electrons to the tip takes place. The tip chemical potential lies above $\epsilon_1 + U$ and below $\epsilon_2 + U$. Therefore, there is enough energy to populate the doubly occupied energy level from the ϵ_2 state but not from the ϵ_1 state. Yet, back transitions from the doubly occupied state to the ϵ_1 state are Pauli-allowed, and therefore, electrons can transit back to the tip. The third column illustrates the openings of a new channel for transport from the ϵ_2 state to the doubly occupied state. The fourth column corresponds to a higher bias, where the back transitions become Pauli-blocked while the forward transitions from the ϵ_1 state to the doubly occupied state become allowed (the third and fourth columns are energetically accessible channels for transport, but they do not contribute to the current due to the decoupling of the ϵ_2 state from the leads).
- (52) Foster, T. J.; Leadbeater, M. L.; Eaves, L.; Henini, M.; Hughes, O. H.; Payling, C. A.; Sheard, F. W.; Simmonds, P. E.; Toombs, G. A.; Hill, G.; Pate, M. A. Current Bistability in Double-Barrier Resonant-Tunneling Devices. *Phys. Rev. B* **1989**, *39*, 6205–6207.
- (53) Koester, S. J.; Ismail, K.; Lee, K. Y.; Chu, J. O. Negative Differential Conductance in Lateral Double-Barrier Transistors Fabricated in Strained Si Quantum Wells. *Appl. Phys. Lett.* **1997**, *70*, 2422–2424.
- (54) Peskin, U. Analysis of a Dissipative Resonant Tunneling Trap by Temperature-Dependent Langevin–Schrodinger Equations. *J. Chem. Phys.* **2000**, *113*, 7479–7487.
- (55) van der Wiel, W. G.; De Franceschi, S.; Elzerman, J. M.; Fujisawa, T.; Tarucha, S.; Kouwenhoven, L. P. Electron Transport through Double Quantum Dots. *Rev. Mod. Phys.* **2002**, *75*, 1–22.
- (56) Ziegler, R.; Bruder, C.; Schoeller, H. Transport through Double Quantum Dots. *Phys. Rev. B* **2000**, *62*, 1961–1970.

6.3 Triple Quantum Dot NEMS Memory Device (2015)

A triple quantum dot based nano-electromechanical memory device

R. Pozner,^{1,2,3} E. Lifshitz,^{1,2,3} and U. Peskin^{1,3,4,a)}

¹Schulich Faculty of Chemistry, Technion-Israel Institute of Technology, Haifa 32000, Israel

²Solid State Institute, Technion-Israel Institute of Technology, Haifa 32000, Israel

³Russell Berrie Nanotechnology Institute, Technion-Israel Institute of Technology, Haifa 32000, Israel

⁴Lise Meitner Center for Computational Quantum Chemistry, Technion-Israel Institute of Technology, Haifa 32000, Israel

(Received 18 June 2015; accepted 29 August 2015; published online 18 September 2015)

Colloidal quantum dots (CQDs) are free-standing nano-structures with chemically tunable electronic properties. This tunability offers intriguing possibilities for nano-electromechanical devices. In this work, we consider a nano-electromechanical nonvolatile memory (NVM) device incorporating a triple quantum dot (TQD) cluster. The device operation is based on a bias induced motion of a floating quantum dot (FQD) located between two bound quantum dots (BQDs). The mechanical motion is used for switching between two stable states, “ON” and “OFF” states, where ligand-mediated effective interdot forces between the BQDs and the FQD serve to hold the FQD in each stable position under zero bias. Considering realistic microscopic parameters, our quantum-classical theoretical treatment of the TQD reveals the characteristics of the NVM. © 2015 AIP Publishing LLC. [<http://dx.doi.org/10.1063/1.4930826>]

The demand for increased nonvolatile and random access memory (RAM) in very large scale integrated circuit (VLSI) architectures has pushed the silicon complementary metal-oxide-semiconductor (CMOS) fabrication scaling to its limit over the past few decades with regard to physical, material, and operational limitations.¹ The current dominating nonvolatile memory (NVM) devices are FLASH devices which are based on CMOS processes.^{2,3} The on-going miniaturization has also enabled the fabrication of nano-electromechanical systems (NEMS) with sub- μm long structures functioning as NVM devices. Those currently include suspended floating beam formed as a gate of an MOSFET structure,^{4–6} vertically aligned carbon nanotube (MWCNT),⁷ suspended carbon nanotube,⁸ and anchor-less shuttle devices.⁹

The operation frequency of typical NEMS devices are inversely proportional to their characteristic (decreasing) size,^{5,10} and therefore NEMS have the potential to achieve a very high operation speeds of several gigahertz. Beside operating speeds, NEMS can achieve very low standby leakage current.^{7,9} Moreover, switching between “ON” and “OFF” states in NEMS can be achieved with a narrow bias difference, and therefore, the switching power has the potential to be reduced significantly in comparison with the FLASH devices. NEMS devices can also potentially work in a wide range of temperatures.^{9,11,12} Last, operation of NEMS is usually not associated with charge tunneling through a gate oxide and therefore the limitation of gate oxide deterioration does not arise, which is an aspect causing the eventual dying of conventional FLASH devices. However, internal stress of the cantilever/beam⁵ needs to be taken into account for the assessment of NEMS lifecycle. Traditional FLASH devices as well as current state of the art NEMS memory devices are most often modeled using three-dimensional finite element methods (FEM) approaches.^{5,9,13} In the case of the NEMS devices, a combination of electrostatic and mechanical aspects is often applied (using, for example,

COMSOL, TCAD, ADVENTURE software packages) for solving the Poisson’s (drift-diffusion) and Navier’s set of equations simultaneously; while in conventional FLASH devices, there is no need to take the mechanical aspect into consideration.

In this article, we consider a NEMS memory device, incorporating a triple quantum dot (TQD) structure constructed of colloidal quantum dots (CQDs), which is based on the effect of (I) double quantum dots (DQD) dissociation¹⁴ and (II) negative differential resistance (NDR).¹⁵ CQDs, synthesized using “wet chemistry” techniques,¹⁶ offer possibilities for innovating NEMS devices by exploiting mechanical motion on the nano-scale. The unique size and material versatility and also the ability to manipulate the surrounding capping ligands^{16,17} of CQDs are a key for the realization of such class of devices. The TQD NEMS device does not incorporate a MOS junction hence no inversion, accumulation, or depletion regions exist nor any moving/bending cantilever/beam exists like in other NEMS devices. Moreover, in comparison with the above mentioned NEMS, at least a semi-classical approach is needed in order to model the inherent quantum-classical phenomena and the coupled electro-mechanical dynamics of the TQD NEMS device. Therefore, standard FEM solutions would not be satisfactory for the characterization of this device which relies on the quantum nature of the underlying phenomena.

The TQD NEMS device, illustrated in Fig. 1, consists of 3 CQDs, 2 bound quantum dots (BQD) at the edges (dots A and C), and 1 floating quantum dot (FQD) between them (dot B). The device can be conceptually divided into two isolated sub-systems, a left configuration where the FQD is on the left (dots A and B) and a right configuration where the FQD is on the right (dots B and C). This treatment is justified under the assumption of zero interaction between the 2 BQDs.

Each of the 3 dots is represented by a single localized spin orbital, given the following assumptions: (i) Degeneracies of the neutral quantum dot orbitals are removed upon charging by an extra electron,^{18,19} (ii) multiple charging of each dot is excluded due to intra-dot Coulomb interaction, (iii) spin is conserved during transport and a single spin model is sufficient,

^{a)}Also at Lise Meitner Center for Computational Quantum Chemistry. Electronic mail: uri@tx.technion.ac.il.

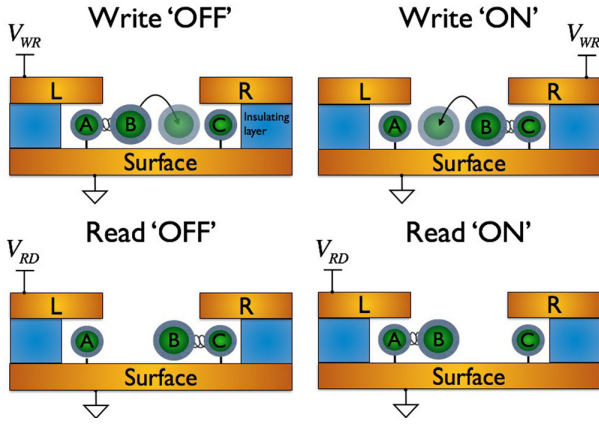


FIG. 1. TQD NEMS device operation. A “write command” is executed by applying V_{WR} voltage on the left or right contact for switching from an ‘ON’ to an ‘OFF’ state and vice versa, respectively. The reset operation is executed by applying V_{WR} on the right dot. Read command is applied by setting V_{RD} on the left dot.

(iv) electronic interactions during double occupancy of each sub-system structure are fully accounted for, and (v) detailed structure of the electronic envelope functions, as well as the rapid oscillations associated with the semiconductor periodicity, are disregarded but can be readily included for CQDs of specific shape and chemical compositions.

The single dot orbitals are modeled as 3D Gaussians, $\chi_{A/B/C}(r) = \left(\frac{1}{2\sigma^2\pi}\right)^{3/4} e^{-\frac{1}{2\sigma^2}(r-R_{A/B/C})^2}$, where R_A , R_B , and R_C are the dots center of mass coordinates and r is the electronic coordinate. The dots dimensions are captured in σ , the standard deviation of the respective probability distributions, $|\chi_{A/B/C}(r)|^2$. The three dots are assumed to have a collinear configuration (which can be realized by confining them in a linear trench on the surface). Setting $R_A \equiv (0, 0, q_A)$, $R_B \equiv (0, 0, q_B)$, and $R_C \equiv (0, 0, q_C)$, the interdot distances, $|R_A - R_B| = q_{AB}$ and $|R_C - R_B| = q_{BC}$, define the overlap between each two adjacent localized orbitals, $S_{AB}(q_{AB}) = \int dr \chi_A(r) \chi_B(r) e^{-\frac{q_{AB}^2}{8\sigma^2}}$ and $S_{BC}(q_{BC}) = \int dr \chi_B(r) \chi_C(r) e^{-\frac{q_{BC}^2}{8\sigma^2}}$. Based on the assumption of zero interaction between the BQDs, the overlap between their orbitals is zero, $S_{AC} \rightarrow 0$. Thereby, the effective single electron Hamiltonian matrix in the basis of $\chi_{A/B/C}(r)$, is assumed to take the following generic form:

$$\mathbf{H}(q_{AB}, q_{BC}) = \begin{pmatrix} E_A & t_0 e^{-\gamma(q_{AB}-q_{0AB})} & 0 \\ t_0 e^{-\gamma(q_{AB}-q_{0AB})} & E_B & t_0 e^{-\gamma(q_{BC}-q_{0BC})} \\ 0 & t_0 e^{-\gamma(q_{BC}-q_{0BC})} & E_C \end{pmatrix}, \quad (1)$$

$$\mathbf{S}(q_{AB}, q_{BC}) = \begin{pmatrix} 1 & S_{AB}(q_{AB}) & 0 \\ S_{AB}(q_{AB}) & 1 & S_{BC}(q_{BC}) \\ 0 & S_{BC}(q_{BC}) & 1 \end{pmatrix}, \quad (2)$$

where E_A , E_B , and E_C are considered the LUMO energies when the dots are separated. The electronic coupling set by the dot boundaries and the surrounding ligands^{16,17} is assigned a typical exponential decay form, where q_{0AB} and q_{0BC} are the interdot distances in the absence of potential bias.

Following the condition $S_{AC} \rightarrow 0$ and by assuming full dephasing during the process of switching from one sub-system to the other, each sub-system can be treated in isolation. Thereby, it is constructive to define a parameter q as

$$\begin{cases} q \cong q_{AB} - q_{0AB} & \text{for } q < 0 \\ q \cong q_{0BC} - q_{BC} & \text{for } q > 0. \end{cases}$$

Using q , the effective single electron Hamiltonian matrix for the left and right sub-systems takes the following form:

$$\mathbf{H}_L(q, q < 0) = \begin{pmatrix} E_A & t_0 e^{-\gamma q} \\ t_0 e^{-\gamma q} & E_B \end{pmatrix}, \quad (3)$$

$$\mathbf{H}_R(q, q > 0) = \begin{pmatrix} E_B & t_0 e^{-\gamma q} \\ t_0 e^{-\gamma q} & E_C \end{pmatrix}, \quad (4)$$

and

$$\mathbf{S}(q) = \begin{pmatrix} 1 & S(q) \\ S(q) & 1 \end{pmatrix}. \quad (5)$$

The single particle energies as functions of the interdot distance of each sub-system, $\epsilon_1(q)$ and $\epsilon_2(q)$, can be calculated using the generalized linear variation principle,²⁰ $\mathbf{H}(q)\mathbf{C}(q) - \mathbf{S}(q)\mathbf{C}(q)\epsilon(q) = 0$. The coefficients matrix for the left sub-system is

$$\mathbf{C}_L(q) = \begin{pmatrix} c_{A1}(q) & c_{A2}(q) \\ c_{B1}(q) & c_{B2}(q) \end{pmatrix}, \quad (6)$$

where the respective orthonormal orbitals are

$$\begin{aligned} \phi_{1,L}(q, r) &= c_{A1}(q)\chi_A(r) + c_{B1}(q)\chi_B(r), \\ \phi_{2,L}(q, r) &= c_{A2}(q)\chi_A(r) + c_{B2}(q)\chi_B(r), \end{aligned} \quad (7)$$

and similarly for the right sub-system. The orthonormal orbitals define an electronic Fock space.

Finally, the projection of the Hamiltonian onto each sub-system space reads, $\hat{H}_{SUB} = \epsilon_1(q)\hat{a}_1^\dagger\hat{a}_1 + \epsilon_2(q)\hat{a}_2^\dagger\hat{a}_2 + U(q)\hat{a}_1^\dagger\hat{a}_1\hat{a}_2^\dagger\hat{a}_2 + \frac{p^2}{2\mu} + V(q)$ where $U(q)$ is a two particle interaction term (Coulomb and exchange) and \hat{a}_m^\dagger is a creation operator for an electron in the m^{th} orbital. μ is the reduced mass of either sub-system, p is the momentum associated with the interdot motion, and $V(q)$ reflects the interdot mechanical bindings potential.

The mechanical binding potential between the FQD and each BQD is attributed to overall interdot ligands and dot-surface ligands interactions.^{16,21,22} The details of the mechanical interaction depend on these specificities and should reflect a universal short-range repulsion and a weak long-term attraction between the ligands. Therefore, a generic Morse potential for each sub-system was chosen, as illustrated in Fig. 2. Based on the condition $S_{AC} \rightarrow 0$, the binding energy for each sub-system is unaffected by the contribution of the remote parts, hence $V(q)$ for each sub-system reduces to the following form:

$$V(q) = D(e^{-2\alpha q} - 2e^{-\alpha q} + 1), \quad (8)$$

where D and α are, respectively, the interdot binding energy and interaction range parameters, which control the

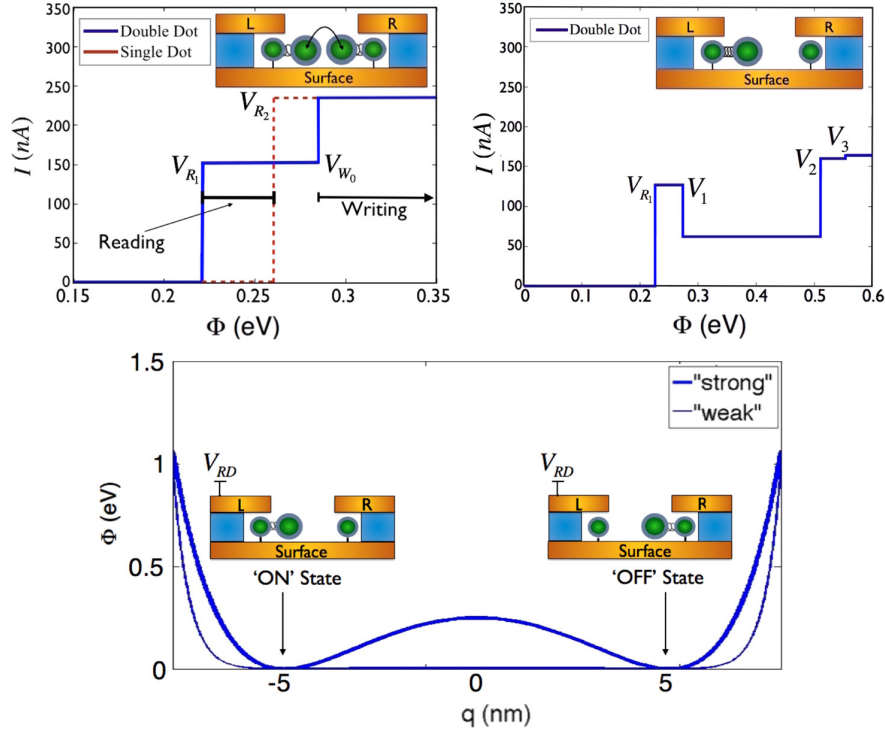


FIG. 2. *Top left*: Current vs. bias potential for weak mechanical binding. The blue curve reflects a transition from DQD to an SQD with increasing voltage at the appropriate lead (see inset). The red curve represents the current through a single dot. The differences between the blue and red curves enable the operations of the NEMS device. The two curves coalesce after a switching response, at 0.276 eV. The voltage range between V_{R_1} and V_{R_2} is the potential bias margin for a “read command” while a bias potential above V_{W_0} is used to execute a write command. *Top right*: Current vs. bias potential for strong mechanical binding. The blue curve reflects the current through a “rigid” DQD, excluding the possibility of a write command. In both cases, the interdot distance for zero bias potential is 5σ , and the asymmetry parameter ($E_A - E_B$ or $E_C - E_B$) is 0.02[eV]. *Bottom*: Effective binding potential for the FQD with two equilibriums positions at $V(-5\sigma) = V(5\sigma) = 0$. The thick and thin curves are associated with strong and weak mechanical interactions, $V(-3\sigma) = V(3\sigma) = 0.25$ eV, 0.0025 eV, respectively.

transition from “weak” to “strong” binding potentials (see Ref. 14 for elaborate discussion on the different mechanical bindings potentials).

The BQDs are coupled electronically to the top contacts (L,R) and to the surface (S) while the FQD is coupled only to the surface (see Fig. 1.) This idealization is assumed for simplicity, but the following analysis applies as long as the coupling of the top contacts to the BQDs is significantly larger than their coupling to the FQD. (This difference is important in order to avoid decoupling of the DQDs from the top contacts due to destructive interference.¹⁵) All contacts are regarded as reservoirs of non-interacting electrons,²³ $\hat{H}_{leads} = \sum_{K=L,R,S} \sum_{k \in K} \epsilon_{k,K} \hat{b}_{k,K}^\dagger \hat{b}_{k,K}$, where $\hat{b}_{k,K}^\dagger$ is the creation of electron in the k^{th} state of the K^{th} reservoir. The coupling between the reservoirs and the dots in each sub-system corresponds to electron hopping between the localized orbitals ($\chi_A(r)$ and $\chi_B(r)$ for the left sub-system or $\chi_B(r)$ and $\chi_C(r)$ for the right sub-system) and the lead states, $\hat{H}_{SUB-leads} = \sum_{n=1,2} \sum_{K=L/R,S} \sum_{k \in K} u_{k,K} \eta_{n,K} \hat{d}_n \hat{b}_{k,K}^\dagger + h.c.$, where \hat{d}_n is the annihilation operator of an electron at the n^{th} dot site. $\eta_{n,K}$ equals one or zero if the K^{th} contact is coupled or uncoupled to the n^{th} dot, respectively.

Finally, the full Hamiltonian of each sub-system reads

$$\hat{H} = \hat{H}_{SUB} + \hat{H}_{leads} + \hat{H}_{leads-SUB}. \quad (9)$$

For typical electronic tunneling barriers between each one of the BQDs and the top contact, and between each sub-

system and the surface, the electronic coupling of the DQD to the lead is weak and the dynamics of the sub-system density can be solved using the reduced density matrix approach.²⁴ The mechanical motion is treated classically using canonical position and momentum equations. The steady-state response of each sub-system to an applied bias voltage is associated with a self-consistent solution of coupled electromechanical dynamical equations.¹⁴ The switching response properties between the two sub-systems and the current through each sub-system are derived using this methodology.

The TQD NEMS device is operated by write and read commands. The “write command” (Fig. 1, upper row) controls the switching between the left and right sub-system configurations. By applying a write command on the left contact, the FQD floats to the right (if it wasn’t already there before) and an OFF state is set, and by applying a write command on the right contact, the FQD floats to the left and an ON state is set (this operation also serves as a “reset command”). The “read command” (Fig. 1, bottom row) is executed by probing the current between the left and surface contacts and it depends on the specific state of the device. In particular, a reading command will probe the current through either a single quantum dot (SQD) or a double quantum dot (DQD). Indeed, the onset of the current is different in the two cases: in the SQD it reflects the charging energy of a single dot, and in a DQD it is shifted to a lower voltage, which corresponds to charging of a delocalized electronic state of

the DQD.^{14,15} (Notice that quantum delocalization between the two dots requires that coherence is preserved within the DQD. Heat production during read command may hinder this coherence and should be efficiently removed in order to distinguish the DQD from the SQD).

The $I-V$ curve of either sub-system configuration ($I_{L \rightarrow S}$ or $I_{R \rightarrow S}$) for weak mechanical binding (Fig. 2, bottom) is shown in Fig. 2, top left. The blue solid curve and the red dashed curve indicate the current before and after a write command, respectively. The write and read commands should be executed using two potential bias margins, V_{WR} and V_{RD} , respectively. The write command (Table I, 1st and 2nd rows) is executed by applying a voltage $V_{WR} > V_{W_0}$ (Fig. 2, top left, blue curve) at the appropriate lead, where V_{W_0} is the second step in the current of the DQD. It is possible to verify the device state by applying a read command before a write command. However, it is also possible to execute a write command without prior knowledge of the device state. The read command (Table I, 3rd row) is applied at the voltage range $V_{R_2} > V_{RD} > V_{R_1}$ (Fig. 2, top left), where V_{R_1} is the first step in the current of the DQD and V_{R_2} is the single voltage threshold of the SQD. Measurement of the current before a mechanical floating response implies charge transport through two dots and high current probing, corresponding to an ON state, while measurement of the current after a mechanical response implies charge transport through a single dot and zero current, corresponding to an OFF state.

The most crucial consideration for the proper operation of the TQD device is the degree of the interdot mechanical binding strength (Fig. 2, bottom). In comparison to the weak mechanical binding case (Fig. 2, top left), setting V_{WR} on the top contacts in the strong mechanical binding regime does not lead to a mechanical response of the FQD, and therefore, hinders the use of the device. Indeed, according to the analysis of Ref. 14, relatively small binding force constants are required for DQD dissociation. This estimate was derived when the dissociation was dominated by single-electron delocalization forces. However, the onset of many body repulsion effects (which prevail at higher voltages) should enable DQD dissociation also for much larger binding force constants. In any case, since the FQD mobility is sensitive to the ligand and surface mediated binding forces, it is necessary to ensure the proper operation of the device by verifying the switching response between the two sub-system (DQDs) configurations. This kind of check-up can be performed during the validation phase of the manufacturing process. The $I-V$ curve for a strong mechanical binding potential is shown in Fig. 2, top right. The jump in the current at V_{R_1} is similar to the one observed for weak mechanical binding (Fig. 2, top left), however, for higher bias potentials, the next

step at V_1 leads to a current drop, also known as NDR. This drop occurs due to the unique connectivity of the dots in the device, where all the dots are connected to a shared surface and only the BQDs are connected to the top contacts (Fig. 1.) This effect, discussed extensively in Ref. 15, leads to the above mentioned NDR. Observing this signature of NDR while scanning a range of potentials indicates the existence of mechanical binding potential which is too stiff for proper operation. Notice that the two-electrons transport channels, ensued at bias potentials V_2 and V_3 , are only accessible in the strong mechanical binding case.

An additional important phenomenon which exists in most conventional NEMS NVMs is a mechanical bistability of a cantilever.^{5,10,25-27} Managing this bistability is an essential part of achieving a functioning memory device. The bistability is accompanied by the existence of a hysteresis in the $I-V$ curve. The motivation is to reduce the switching voltage (difference between ON and OFF switching voltages) without impairing the beam/cantilever displacement ability which control the ON/OFF currents ratio. The TQD NEMS device proposed here does not suffer from such a trade-off because the switching voltage is applied on two separate voltage lines (the left and right contacts). One can thus say that the TQD NEMS device can achieve ideal switching or has “infinite” hysteresis because the switching voltage is not voltage dependent but distance dependent. In addition, because the ON or OFF states are not affected by charging effects, but rather by a mechanical effect, no current leakage is expected.

Finally, we estimate the write command operation frequency for the proposed device. The switching speed depends on the timescale of DQD dissociation (transition from a DQD to a SQD). A rough estimate of the switching speed can be based on the inter-dot oscillation frequency, $\frac{2\pi}{T} = \sqrt{\frac{K}{\mu}}$, where K is the mechanical binding force, which ideally takes the highest value that still enables dissociation. Considering the values $K \approx 10^{-2}$ [N/m], and $\mu \approx 10^{-22}$ [Kg] (see Ref. 14), the resultant frequency is $f \approx 1$ GHz. This estimation for the switching frequency is higher than that of current non-volatile FLASH memory devices. Reducing the length of the interdot capping ligands or changing their inner atomistic structure could lead to a modification of the shape of the mechanical binding potential (Fig. 2, bottom) with an overall increase of K . This is expected to farther increase the switching speed, provided that the increase in the inter-dot binding force would not prevent the DQD dissociation. However, minimizing the inter-dot distance is likely to amplify the interaction between the BQDs and may alter the operation of the device. Dealing with these effects is out of the scope of the present article and will be investigated in the future.

In conclusion, a setup is proposed for a TQD NEMS memory device based on the motion of a floating CQD. The coupling between the dots in the device is accounted for by considering explicitly the dependence of the electronic terms on the interdot distance. In particular, the single electron (tunneling) coupling and the many body (Coulomb and exchange) interaction terms are calculated self-consistently with an interdot mechanical response within a mixed quantum-classical

TABLE I. Operating principles of the TQD NEMS device.

Logic	Voltages	Operation
Write “ON”	$V_L = V_{WR}; V_R = 0$	Switch to right sub-system
Write “OFF”	$V_L = 0; V_R = V_{WR}$	Switch to left sub-system
Read	$V_L = V_{RD}; V_R = 0$	Read ON or OFF states
Hold	$V_L = 0; V_R = 0$	NULL

reduced density matrix formulation. The characteristics of the device were studied for different interdot mechanical binding potential strengths. Further characterization of other physical parameters will be explored in future studies. Finally, the proposed device is estimated to work at very high frequencies (higher than 1 GHz according to our rough estimate) and it also has the potential to exhibit large ON/OFF current ratios together with low switching power demands as well as zero hysteresis, zero mechanical bistability, and zero leakage currents.

This research was supported by the German Israeli Foundation Grant 1154-119.5/2011 (U.P.). The research work at E.L. laboratory was supported by the Volkswagen Stiftung - Project 88116, the Niedersachsen-Deutsche Technion Gesellschaft E.V - Project ZN2916, and the Focal Area Technology (FTA) - Council For Higher Education - Project 872967. R.P. acknowledges the support by the Nancy & Stephan Grand Technion Energy Program (GTEP) center.

- ¹E. Vatajelu, H. Aziza, and C. Zambelli, in *9th International Design Test Symposium (IDT)* (2014), pp. 61–66.
- ²Y. Park, J. Lee, S. S. Cho, G. Jin, and E. Jung, in *IEEE International Reliability Physics Symposium* (2014), pp. 2E.1.1–2E.1.4.
- ³P.-Y. Du, H.-T. Lue, Y.-H. Shih, K.-Y. Hsieh, and C.-Y. Lu, in *12th IEEE International Conference on Solid-State and Integrated Circuit Technology (ICSICT)* (2014), pp. 1–4.
- ⁴T. Nagami, Y. Tsuchiya, K. Uchida, H. Mizuta, and S. Oda, *Jpn. J. Appl. Phys.* **49**, 044304 (2010).
- ⁵Y. Tsuchiya, K. Takai, N. Momo, T. Nagami, H. Mizuta, S. Oda, S. Yamaguchi, and T. Shimada, *J. Appl. Phys.* **100**, 094306 (2006).
- ⁶K. Lee and W. Y. Choi, *IEEE Trans. Electron Devices* **58**, 1264 (2011).

- ⁷J. E. AU Jang, S. N. Cha, Y. J. Choi, D. J. Kang, T. P. Butler, D. G. Hasko, J. E. Jung, J. M. Kim, and G. A. J. Amaratunga, *Nature Nanotechnol.* **3**, 26 (2008).
- ⁸S. N. Cha, J. E. Jang, Y. Choi, G. A. J. Amaratunga, D.-J. Kang, D. G. Hasko, J. E. Jung, and J. M. Kim, *Appl. Phys. Lett.* **86**, 083105 (2005).
- ⁹V. Pott, G. L. Chua, R. Vaddi, J.-L. Tsai, and T. Kim, *IEEE Trans. Electron Devices* **59**, 1137 (2012).
- ¹⁰T. Nagami, Y. Tsuchiya, S. Saito, T. Arai, T. Shimada, H. Mizuta, and S. Oda, *Jpn. J. Appl. Phys.* **48**, 114502 (2009).
- ¹¹J. Gopal, A. T. Do, P. Singh, G. L. Chua, and T.-H. Kim, *IEEE Trans. Electron Devices* **61**, 2177 (2014).
- ¹²R. Vaddi, T. Kim, V. Pott, and J. Lin, in *IEEE International Reliability Physics Symposium (IRPS)* (2012), pp. ME.3.1–ME.3.6.
- ¹³A. Lazarus, T. Barois, S. Perisanu, P. Poncharal, P. Manneville, E. de Langre, S. T. Purcell, P. Vincent, and A. Ayari, *Appl. Phys. Lett.* **96**, 193114 (2010).
- ¹⁴R. Pozner, E. Lifshitz, and U. Peskin, *Nano Lett.* **14**, 6244 (2014).
- ¹⁵R. Pozner, E. Lifshitz, and U. Peskin, *J. Phys. Chem. Lett.* **6**, 1521 (2015).
- ¹⁶D. V. Talapin, J.-S. Lee, M. V. Kovalenko, and E. V. Shevchenko, *Chem. Rev.* **110**, 389 (2010).
- ¹⁷D. V. Talapin and C. B. Murray, *Science* **310**, 86 (2005).
- ¹⁸F. R. Waugh, M. J. Berry, D. J. Mar, R. M. Westervelt, K. L. Campman, and A. C. Gossard, *Phys. Rev. Lett.* **75**, 705 (1995).
- ¹⁹H. E. Romero and M. Drndic, *Phys. Rev. Lett.* **95**, 156801 (2005).
- ²⁰A. Szabo and N. S. Ostlund, *Modern Quantum Chemistry: Introduction to Advanced Electronic Structure Theory* (Dover Books on Chemistry Series, Dover Publications: Mineola, NY, 1996).
- ²¹D. A. Hines and P. V. Kamat, *J. Phys. Chem. C* **117**, 14418 (2013).
- ²²K. J. Williams, W. A. Tisdale, K. S. Leschkies, G. Haugstad, D. J. Norris, E. S. Aydil, and X.-Y. Zhu, *ACS Nano* **3**, 1532 (2009).
- ²³Y. Meir, N. S. Wingreen, and P. A. Lee, *Phys. Rev. Lett.* **70**, 2601 (1993).
- ²⁴U. Peskin, *J. Phys. B: Atom., Mol. Opt. Phys.* **43**, 153001 (2010).
- ²⁵K. J. Ziegler, D. M. Lyons, J. D. Holmes, D. Ertz, B. Polyakov, H. Olin, K. Svensson, and E. Olsson, *Appl. Phys. Lett.* **84**, 4074 (2004).
- ²⁶B. W. Soon, E. Jiaqiang Ng, Y. Qian, N. Singh, M. Julius Tsai, and C. Lee, *Appl. Phys. Lett.* **103**, 053122 (2013).
- ²⁷B. Charlot, W. Sun, K. Yamashita, H. Fujita, and H. Toshiyoshi, *J. Micromech. Microeng.* **18**, 045005 (2008).

Chapter 7

Results Clarifications and Extensions

In this chapter we extend some of the explanations and important derivations which appeared in the articles section at chapter 6. For brevity, we shall refer to the three papers presented above in Chapters 6.1, 6.2, 6.3 as Refs. 1, 2, 3, respectively.

7.1 Self consistent solution of QME with Canonical Classical Forces

In Ref. 1, the mechanical motion is treated using classical mechanics. It is important to clarify why this motion can be represented by classical terms.

Let's assume a typical QD mass of $m = 10^5[amu] = 1.6 \times 10^{-22}[Kg]$ and that the mechanical binding potential, a Morse potential, can be approximated to a parabolic function. Lastly, a typical energy difference, $\Delta\epsilon$, between the single particle orbitals is of the order of $0.1[eV]$.

Treatment of this problem using quantum mechanics would require the use of the position operator $q = \sqrt{\frac{\hbar\omega}{K}}(c^\dagger + c)$. As stated in the conclusion of the article, an interdot binding force constant smaller than $K = 0.01\frac{eV}{nm^2}$ would lead to dissociation, hence $\hbar\omega$, where $\omega = \sqrt{\frac{K}{m}}$, equals $3 \times 10^{-6}eV$. It follows that $\sqrt{\frac{\hbar\omega}{K}}$ equals $\sqrt{3} \times 10^{-2}[nm]$.

Therefore, in order to induce a motion of $\Delta q = 1[nm]$, the use of at least 10^2 states would be required. Taking into consideration the typical margin of $\Delta\epsilon$, these states are quasi-continuous and therefore should be treated classically.

Hereon, we elaborate on the classical treatment which is the cornerstone of the derivation which appear in Ref. 1, Eq. 4. The reduced system Hamiltonian (Ref. 1, Eq. 3) is,

$$\hat{H}_S = \epsilon_1(q)a_1^\dagger a_1 + \epsilon_2(q)a_2^\dagger a_2 + U(q)a_1^\dagger a_1 a_2^\dagger a_2 + \frac{P^2}{2m} + V(q) \quad (7.1)$$

and by depicting explicit expression of the density in a matrix form, ρ_S , with coherences between the single-particle terms,

$$\rho_S = \begin{pmatrix} \rho_{11} & 0 & 0 & 0 \\ 0 & \rho_{22} & \rho_{23} & 0 \\ 0 & \rho_{32} & \rho_{33} & 0 \\ 0 & 0 & 0 & \rho_{44} \end{pmatrix} \quad (7.2)$$

the condition for the steady state solution, $\langle \frac{d\hat{H}_S}{dq} \rangle = tr[\rho_S \frac{d\hat{H}_S}{dq}] = 0$ (as explained in the section below Eq. 3 in Ref .1), can be analyzed. We proceed by writing the derivative of the system Hamiltonian in a matrix form,

$$\begin{array}{cccc} |00\rangle & |01\rangle & |10\rangle & |11\rangle \\ \left(\begin{array}{cccc} \boxed{-\frac{d}{dq}V(q)} & 0 & 0 & 0 \\ 0 & \boxed{-\frac{d}{dq}V(q) + \frac{d}{dq}\epsilon_1(q)} & \boxed{-\langle\varphi_2(q)|\frac{d}{dq}\varphi_1(q)\rangle(\epsilon_1(q) - \epsilon_2(q))} & 0 \\ 0 & \boxed{-\langle\varphi_2(q)|\frac{d}{dq}\varphi_1(q)\rangle(\epsilon_2(q) - \epsilon_1(q))} & \boxed{-\frac{d}{dq}V(q) + \frac{d}{dq}\epsilon_2(q)} & 0 \\ 0 & 0 & 0 & \boxed{-\frac{d}{dq}V(q) + \frac{d}{dq}\epsilon_1(q) + \frac{d}{dq}\epsilon_2(q) + \frac{d}{dq}U(q)} \end{array} \right) \begin{array}{l} |00\rangle \\ |01\rangle \\ |10\rangle \\ |11\rangle \end{array} \end{array}$$

FIGURE 7.1: The diagonal red terms are adiabatic force terms and the non-diagonal blue terms are non-adiabatic force terms.

the diagonal terms are adiabatic forces terms representing force due to the population on each DQD eigenstate, and the non-diagonal terms are non-adiabatic force terms representing forces due to population transfer between different DQD eigenstates.

As stated in Ref. 1, the relatively large DQD eigenvalues separation and the electronic interactions that exceed the level broadening induced by the DQD-leads coupling and temperature leads to rapid decoherence [77]. Hence coherences can be neglected at

steady state and the density matrix becomes diagonal at steady state (this is the well known secular approximation). Finally, the non-adiabatic force terms can be ignored under the trace and the expression for $\langle \frac{d\hat{H}_S}{dq} \rangle$ follows,

$$\langle \frac{d\hat{H}_S}{dq} \rangle = 0 = \epsilon_1'(q)\langle a_1^\dagger a_1 \rangle_q + \epsilon_2'(q)\langle a_2^\dagger a_2 \rangle_q + U'(q)\langle a_1^\dagger a_1 a_2^\dagger a_2 \rangle_q + V'(q)\hat{I} \quad (7.3)$$

And the matrix form of Eq. 7.3 is the following,

$$\begin{aligned} \langle \frac{d\hat{H}_S}{dq} \rangle &= \epsilon_1'(q)\text{tr}[\rho a_1^\dagger a_1] + \epsilon_2'(q)\text{tr}[\rho a_2^\dagger a_2] + U'(q)\text{tr}[\rho a_1^\dagger a_1 a_2^\dagger a_2] + V'(q)\text{tr}[I] = \\ &\epsilon_1'(q)\text{tr} \begin{pmatrix} 0 & 0 & 0 & 0 \\ 0 & P_{10} & 0 & 0 \\ 0 & 0 & 0 & 0 \\ 0 & 0 & 0 & P_{11} \end{pmatrix} + \epsilon_2'(q)\text{tr} \begin{pmatrix} 0 & 0 & 0 & 0 \\ 0 & 0 & 0 & 0 \\ 0 & 0 & P_{01} & 0 \\ 0 & 0 & 0 & P_{11} \end{pmatrix} + \\ &U'(q)\text{tr} \begin{pmatrix} 0 & 0 & 0 & 0 \\ 0 & 0 & 0 & 0 \\ 0 & 0 & 0 & 0 \\ 0 & 0 & 0 & P_{11} \end{pmatrix} + V'(q)\text{tr} \begin{pmatrix} P_{00} & 0 & 0 & 0 \\ 0 & P_{10} & 0 & 0 \\ 0 & 0 & P_{01} & 0 \\ 0 & 0 & 0 & P_{11} \end{pmatrix} = \\ &\text{tr} \begin{pmatrix} P_{00}E'_{00}(q) & 0 & 0 & 0 \\ 0 & P_{10}E'_{10}(q) & 0 & 0 \\ 0 & 0 & P_{01}E'_{01}(q) & 0 \\ 0 & 0 & 0 & P_{11}E'_{11}(q) \end{pmatrix} \end{aligned} \quad (7.4)$$

where

$$\begin{cases} E_{00}(q) = V(q) \\ E_{10}(q) = V(q) + \epsilon_1(q) \\ E_{01}(q) = V(q) + \epsilon_2(q) \\ E_{11}(q) = V(q) + \epsilon_1(q) + \epsilon_2(q) + U(q) \end{cases} \quad (7.5)$$

and after some more algebra, we finally derive the relation from Ref. 1, Eq. 4,

$$-\langle \frac{dH_S}{dq} \rangle = -[P_{00}(q)E'_{00}(q) + P_{10}(q)E'_{10}(q) + P_{01}(q)E'_{01}(q) + P_{11}(q)E'_{11}(q)] \quad (7.6)$$

from which we can conclude that the force is a weighed average of the population multiplied by the derivative of the respective eigen-energy potential curve. And the effect of the leads amount to inducing particle transfer between the DQD eigenstates, and there is no charge transfer due to kinetic energy of the dots themselves.

7.2 Negative Differential Resistance - Further Derivations

The NDR phenomena in the single connection configuration (Ref. 2, table 2) can be analyzed analytically by using explicit terms of the coupling matrix elements to the tip and to the surface. Using equations 7, 8 and 14 from Ref. 2, the general coupling matrix elements to the tip reads ($\hat{f}_T = \hat{d}_1$),

$$\begin{aligned}
|\langle 00|\hat{f}_T|01\rangle|^2 &= |D_{12}|^2, |\langle 00|\hat{f}_T|10\rangle|^2 = |D_{11}|^2, \\
|\langle 11|\hat{f}_T|01\rangle|^2 &= 0, |\langle 11|\hat{f}_T|10\rangle|^2 = 0 \\
|\langle 00|\hat{f}_T^\dagger|01\rangle|^2 &= 0, |\langle 00|\hat{f}_T^\dagger|10\rangle|^2 = 0, \\
|\langle 11|\hat{f}_T^\dagger|01\rangle|^2 &= |D_{11}|^2, |\langle 11|\hat{f}_T^\dagger|10\rangle|^2 = |D_{12}|^2
\end{aligned} \tag{7.7}$$

and the general coupling matrix elements to the surface reads ($\hat{f}_S = \hat{d}_1 + \hat{d}_2$),

$$\begin{aligned}
|\langle 00|\hat{f}_S|01\rangle|^2 &= |D_{12} + D_{22}|^2, |\langle 00|\hat{f}_S|10\rangle|^2 = |D_{11} + D_{21}|^2, \\
|\langle 11|\hat{f}_S|01\rangle|^2 &= 0, |\langle 11|\hat{f}_S|10\rangle|^2 = 0 \\
|\langle 00|\hat{f}_S^\dagger|01\rangle|^2 &= 0, |\langle 00|\hat{f}_S^\dagger|10\rangle|^2 = 0, \\
|\langle 11|\hat{f}_S^\dagger|01\rangle|^2 &= |D_{11} + D_{21}|^2, |\langle 11|\hat{f}_S^\dagger|10\rangle|^2 = |D_{12} + D_{22}|^2.
\end{aligned} \tag{7.8}$$

In the symmetric case (Ref. 2, Eq. 15), the coupling matrix elements are further simplified. The matrix elements to the tip reads,

$$\begin{aligned}
|\langle 00|\hat{f}_T|01\rangle|^2 &= \frac{1}{2}(1 - s), |\langle 00|\hat{f}_T|10\rangle|^2 = \frac{1}{2}(1 + s), \\
|\langle 11|\hat{f}_T|01\rangle|^2 &= 0, |\langle 11|\hat{f}_T|10\rangle|^2 = 0 \\
|\langle 00|\hat{f}_T^\dagger|01\rangle|^2 &= 0, |\langle 00|\hat{f}_T^\dagger|10\rangle|^2 = 0, \\
|\langle 11|\hat{f}_T^\dagger|01\rangle|^2 &= \frac{1}{2}(1 + s), |\langle 11|\hat{f}_T^\dagger|10\rangle|^2 = \frac{1}{2}(1 - s)
\end{aligned} \tag{7.9}$$

and the matrix elements to the surface reads,

$$\begin{aligned}
|\langle 00|\hat{f}_S|01\rangle|^2 &= 0, |\langle 00|\hat{f}_S|10\rangle|^2 = 2(1+s), \\
|\langle 11|\hat{f}_S|01\rangle|^2 &= 0, |\langle 11|\hat{f}_S|10\rangle|^2 = 0 \\
|\langle 00|\hat{f}_S|01\rangle|^2 &= 0, |\langle 00|\hat{f}_S|10\rangle|^2 = 0, \\
|\langle 11|\hat{f}_S|01\rangle|^2 &= 2(1+s), |\langle 11|\hat{f}_S|10\rangle|^2 = 0.
\end{aligned} \tag{7.10}$$

Using these relations, we can derive analytic expressions for the steady state currents and populations for each distinctive bias potential step in the single connection configuration (Ref. 2, table 2), see Appendix C. The appendix is directed specifically to the symmetric case where the NDR is most pronounced (Ref. 2, fig. 2).

7.3 NEMS Memory Device - Additional Discussions

Apart from the degree of the inter-dot mechanical binding discussed in the NEMS TQD article in Ref. 3, there are other parameters that should be further optimized. The effect of using ligands of different compositions and lengths as well as the tunable electronic properties of the dots can lead to improved performance on one hand but also to non-functioning operation of the device on the other hand. This section is devoted to the study of those margins and constrains.

The inter-dot DQD separation for zero bias potential is denoted q_0 (q_{0AB} or q_{0BC} for the left and right sub-system respectively) and the separation can be controlled by the use of different ligands lengths. Fig. 7.2 shows the current of a DQD configuration as a function of q_0 and bias potential. The figure highlights the reading margin at $V_{RD} = [V_{R1}, V_{R2}]$ and the writing margin at $V_{WR} > V_{W0}$ for an asymmetric, $E_B > \{E_A, E_C\}$ (Fig. 7.2, top plot), and a symmetric, $E_B = E_A = E_C$ (Fig. 7.2, bottom plot) scenarios. The white parts are non-operational regions. The electronics and mechanical coupling terms (Ref. 3, Eq. 3, 4 and 11) depend on q_0 . This dependence leads to the observed shifts in the positions of the voltage steps at steady state, and in particular to sensitivity of the reading margin width.

Large q_0 's, reflecting long ligands, lead to both lower reading margins and smaller switching voltage ($V_{W0} - V_{R2}$), the former is not desirable while the latter is desirable. Short q_0 's, lead to more robust values of the reading region in the expense of higher switching

voltages. Therefore, it is not always preferable to minimize q_0 infinitely, even if technology allows, due to the accompanied growing power demands. Another side effect of large q_0 's is a minor reduction of readout capabilities due to lower peak to valley ratio in the current between the 'ON' (double dot current) and 'OFF' (single dot zero current) stable states. This reduction is more pronounced in the asymmetric case in comparison with the symmetric case.

A major difference between the top and bottom plots in Fig. 7.2 appears in the writing region. While in the symmetric case the entire range of q_0 's values is accessible for writing, in the asymmetric case, only a more limited region is accessible, which is the reason for the non-operational white writing region for large values of q_0 's. This difference, which would only grow for growing asymmetries, reflects the fact that the probability for mechanical response due to the single particle orbital is more pronounced in the symmetric case than the asymmetric cases as discussed in Ref. 1.

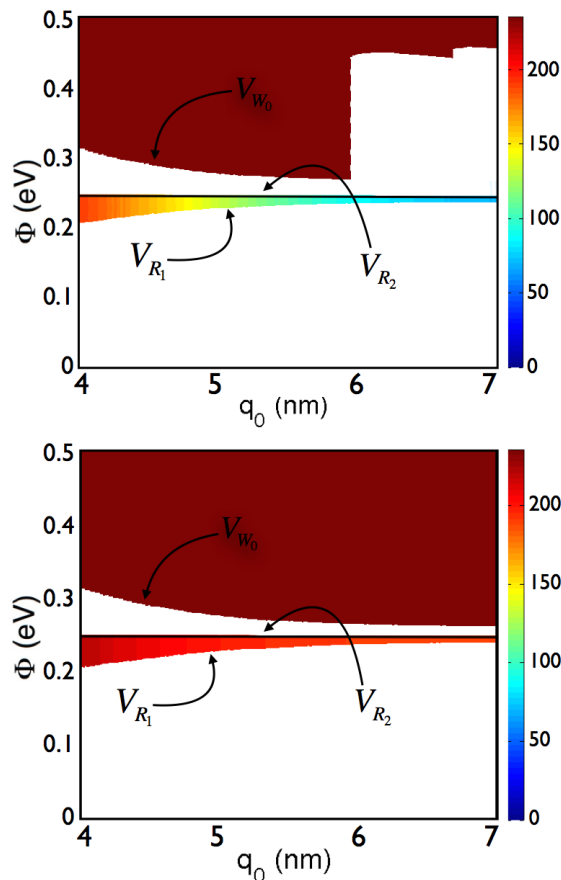


FIGURE 7.2: Current as a function of interdot distance, q_0 , and bias potentials Φ for an asymmetric (top) and symmetric (bottom) configurations. The colored regions highlight the writing and reading voltage margins for different ligands length which are reflected in q_0 . The white parts are non-operational regions.

The operation capability of the TQD NEMS device depends also on the degree of asymmetry or size differences between each BQD and the FQD. The FQD should be larger than or equal the BQDs. Deviation from this requirement would cause undesirable operation of the device. Fig. 7.3 shows the interdot distance at steady state as a function of $E_A - E_B$ for the left sub-system (the same applies for $E_C - E_B$ for the right sub-system) and bias potential for a constant q_0 . The dark red region in this plot points to an area where a switching response takes place. The dependence of the switching response on the asymmetry can be understood on the basis of the steady state populations of the different electronic states of the DQD, as discussed in Ref. 1.

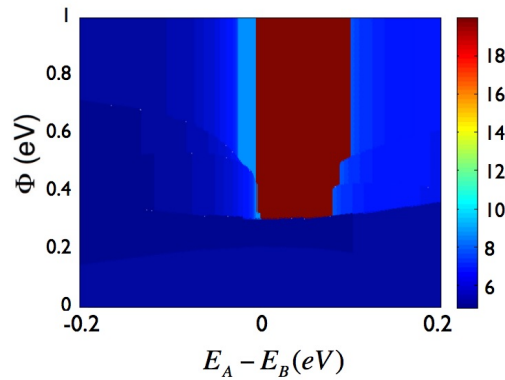


FIGURE 7.3: The interdot distance (in nm) as a function of asymmetry, $E_A - E_B$ and bias potential. The dark red region indicates switching between a DQD to a SQD configuration under the appropriate lead, for $q_0 = 5nm$.

Following the above analysis, it can be concluded that a delicate balance should be maintained in order to ensure a margin of safety between the mechanical binding strength, the degree of dots asymmetry and the ligand lengths, q_0 , in order to ensure the flawless operation of the device.

Chapter 8

Discussion

The aim of the research presented above was to improve our understanding of colloidal quantum dots (CQD) clusters. Specifically, we modeled charge transport induced phenomena in colloidal double quantum dots (DQD) and developed new probes for inter-dot interactions. We also proposed a scheme for a nano-electromechanical device in which the principle of operation is based on our previous findings. For brevity, we shall refer to the three papers presented above in Chapters 6.1, 6.2, 6.3 as Refs. 1, 2, 3, respectively.

The significance of the research is reflected in the fact that (1) the territory of mechanical coupling between CQDs has never been studied. The interaction between CQDs is controlled by their surface chemistry and by the organic ligands that link between the dots and therefore difficult to assess; (2) the extent to which single dot properties and the interactions between dots in an array are significant, in relation to observed transport properties in general and nonlinear effects in particular, is far from understood; (3) intermediate regimes of several interacting CQDs in which specific interdot interactions might be manifested in transport measurements have been hardly studied.

The research described in Ref. 1 proposed a new setup for inducing controlled mechanical motions of CQDs on a surface and for extracting information on the hard to characterize ligand-mediated effective interdot forces.

The model setup in the study was a DQD structure in an STM tip-DQD-substrate architecture (see Figure 1 in Ref. 1). The model elucidated the relation between electronic transport and mechanical motion within the DQD for parameters chosen in consistency with typical dimensions of CQDs structures. Typical values of quantum dot masses

and the chosen ligand-mediated interdot binding force constants allowed us to treat the motion classically.

The electro-mechanical coupling was accounted for by considering explicitly the dependence of the electronic terms on the interdot distance. In particular, the single electron (tunneling) coupling and the many body (Coulomb and exchange) interaction terms were calculated self-consistently with the interdot mechanical response within a mixed quantum-classical reduced density matrix formulation.

The DQD-leads (STM contacts) coupling was assumed to be weak based on typical values of tunneling barriers in STM setups. The leads were assumed to maintain a quasi-equilibrium density, while the many-body DQD system was evolved according to the reduced Liouville equation to second order in the coupling to the leads.

The steady-state response of the system to applied bias voltage between the tip and the substrate was found by using a self-consistent solution of the coupled electro-mechanical dynamical equations under the constraint of zero velocity and acceleration at steady state.

The motion was simultaneously, induced and evaluated, by applying a bias voltage and measuring the current through the STM setup. The correlation between the measured current and the mechanical motion was then demonstrated. The mechanical binding potential (Figure 2 in Ref. 1) was modeled using a generic Morse potential with parameters that controlled transitions from “weak” to “strong” binding. This potential was used to reflect the short-range repulsion and long-term attraction forces of the ligand-mediated force between the dots.

The calculations showed that charge transport can induce mechanical recoil and/or dissociation - transition from a DQD to a SQD. For strong interdot binding interaction (Figure 3 in Ref. 1), changes in interdot distances were minor for any bias. However, for weak binding, changes in interdot distances were significant, reflecting apparent mechanical response. The mechanical response was accompanied by apparent variations also in the current.

Another important characteristic was the dependency on the DQD symmetry. The difference between the dots is reflected in different LUMO energies, that is, $E_A \neq E_B$, which can be obtained by using CQDs with different sizes and compositions. Strong

mechanical response (dissociation) was observed for weak binding when the tip was coupled to the smaller dot or for symmetric dots (Figure 5 in Ref. 1). When the tip was coupled to the larger dot, the mechanical response was insignificant.

Finally, a Born-Oppenheimer interpretation of the steady-state response was formulated. The average electro-mechanical force was attributed to potential energy curves associated with the eigenstates of the DQD. The effective force was weighted according to the steady-state populations of each eigenstate (Figure 4 in Ref. 1). For strong binding, all the curves were attractive. For intermediate binding the highest curve became repulsive and for weak binding the two highest curves became repulsive. Mechanical response became apparent when the averaged force over all the curves multiplied by the population at each curve became repulsive. This was due to significant population transfer into the repulsive states. The two most significant contributions to the repulsion were the single electron eigenstate associated with an anti-bonding orbital and the two-body repulsion orbital.

In the work in Ref. 2 we extended our study to nonlinear effects in transport through arrays of CQDs, where the STM setup, with a strong mechanical binding potential between the dots, was shown to give rise to a non-linear NDR effect. It was found out that destructive interference between different pathways at the DQD-surface interface can give rise to an unexplored dark state. In particular, destructive interference through the antibonding orbital resulted in charging of a dark state that blocked the current through the DQD via Coulomb repulsion, and resulted in the appreciable NDR and a corresponding distinctive signal in the current-voltage curve.

Our theoretical analysis showed that an accurate probe measurement of the interdot interaction can be based on the measurement of this NDR signal. It can also provide meaningful information on the intricate electronic interaction between two neighboring dots in the DQD, and potentially be used to reveal the molecule like nature of the DQD.

Our task in Ref. 2 was two-fold. First, we wished to check the transport through different DQD configurations (see Table 1 in Ref. 2). In the absence of interactions between the dots in the DQD, the I-V curve reflected the behavior of a single transport channel with a single threshold energy. In the presence of interdot interactions, there was a shift of the threshold energy in all the different DQD configurations. The shift was found out to be indicative of the interdot coupling strength. The appearance of a

pronounced NDR effect appeared only in the case of the STM configuration described above. The NDR effect was absent in the case of parallel configuration (see Table 1, Row 3 in Ref. 2), where the tip was coupled to both dots.

Second, we studied the energetically allowed transition rates and the underlying coupling matrix elements in the two most interesting configurations (Table 2, Row 3 and 4 in Ref. 2), with which we could derive analytic expressions that clarified the NDR phenomena. It was found out that the antibonding state was trapped in a "dark state" with respect to the coupling to the surface, and was not contributing to the current. This was due to the unique connectivity in the STM configuration in which charging and discharging rates of the antibonding state were dramatically different. At the NDR voltage margin, other states could not be occupied because an additional finite charging energy was needed and so they remained empty and there was no contribution to the current, hence it dropped to zero. It was found that for higher voltages, the current builds up again.

The width of the NDR was found to depend on the distance between the dots due to the dependency on the electronic coupling terms, which in turn are controlled by the capping ligands. We suggested that the sensitivity of the NDR signal to the interdot distance strongly indicate that this particular NDR originates from our proposed unique dark state mechanism, because no other known NDR mechanism in the literature predicts such distance dependence.

Lastly, dependency on asymmetry of the two dots was studied. The NDR was found to be less pronounced for all asymmetries, where only a small drop in the current was observed when the tip was placed above the larger dot, and the NDR was completely missing when the tip was placed above the smaller dot (Figure 2 in Ref. 2). However, it was shown that NDR can still be pronounced for weakly asymmetric DQD structures for short interdot distances (Figure 3 in Ref. 2).

Additional perspective on the DQD characteristics was presented using a non-standard RC (resistor-capacitor) scheme. An orthodox classical kinetic RC schemes, where the two dots are modeled as separate entities connected by incoherent transition rates, couldn't be used in our model because of significant coherence relation between the dots. Therefore, in our model, each of the single-electron orbitals, and not each dot, was affixed with different RC parameters (Figure 4 in Ref. 1 and Figure 6 in Ref. 2). Each one of the DQD orbitals had different effective resistance and capacitance at the coupling

to the tip and to the surface which depended on the dot asymmetries and the different orbitals (bonding/antibonding).

The final waypoint of this research was the characterization of a novel nano-electromechanical memory device. The device, incorporating a triple CQDs structure (Figure 1 in Ref. 3), was based on the dissociation effect as presented in Ref. 1 and the NDR effect as presented in Ref. 2. The device was compared to conventional FLASH devices as well as to other state of the art nano-electromechanical memory devices, and it was elaborated that unlike other devices, the conventional classical electrostatic and mechanical modeling was not sufficient in this case.

The device consisted of 2 bound quantum dots placed at the two edges of the device and 1 floating quantum dot that was placed between them and can transit between each bound dot to the other. The device was divided into two isolated sub-systems under the assumption of zero interaction between the bound dots. Each sub-system consisted of 1 bound dot and, depending on the state of the device, an additional floating dot.

The bias potential margins of the write and read commands of the device were presented in Figure 2 in Ref. 3. The write command controlled the switching between the left and right sub-system configurations and the read command probed the current of the left configuration and depended on the specific state of the device. In particular, measurement of the current before a mechanical floating implied charge transport through two dots (bound and floating dots) and high current probing, corresponding to an 'ON' state, while measurement of the current after a mechanical response implied charge transport through a single bound dot and zero current, corresponding to an 'OFF' state.

The most crucial consideration for the proper operation of the device was shown to be the degree of the interdot mechanical binding strength (Figure 2 in Ref. 3). Similarly to Ref. 2, a strong mechanical binding potential led to a current drop, which served as indication for non-proper operation of the device. Further operation and optimization considerations are presented in section 7.3

Several key advantages of the CQDs NEMS device were pointed out. Ordinary mechanical bistability and the accompanied $I - V$ hysteresis was shown to be non-existent in this device, implying zero trade-off between the conventional motivation to reduce the switching voltage and controlling the ON/OFF currents ratio. Also, the 'ON' or 'OFF'

states were shown to be not affected by charging effects, implying the possibility of zero current leakage. Lastly, the write operation frequency was estimated based on an inter-dot oscillation frequency and the resultant frequency was estimated to be higher than that of current non-volatile FLASH memory devices.

Appendix A

Hamiltonian of a Double Quantum Dot with spin

We start by writing the general Hamiltonian in the case of two (real) spatial orbitals (including Spin), $i, j, k, l \in \{1\alpha, 1\beta, 2\alpha, 2\beta\}$, $\{\varphi_1, \varphi_2\} \in R$ which reduces from the full Hamiltonian (eq. 4.15 in the text) to:

$$\begin{aligned}
H_M = & \varepsilon_1 a_{1\alpha}^\dagger a_{1\alpha} + \varepsilon_1 a_{1\beta}^\dagger a_{1\beta} + \varepsilon_2 a_{2\alpha}^\dagger a_{2\alpha} + \varepsilon_2 a_{2\beta}^\dagger a_{2\beta} + t a_{1\alpha}^\dagger a_{2\alpha} + t a_{1\beta}^\dagger a_{2\beta} + t a_{2\alpha}^\dagger a_{1\alpha} \\
& + t a_{2\beta}^\dagger a_{1\beta} + U_{11} a_{1\alpha}^\dagger a_{1\alpha} a_{1\beta}^\dagger a_{1\beta} + U_{22} a_{2\alpha}^\dagger a_{2\alpha} a_{1\beta}^\dagger a_{1\beta} + (U_{12} \\
& - U_{ex}) [a_{1\alpha}^\dagger a_{1\alpha} a_{2\alpha}^\dagger a_{2\alpha} + a_{1\beta}^\dagger a_{1\beta} a_{2\beta}^\dagger a_{2\beta}] + U_{12} [a_{1\alpha}^\dagger a_{1\alpha} a_{2\beta}^\dagger a_{2\beta} \\
& + a_{2\alpha}^\dagger a_{2\alpha} a_{1\beta}^\dagger a_{1\beta}] + S_1 [a_{1\alpha}^\dagger a_{1\alpha} a_{1\beta}^\dagger a_{2\beta} + a_{1\alpha}^\dagger a_{1\alpha} a_{2\beta}^\dagger a_{1\beta} + a_{1\beta}^\dagger a_{1\beta} a_{1\alpha}^\dagger a_{2\alpha} \\
& + a_{1\beta}^\dagger a_{1\beta} a_{2\alpha}^\dagger a_{1\alpha}] + S_2 [a_{2\alpha}^\dagger a_{2\alpha} a_{1\beta}^\dagger a_{2\beta} + a_{2\alpha}^\dagger a_{2\alpha} a_{2\beta}^\dagger a_{1\beta} + a_{2\beta}^\dagger a_{2\beta} a_{1\alpha}^\dagger a_{2\alpha} \\
& + a_{2\beta}^\dagger a_{2\beta} a_{2\alpha}^\dagger a_{1\alpha}] + U_{ex} [a_{1\alpha}^\dagger a_{2\alpha} a_{1\beta}^\dagger a_{2\beta} + a_{1\alpha}^\dagger a_{2\alpha} a_{2\beta}^\dagger a_{1\beta} + a_{2\alpha}^\dagger a_{2\alpha} a_{1\beta}^\dagger a_{2\beta} \\
& + a_{2\alpha}^\dagger a_{1\alpha} a_{2\beta}^\dagger a_{1\beta}]
\end{aligned} \tag{A1}$$

where the single particle energies are,

$$\begin{aligned}
\varepsilon_i &= \langle i | \hat{h} | i \rangle = \int dr \varphi_i^*(r) \left[\frac{-\hbar^2}{2m_e} \nabla_r^2 + V(r) \right] \varphi_i(r) \\
\varepsilon_1 &= \int dr \varphi_1^*(r) \left[\frac{-\hbar^2}{2m_e} \nabla_r^2 + V(r) \right] \varphi_1(r), \\
\varepsilon_2 &= \int dr \varphi_2^*(r) \left[\frac{-\hbar^2}{2m_e} \nabla_r^2 + V(r) \right] \varphi_2(r) \\
t &= \int dr \varphi_2^*(r) \left[\frac{-\hbar^2}{2m_e} \nabla_r^2 + V(r) \right] \varphi_1(r)
\end{aligned} \tag{A2}$$

and the two-particle interaction energies terms are,

$$\begin{aligned}
U_{11} &= \langle 1,1 | 1,1 \rangle = \int dr_1 \int dr_2 \varphi_1^*(r_1) \varphi_1^*(r_2) \frac{K e^2}{|r_1 - r_2|} \varphi_1(r_1) \varphi_1(r_2) \\
U_{22} &= \langle 2,2 | 2,2 \rangle = \int dr_1 \int dr_2 \varphi_2^*(r_1) \varphi_2^*(r_2) \frac{K e^2}{|r_1 - r_2|} \varphi_2(r_1) \varphi_2(r_2) \\
U_{12} &= \langle 1,2 | 1,2 \rangle = \int dr_1 \int dr_2 \varphi_1^*(r_1) \varphi_2^*(r_2) \frac{K e^2}{|r_1 - r_2|} \varphi_1(r_1) \varphi_2(r_2) \\
U_{ex} &= \langle 1,2 | 2,1 \rangle = \int dr_1 \int dr_2 \varphi_1^*(r_1) \varphi_2^*(r_2) \frac{K e^2}{|r_1 - r_2|} \varphi_2(r_1) \varphi_1(r_2) \\
S_1 &= \langle 1,1 | 1,2 \rangle = \int dr_1 \int dr_2 \varphi_1^*(r_1) \varphi_1^*(r_2) \frac{K e^2}{|r_1 - r_2|} \varphi_1(r_1) \varphi_2(r_2) \\
S_2 &= \langle 2,2 | 2,1 \rangle = \int dr_1 \int dr_2 \varphi_2^*(r_1) \varphi_2^*(r_2) \frac{K e^2}{|r_1 - r_2|} \varphi_2(r_1) \varphi_1(r_2).
\end{aligned} \tag{A3}$$

* As presented in the text (eq. 5.10), only the terms, U_{12} and U_{ex} , are relevant for a single spin model.

Deducing the above two (real) spatial orbitals Hamiltonian (with Spin) is based on the application of the following two restrictions:

1. No spin transitions: $\begin{cases} spin(i) = spin(k) \\ spin(j) = spin(l) \end{cases}$
2. Only one Fermion per single spin-orbital state $\begin{cases} i \neq j \\ l \neq k \end{cases}$

Using those restrictions, we present a detailed derivation of the allowed two-particle interaction terms of the system Hamiltonian (Eq. A1).

The presentation of the allowed terms, presented below, follow a specific pattern. The first and second terms ($\hat{a}_i^\dagger, \hat{a}_j^\dagger$) are all the possible (second restriction - only one fermion can be created in each spin-orbital state) creation operators combination. In analog, the third and fourth terms (\hat{a}_l, \hat{a}_k) are all the possible (second restriction again) destruction operators combinations. Additionally, the relation between the first two terms and the last two terms follow the first restriction which state the prohibition on spin transitions.

Therefore, the general interaction term, $\hat{a}_i^\dagger \hat{a}_j^\dagger \hat{a}_l \hat{a}_k$ (Eq. 4.15), is presented as follows:

$$\hat{a}_i^\dagger \hat{a}_j^\dagger \left\{ \begin{array}{l} \hat{a}_{l1} \left\{ \begin{array}{l} \hat{a}_{k1} \\ \hat{a}_{k2} \end{array} \right. \\ \hat{a}_{l2} \left\{ \begin{array}{l} \hat{a}_{k1} \\ \hat{a}_{k2} \end{array} \right. \end{array} \right.$$

where $\hat{a}_{l1}, \hat{a}_{l2}, \hat{a}_{k1}, \hat{a}_{k2}$ are the different allowed terms. The terms in brackets are the corresponding coefficients of each interaction term, $\langle i, j | k, l \rangle$.

After rearrangement of the terms, we get,

$$\begin{aligned}
& \hat{a}_{1\alpha}^+ \hat{a}_{1\alpha} \hat{a}_{1\beta}^+ \hat{a}_{1\beta} [\langle 1,1,1,1 \rangle + \langle 1,1,1,1 \rangle] \\
& \hat{a}_{2\alpha}^+ \hat{a}_{2\alpha} \hat{a}_{2\beta}^+ \hat{a}_{2\beta} [\langle 2,2,2,2 \rangle + \langle 2,2,2,2 \rangle] \\
& \hat{a}_{1\alpha}^+ \hat{a}_{1\alpha} \hat{a}_{2\alpha}^+ \hat{a}_{2\alpha} [\langle 2,1,2,1 \rangle - \langle 2,1,1,2 \rangle - \langle 1,2,2,1 \rangle + \langle 1,2,1,2 \rangle] \\
& \hat{a}_{1\beta}^+ \hat{a}_{1\beta} \hat{a}_{2\beta}^+ \hat{a}_{2\beta} [\langle 2,1,2,1 \rangle - \langle 2,1,1,2 \rangle - \langle 1,2,2,1 \rangle + \langle 1,2,1,2 \rangle] \\
& \hat{a}_{1\alpha}^+ \hat{a}_{1\alpha} \hat{a}_{2\beta}^+ \hat{a}_{2\beta} [\langle 2,1,2,1 \rangle + \langle 1,2,1,2 \rangle] \\
& \hat{a}_{2\alpha}^+ \hat{a}_{2\alpha} \hat{a}_{1\beta}^+ \hat{a}_{1\beta} [\langle 2,1,2,1 \rangle + \langle 1,2,1,2 \rangle] \\
& \hat{a}_{1\alpha}^+ \hat{a}_{1\alpha} \hat{a}_{1\beta}^+ \hat{a}_{2\beta} [\langle 1,1,1,2 \rangle + \langle 1,1,2,1 \rangle] \\
& \hat{a}_{1\alpha}^+ \hat{a}_{1\alpha} \hat{a}_{1\beta} \hat{a}_{2\beta}^+ [-\langle 2,1,1,1 \rangle - \langle 1,2,1,1 \rangle] \\
& \hat{a}_{2\alpha}^+ \hat{a}_{2\alpha} \hat{a}_{1\beta}^+ \hat{a}_{2\beta} [\langle 2,1,2,2 \rangle + \langle 1,1,2,2 \rangle] \\
& \hat{a}_{2\alpha}^+ \hat{a}_{2\alpha} \hat{a}_{1\beta} \hat{a}_{2\beta}^+ [-\langle 2,2,2,1 \rangle - \langle 2,2,1,2 \rangle] \\
& \hat{a}_{1\alpha}^+ \hat{a}_{2\alpha} \hat{a}_{1\beta}^+ \hat{a}_{1\beta} [\langle 1,1,2,1 \rangle + \langle 1,1,1,2 \rangle] \\
& \hat{a}_{1\alpha} \hat{a}_{2\alpha}^+ \hat{a}_{1\beta} \hat{a}_{1\beta}^+ [-\langle 2,1,1,1 \rangle - \langle 1,2,1,1 \rangle] \\
& \hat{a}_{1\alpha}^+ \hat{a}_{2\alpha} \hat{a}_{2\beta}^+ \hat{a}_{2\beta} [\langle 2,1,2,2 \rangle + \langle 1,2,2,2 \rangle] \\
& \hat{a}_{1\alpha} \hat{a}_{2\alpha}^+ \hat{a}_{2\beta} \hat{a}_{2\beta}^+ [-\langle 2,2,1,2 \rangle - \langle 2,2,2,1 \rangle] \\
& \hat{a}_{1\alpha}^+ \hat{a}_{2\alpha} \hat{a}_{1\beta}^+ \hat{a}_{2\beta} [\langle 1,1,2,2 \rangle + \langle 1,1,2,2 \rangle] \\
& \hat{a}_{1\alpha}^+ \hat{a}_{2\alpha} \hat{a}_{1\beta} \hat{a}_{2\beta}^+ [-\langle 2,1,1,2 \rangle - \langle 1,2,2,1 \rangle] \\
& \hat{a}_{1\alpha} \hat{a}_{2\alpha}^+ \hat{a}_{1\beta} \hat{a}_{2\beta} [-\langle 2,1,1,2 \rangle - \langle 1,2,2,1 \rangle] \\
& \hat{a}_{1\alpha} \hat{a}_{2\alpha}^+ \hat{a}_{1\beta} \hat{a}_{2\beta}^+ [\langle 2,2,1,1 \rangle + \langle 2,2,1,1 \rangle]
\end{aligned} \tag{A8}$$

And by associating the following abbreviations to each to the different terms, we finally derive the general Hamiltonian including Spin (eq. A1),

$$\begin{aligned}
& (i, j, k, l) = (j, i, l, k) \\
& (i, j, k, l) = (k, l, i, j)^* \\
& \Rightarrow \\
& U_{11} = (1,1,1,1) \\
& U_{22} = (2,2,2,2) \\
& U_{12} = (1,2,1,2) = (2,1,2,1) \\
& U_{ex} = (1,2,2,1) = (2,1,1,2) = (2,2,1,1) \\
& S_1 = (1,1,1,2) = (1,2,1,1) \\
& S_2 = (2,2,2,1) = (2,1,2,2)
\end{aligned} \tag{A9}$$

Appendix B

Hamiltonian Interactions

We start the derivation of the Coulomb interaction terms by rewriting Eq. 5.10 from the main text in the following way,

$$\varphi_i(r) = \frac{a_i}{\sqrt{a_i^2 + b_i^2 + 2Sa_i b_i}} \chi_a(r) + \frac{b_i}{\sqrt{a_i^2 + b_i^2 + 2Sa_i b_i}} \chi_b(r); i = 1,2. \quad (\text{B1})$$

Using $\varphi_i(r)$ we can derive the following useful expression

$$\begin{aligned} & \frac{\varphi_i(r_{1,2})\varphi_k(r_{1,2})}{=} = \frac{a_i a_k \chi_a(r_{1,2})\chi_a(r_{1,2}) + b_i b_k \chi_b(r_{1,2})\chi_b(r_{1,2}) + (a_i b_k + b_i a_k) \chi_a(r_{1,2})\chi_b(r_{1,2})}{\sqrt{a_i^2 + b_i^2 + 2Sa_i b_i} \sqrt{a_k^2 + b_k^2 + 2Sa_k b_k}} \\ \varphi_i(r_1)\varphi_k(r_1) &= \frac{a_i a_k \chi_a(r_1)\chi_a(r_1) + b_i b_k \chi_b(r_1)\chi_b(r_1) + (a_i b_k + b_i a_k) \chi_a(r_1)\chi_b(r_1)}{\sqrt{a_i^2 + b_i^2 + 2Sa_i b_i} \sqrt{a_k^2 + b_k^2 + 2Sa_k b_k}} \\ \varphi_j(r_2)\varphi_l(r_2) &= \frac{a_j a_l \chi_a(r_2)\chi_a(r_2) + b_j b_l \chi_b(r_2)\chi_b(r_2) + (a_j b_l + b_j a_l) \chi_a(r_2)\chi_b(r_2)}{\sqrt{a_j^2 + b_j^2 + 2Sa_j b_j} \sqrt{a_l^2 + b_l^2 + 2Sa_l b_l}} \end{aligned} \quad (\text{B2})$$

where the Gaussian ($\chi_{a,b}(r)$) product terms are,

$$\begin{aligned} \chi_a(r)\chi_a(r) &= \left(\frac{\alpha}{\pi}\right)^{3/2} e^{-\alpha(r-R_a)^2} \equiv \chi_{aa}(r) \\ \chi_b(r)\chi_b(r) &= \left(\frac{\alpha}{\pi}\right)^{3/2} e^{-\alpha(r-R_b)^2} \equiv \chi_{bb}(r) \\ \chi_a(r)\chi_b(r) &= \left(\frac{\alpha}{\pi}\right)^{3/2} e^{-\frac{\alpha}{4}(R_a-R_b)^2} e^{-\frac{\alpha}{4}(r-[R_a+R_b]/2)^2} = e^{-\frac{\alpha}{4}(R_a-R_b)^2} \chi_{ab}(r) \end{aligned} \quad (\text{B3})$$

Using these relations, we can write explicit expression for the Coulomb integral,

$$\begin{aligned}
\langle ij|kl \rangle &= \int dr_1 \int dr_2 \varphi_i(r_1) \varphi_k(r_1) \frac{Ke^2}{|r_1 - r_2|} \varphi_j(r_2) \varphi_l(r_2) \\
&= \frac{1}{\sqrt{a_i^2 + b_i^2 + 2Sa_i b_i} \sqrt{a_k^2 + b_k^2 + 2Sa_k b_k} \sqrt{a_j^2 + b_j^2 + 2Sa_j b_j} \sqrt{a_l^2 + b_l^2 + 2Sa_l b_l}} \\
&\cdot [a_i a_k a_j a_l \int dr_1 \int dr_2 \chi_{aa}(r_1) \frac{Ke^2}{|r_1 - r_2|} \chi_{aa}(r_2) \\
&+ a_i a_k a_j a_l \int dr_1 \int dr_2 \chi_{aa}(r_1) \frac{Ke^2}{|r_1 - r_2|} \chi_{bb}(r_2) \\
&+ a_i a_k (a_j b_l + b_j a_l) e^{-\frac{\alpha}{4}(R_a - R_b)^2} \int dr_1 \int dr_2 \chi_{aa}(r_1) \frac{Ke^2}{|r_1 - r_2|} \chi_{ab}(r_2) \\
&+ b_i b_k a_j a_l \int dr_1 \int dr_2 \chi_{bb}(r_1) \frac{Ke^2}{|r_1 - r_2|} \chi_{aa}(r_2) \\
&+ b_i b_k b_j b_l \int dr_1 \int dr_2 \chi_{bb}(r_1) \frac{Ke^2}{|r_1 - r_2|} \chi_{bb}(r_2) \\
&+ b_i b_k (a_j b_l + b_j a_l) e^{-\frac{\alpha}{4}(R_a - R_b)^2} \int dr_1 \int dr_2 \chi_{bb}(r_1) \frac{Ke^2}{|r_1 - r_2|} \chi_{ab}(r_2) \\
&+ (a_i b_k + b_i a_k) a_j a_l e^{-\frac{\alpha}{4}(R_a - R_b)^2} \int dr_1 \int dr_2 \chi_{ab}(r_1) \frac{Ke^2}{|r_1 - r_2|} \chi_{aa}(r_2) \\
&+ (a_i b_k + b_i a_k) b_j b_l e^{-\frac{\alpha}{4}(R_a - R_b)^2} \int dr_1 \int dr_2 \chi_{ab}(r_1) \frac{Ke^2}{|r_1 - r_2|} \chi_{bb}(r_2) \\
&+ (a_i b_k + b_i a_k) (a_j b_l + b_j a_l) e^{-\frac{\alpha}{4}(R_a - R_b)^2} \int dr_1 \int dr_2 \chi_{ab}(r_1) \frac{Ke^2}{|r_1 - r_2|} \chi_{ab}(r_2)].
\end{aligned} \tag{B4}$$

Using the identity:

$$\int dr_1 \int dr_2 \left(\frac{p}{\pi}\right)^{3/2} e^{-p(r_1 - R_p)^2} \left(\frac{q}{\pi}\right)^{3/2} e^{-q(r_1 - R_q)^2} \frac{1}{|r_1 - r_2|} = \frac{\text{erf}\left[\sqrt{\frac{pq}{p+q}} |R_p - R_q|\right]}{|R_p - R_q|} \tag{B5}$$

$$\text{erf}[x] = \frac{2}{\sqrt{\pi}} \int_0^x e^{-t^2} dt \tag{B6}$$

the Gaussian integrals are written as

$$\begin{aligned}
\int dr_1 \int dr_2 \frac{\chi_{aa}(r_1) \chi_{aa}(r_2)}{|r_1 - r_2|} &= \int dr_1 \int dr_2 \frac{\chi_{bb}(r_1) \chi_{bb}(r_2)}{|r_1 - r_2|} = \int dr_1 \int dr_2 \frac{\chi_{ab}(r_1) \chi_{ab}(r_2)}{|r_1 - r_2|} \\
&= \sqrt{\frac{2\alpha}{\pi}}
\end{aligned}$$

$$\int dr_1 \int dr_2 \frac{\chi_{aa}(r_1)\chi_{bb}(r_2)}{|r_1 - r_2|} = \frac{\text{erf}\left[\sqrt{\frac{\alpha}{2}}|R_a - R_b|\right]}{|R_a - R_b|}$$

$$\int dr_1 \int dr_2 \frac{\chi_{aa}(r_1)\chi_{ab}(r_2)}{|r_1 - r_2|} = \int dr_1 \int dr_2 \frac{\chi_{bb}(r_1)\chi_{ab}(r_2)}{|r_1 - r_2|} = \frac{\text{erf}\left[\sqrt{\frac{\alpha}{2}}|R_a - R_b|/2\right]}{|(R_a - R_b)/2|}.$$

(B7)

Denoting the inter dot distance as $q = |R_a - R_b|$, we finally obtain a close expression for the interactions.

$$\begin{aligned} \langle ij|kl \rangle &= \int dr_1 \int dr_2 \varphi_i(r_1)\varphi_k(r_1) \frac{Ke^2}{|r_1 - r_2|} \varphi_j(r_2)\varphi_l(r_2) \\ &= \frac{Ke^2}{Ke^2} \\ &= \frac{\sqrt{a_i^2 + b_i^2 + 2Sa_i b_i} \sqrt{a_k^2 + b_k^2 + 2Sa_k b_k} \sqrt{a_j^2 + b_j^2 + 2Sa_j b_j} \sqrt{a_l^2 + b_l^2 + 2Sa_l b_l}}{\sqrt{a_i^2 + b_i^2 + 2Sa_i b_i} \sqrt{a_k^2 + b_k^2 + 2Sa_k b_k} \sqrt{a_j^2 + b_j^2 + 2Sa_j b_j} \sqrt{a_l^2 + b_l^2 + 2Sa_l b_l}} \\ &\cdot [a_i a_k a_j a_l \sqrt{\frac{2\alpha}{\pi}} + a_i a_k b_j b_l \frac{\text{erf}\left[\sqrt{\frac{\alpha}{2}}q\right]}{q} + a_i a_k (a_j b_l + b_j a_l) e^{-\frac{\alpha}{4}q^2} \frac{\text{erf}\left[\sqrt{\frac{\alpha}{2}}q/2\right]}{|q/2|} \\ &+ b_i b_k a_j a_l \frac{\text{erf}\left[\sqrt{\frac{\alpha}{2}}q\right]}{q} + b_i b_k b_j b_l \sqrt{2\alpha/\pi} + b_i b_k (a_j b_l + b_j a_l) e^{-\frac{\alpha}{4}q^2} \frac{\text{erf}\left[\sqrt{\frac{\alpha}{2}}q/2\right]}{|q/2|} \\ &+ (a_i b_k + b_i a_k) a_j a_l e^{-\frac{\alpha}{4}q^2} \frac{\text{erf}\left[\sqrt{\frac{\alpha}{2}}q/2\right]}{|q/2|} + (a_i b_k + b_i a_k) b_j b_l e^{-\frac{\alpha}{4}q^2} \frac{\text{erf}\left[\sqrt{\frac{\alpha}{2}}q/2\right]}{|q/2|} \\ &+ (a_i b_k + b_i a_k) (a_j b_l + b_j a_l) e^{-\frac{\alpha}{2}q^2} \sqrt{2\alpha/\pi}] \end{aligned}$$

(B8)

$$\begin{aligned}
\langle ij|kl\rangle &= \int dr_1 \int dr_2 \varphi_i(r_1)\varphi_k(r_1) \frac{Ke^2}{|r_1 - r_2|} \varphi_j(r_2)\varphi_l(r_2) \\
&= \frac{Ke^2}{\sqrt{a_i^2 + b_i^2 + 2Sa_i b_i} \sqrt{a_k^2 + b_k^2 + 2Sa_k b_k} \sqrt{a_j^2 + b_j^2 + 2Sa_j b_j} \sqrt{a_l^2 + b_l^2 + 2Sa_l b_l}} \\
&\cdot \left[(a_i a_k a_j a_l + b_i b_k b_j b_l + (a_i b_k + b_i a_k)(a_j b_l + b_j a_l) e^{-\frac{\alpha}{4}q^2} \right) \sqrt{\frac{2\alpha}{\pi}} \\
&+ (a_i a_k b_j b_l + b_i b_k a_j a_l) \frac{\operatorname{erf}\left[\sqrt{\frac{\alpha}{2}}q\right]}{R} \\
&+ (a_i a_k (a_j b_l + b_j a_l) + b_i b_k (a_j b_l + b_j a_l) + (a_i b_k + b_i a_k) a_j a_l \\
&+ (a_i b_k + b_i a_k) b_j b_l) e^{-\frac{\alpha}{4}q^2} \frac{\operatorname{erf}\left[\sqrt{\frac{\alpha}{2}}q/2\right]}{|q/2|}]
\end{aligned} \tag{B9}$$

Using the above derivation, we can write explicit expressions for the two-particle interaction terms and explicitly for the Coloumb and exchange interaction terms that remain in the case of a single spin Hamiltonian (Eq. 5.1 in the text).

Here are three representative terms:

$$\begin{aligned}
U_{11} &= \langle 1,1||1,1\rangle = \frac{Ke^2}{(a_1^2 + b_1^2 + 2Sa_1 b_1)^2} \\
&\cdot \left[\sqrt{\frac{2\alpha}{\pi}} (a_1^4 + b_1^4 + 4a_1^2 b_1^2 e^{-\frac{\alpha}{2}R^2}) + \frac{\operatorname{erf}[\sqrt{\alpha/2}R]}{R} 2a_1^2 b_1^2 + e^{-\frac{\alpha}{4}R^2} \frac{\operatorname{erf}[\sqrt{\alpha/2}R/2]}{R/2} [4a_1^3 b_1 + 4b_1^3 a_1] \right. \\
U_{22} &= \langle 2,2||2,2\rangle = \frac{Ke^2}{(a_2^2 + b_2^2 + 2Sa_2 b_2)^2} \\
&\cdot \left[\sqrt{\frac{2\alpha}{\pi}} (a_2^4 + b_2^4 + 4a_2^2 b_2^2 e^{-\frac{\alpha}{2}R^2}) + \frac{\operatorname{erf}[\sqrt{\alpha/2}R]}{R} 2a_2^2 b_2^2 + e^{-\frac{\alpha}{4}R^2} \frac{\operatorname{erf}[\sqrt{\alpha/2}R/2]}{R/2} [4a_2^3 b_2 + 4b_2^3 a_2] \right. \\
U_{12} &= \langle 1,2||1,2\rangle = \frac{Ke^2}{(a_1^2 + b_1^2 + 2Sa_1 b_1)(a_2^2 + b_2^2 + 2Sa_2 b_2)} \\
&\cdot \left[\sqrt{\frac{2\alpha}{\pi}} (a_1^2 a_2^2 + b_1^2 b_2^2 + 4a_1 a_2 b_1 b_2 e^{-\frac{\alpha}{2}R^2}) + \frac{\operatorname{erf}[\sqrt{\alpha/2}R]}{R} (a_1^2 b_2^2 + b_1^2 a_2^2) \right. \\
&+ e^{-\frac{\alpha}{4}R^2} \frac{\operatorname{erf}[\sqrt{\alpha/2}R/2]}{R/2} [a_1^2 (a_2 b_2 + b_2 a_2) + b_1^2 (a_2 b_2 + b_2 a_2) + a_2^2 (a_1 b_1 + b_1 a_1) + b_2^2 (a_1 b_1 + b_1 a_1)]
\end{aligned} \tag{B10}$$

Appendix C

Negative Differential Resistance

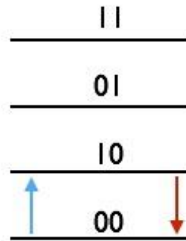
We derive analytic expressions for the probabilities and currents in the single connection scheme for the different bias potentials margins which appear in table 2, article 6.2. We further concentrate on the symmetric case in each one of those margins.

For simplicity, in the symmetric case, we work in the regime of small overlap between the localized orbitals, $s \ll 1$. Extension to the general case is straightforward.

Pay attention that $D_{11}, D_{12}, D_{21}, D_{22}$ in the text (Eq. 15 in 6.2) are represented here correspondingly as $c_{11}, c_{12}, c_{21}, c_{22}$.

The schemes in each one of the cases illustrate the allowed transition rates. A continuous line indicates a finite rate for both asymmetric and symmetric cases, whereas a dashed line indicates finite rate for an asymmetric case and zero rate for a symmetric case.

1. First column: $\varepsilon_2 > \Phi > \varepsilon_1$



The only non-zero transition rates (at zero T) are:

$$k_{00 \rightarrow 10}^T = |c_{11}|^2$$

$$k_{10 \rightarrow 00}^S = (c_{11} + c_{21})^2$$

Rates and Probability equations:

$$\frac{dP_{00}}{dt} = k_{10 \rightarrow 00}^S P_{10} - k_{00 \rightarrow 10}^T P_{00} = 0$$

$$P_{00} + P_{10} = 1$$

$$(c_{11} + c_{21})^2 P_{10} - c_{11}^2 (1 - P_{10}) = 0$$

$$[(c_{11} + c_{21})^2 + c_{11}^2] P_{10} = c_{11}^2$$

$$P_{10} = \frac{c_{11}^2}{(c_{11} + c_{21})^2 + c_{11}^2} \quad ; \quad P_{00} = \frac{(c_{11} + c_{21})^2}{(c_{11} + c_{21})^2 + c_{11}^2}$$

$$I = \frac{(c_{11} + c_{21})^2 c_{11}^2}{(c_{11} + c_{21})^2 + c_{11}^2}$$

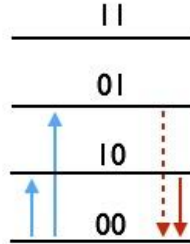
In the symmetric case:

$$P_{00} = 4/5$$

$$P_{10} = 1/5$$

$$I = 2P_{10} = 2/5$$

2. Second column: $\varepsilon_1 + U > \Phi > \varepsilon_2$



The non-zero transition rates (at zero T) are:

$$k_{00 \rightarrow 10}^T = |c_{11}|^2$$

$$k_{00 \rightarrow 01}^T = |c_{12}|^2$$

$$k_{10 \rightarrow 00}^S = (c_{11} + c_{21})^2$$

$$k_{01 \rightarrow 00}^S = (c_{12} + c_{22})^2$$

$$\frac{dP_{00}}{dt} = k_{01 \rightarrow 00}^S P_{01} + k_{10 \rightarrow 00}^S P_{10} - (k_{00 \rightarrow 10}^T + k_{00 \rightarrow 01}^T) P_{00} = 0$$

$$\frac{dP_{10}}{dt} = -k_{10 \rightarrow 00}^S P_{10} + k_{00 \rightarrow 10}^T P_{00} = 0$$

$$P_{00} + P_{10} + P_{01} = 1$$

$$I = (k_{00 \rightarrow 10}^T + k_{00 \rightarrow 01}^T) P_{00}$$

In the symmetric case:

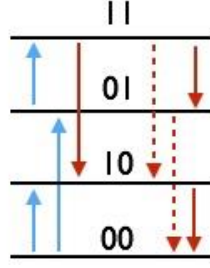
$$P_{00} = 0$$

$$P_{10} = 0$$

$$P_{01} = 1$$

$$I = \left(\frac{1}{2} + \frac{1}{2}\right) \cdot 0 = 0$$

3. Third column: $\varepsilon_2 + U > \Phi > \varepsilon_1 + U$



The non-zero transition rates (at zero T) are:

$$k_{00 \rightarrow 10}^T = |c_{11}|^2$$

$$k_{00 \rightarrow 01}^T = |c_{12}|^2$$

$$k_{01 \rightarrow 11}^T = |c_{11}|^2$$

$$k_{11 \rightarrow 10}^T = |c_{12}|^2$$

$$k_{11 \rightarrow 01}^S = (c_{11} + c_{21})^2$$

$$k_{11 \rightarrow 10}^S = (c_{12} + c_{22})^2$$

$$k_{10 \rightarrow 00}^S = (c_{11} + c_{21})^2$$

$$k_{01 \rightarrow 00}^S = (c_{12} + c_{22})^2$$

Rates and Probability equations:

$$\frac{dP_{00}}{dt} = k_{01 \rightarrow 00}^S P_{01} + k_{10 \rightarrow 00}^S P_{10} - (k_{00 \rightarrow 10}^T + k_{00 \rightarrow 01}^T) P_{00} = 0$$

$$\frac{dP_{10}}{dt} = -k_{10 \rightarrow 00}^S P_{10} + k_{00 \rightarrow 10}^T P_{00} + (k_{11 \rightarrow 10}^S + k_{11 \rightarrow 10}^T) P_{11} = 0$$

$$\frac{dP_{11}}{dt} = k_{01 \rightarrow 11}^T P_{01} - (k_{11 \rightarrow 01}^S + k_{11 \rightarrow 10}^S + k_{11 \rightarrow 10}^T) P_{11} = 0$$

$$P_{00} + P_{10} + P_{01} + P_{11} = 1$$

$$\begin{pmatrix} -(k_{00 \rightarrow 10}^T + k_{00 \rightarrow 01}^T) & k_{10 \rightarrow 00}^S & k_{01 \rightarrow 00}^S & 0 \\ k_{00 \rightarrow 10}^T & -k_{10 \rightarrow 00}^S & 0 & k_{11 \rightarrow 10}^S + k_{11 \rightarrow 10}^T \\ 0 & 0 & k_{01 \rightarrow 11}^T & -(k_{11 \rightarrow 01}^S + k_{11 \rightarrow 10}^S + k_{11 \rightarrow 10}^T) \\ 1 & 1 & 1 & 1 \end{pmatrix} = \begin{pmatrix} P_{00} \\ P_{10} \\ P_{01} \\ P_{11} \end{pmatrix} = \begin{pmatrix} 0 \\ 0 \\ 0 \\ 1 \end{pmatrix}$$

$$\begin{pmatrix} -(c_{11}^2 + c_{12}^2) & (c_{11} + c_{21})^2 & (c_{12} + c_{22})^2 & 0 \\ c_{11}^2 & -(c_{11} + c_{21})^2 & 0 & (c_{12} + c_{22})^2 + c_{12}^2 \\ 0 & 0 & c_{11}^2 & -((c_{11} + c_{21})^2 + (c_{12} + c_{22})^2 + c_{12}^2) \\ 1 & 1 & 1 & 1 \end{pmatrix} = \begin{pmatrix} P_{00} \\ P_{10} \\ P_{01} \\ P_{11} \end{pmatrix} = \begin{pmatrix} 0 \\ 0 \\ 0 \\ 1 \end{pmatrix}$$

$$I = (k_{00 \rightarrow 10}^T + k_{00 \rightarrow 01}^T) P_{00} + k_{01 \rightarrow 11}^T P_{01} - k_{11 \rightarrow 10}^T P_{11}$$

In the symmetric case:

$$P_{00} = 1/3$$

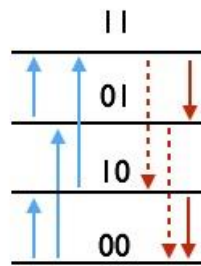
$$P_{10} = 1/15$$

$$P_{01} = 10/15$$

$$P_{11} = 2/15$$

$$I = \left(\frac{1}{2} + \frac{1}{2}\right) \cdot \frac{2}{15} + \frac{1}{2} \cdot \frac{10}{15} - \frac{1}{2} \cdot \frac{2}{15} = \frac{2}{5}$$

4. Forth column: $\Phi > \varepsilon_2 + U$



The non-zero transition rates (at zero T) are:

$$k_{00 \rightarrow 10}^T = |c_{11}|^2$$

$$k_{00 \rightarrow 01}^T = |c_{12}|^2$$

$$k_{01 \rightarrow 11}^T = |c_{11}|^2$$

$$k_{10 \rightarrow 11}^T = |c_{12}|^2$$

$$k_{11 \rightarrow 01}^S = (c_{11} + c_{21})^2$$

$$k_{11 \rightarrow 10}^S = (c_{12} + c_{22})^2$$

$$k_{10 \rightarrow 00}^S = (c_{11} + c_{21})^2$$

$$k_{01 \rightarrow 00}^S = (c_{12} + c_{22})^2$$

Rates and Probability equations:

$$\frac{dP_{00}}{dt} = k_{01 \rightarrow 00}^S P_{01} + k_{10 \rightarrow 00}^S P_{10} - (k_{00 \rightarrow 10}^T + k_{00 \rightarrow 01}^T) P_{00} = 0$$

$$\frac{dP_{10}}{dt} = -(k_{10 \rightarrow 00}^S + k_{10 \rightarrow 11}^S) P_{10} + k_{00 \rightarrow 10}^T P_{00} + k_{11 \rightarrow 10}^S P_{11} = 0$$

$$\frac{dP_{11}}{dt} = k_{01 \rightarrow 11}^T P_{01} + k_{10 \rightarrow 11}^T P_{10} - (k_{11 \rightarrow 01}^S + k_{11 \rightarrow 10}^S) P_{11} = 0$$

$$P_{00} + P_{10} + P_{01} + P_{11} = 1$$

$$\begin{pmatrix} -(k_{00 \rightarrow 10}^T + k_{00 \rightarrow 01}^T) & k_{10 \rightarrow 00}^S & k_{01 \rightarrow 00}^S & 0 \\ k_{00 \rightarrow 10}^T & -(k_{10 \rightarrow 00}^S + k_{10 \rightarrow 11}^T) & 0 & k_{11 \rightarrow 10}^S \\ 0 & k_{10 \rightarrow 11}^T & k_{01 \rightarrow 11}^T & -(k_{11 \rightarrow 01}^S + k_{11 \rightarrow 10}^S) \\ 1 & 1 & 1 & 1 \end{pmatrix} = \begin{pmatrix} P_{00} \\ P_{10} \\ P_{01} \\ P_{11} \end{pmatrix} = \begin{pmatrix} 0 \\ 0 \\ 0 \\ 1 \end{pmatrix}$$

$$\begin{pmatrix} -(c_{11}^2 + c_{12}^2) & (c_{11} + c_{21})^2 & (c_{12} + c_{22})^2 & 0 \\ c_{11}^2 & -(c_{11} + c_{21})^2 - c_{12}^2 & 0 & (c_{12} + c_{22})^2 \\ 0 & c_{12}^2 & c_{11}^2 & -(c_{11} + c_{21})^2 - (c_{12} + c_{22})^2 \\ 1 & 1 & 1 & 1 \end{pmatrix} = \begin{pmatrix} P_{00} \\ P_{10} \\ P_{01} \\ P_{11} \end{pmatrix} = \begin{pmatrix} 0 \\ 0 \\ 0 \\ 1 \end{pmatrix}$$

$$I = (k_{00 \rightarrow 10}^T + k_{00 \rightarrow 01}^T) P_{00} + k_{01 \rightarrow 11}^T P_{01} + k_{10 \rightarrow 11}^T P_{10}$$

In the symmetric case:

$$P_{00} = 0$$

$$P_{10} = 0$$

$$P_{01} = 4/5$$

$$P_{11} = 1/5$$

$$I = \left(\frac{1}{2} + \frac{1}{2}\right) \cdot 0 + \frac{1}{2} \cdot \frac{4}{5} + \frac{1}{2} \cdot 0 = \frac{2}{5}$$

Bibliography

- [1] R. Dingle, W. Wiegmann, and C. H. Henry. Quantum states of confined carriers in very thin $\text{al}_x\text{ga}_{1-x}\text{As-gaas-al}_x\text{ga}_{1-x}\text{As}$ heterostructures. *Phys. Rev. Lett.*, 33:827–830, Sep 1974.
- [2] P. M. Petroff, A. C. Gossard, R. A. Logan, and W. Wiegmann. Toward quantum well wires: Fabrication and optical properties. *Applied Physics Letters*, 41(7):635–638, 1982.
- [3] A.C. Gossard. Growth of microstructures by molecular beam epitaxy. *Quantum Electronics, IEEE Journal of*, 22(9):1649–1655, Sep 1986.
- [4] A. I. Ekimov and A. A. Onushchenko. Quantum size effect in three-dimensional microscopic semiconductor crystals. *Soviet Journal of Experimental and Theoretical Physics Letters*, 34:345, September 1981.
- [5] Suresh S. Growth of microstructures by molecular beam epitaxy. *Nanoscience and Nanotechnology*, 3(3):62–74, 2013.
- [6] R. Rossetti, S. Nakahara, and L. E. Brus. Quantum size effects in the redox potentials, resonance raman spectra, and electronic spectra of cds crystallites in aqueous solution. *The Journal of Chemical Physics*, 79(2):1086–1088, 1983.
- [7] P. Michler. *Single Quantum Dots: Fundamentals, Applications and New Concepts*. Physics and Astronomy Online Library. Springer, 2003.
- [8] C. B. Murray, D. J. Norris, and M. G. Bawendi. Synthesis and characterization of nearly monodisperse cde (e = sulfur, selenium, tellurium) semiconductor nanocrystallites. *Journal of the American Chemical Society*, 115(19):8706–8715, 1993.

-
- [9] Jin Young Kim, Oleksandr Voznyy, David Zhitomirsky, and Edward H. Sargent. 25th anniversary article: Colloidal quantum dot materials and devices: A quarter-century of advances. *Advanced Materials*, 25(36):4986–5010, 2013.
- [10] Yadong Yin and A. Paul Alivisatos. Colloidal nanocrystal synthesis and the organic-inorganic interface. *Nature*, 437:664–670, 2005.
- [11] Karin Overgaag, Peter Liljeroth, Bruno Grandidier, and Daniel Vanmaekelbergh. Scanning tunneling spectroscopy of individual pbse quantum dots and molecular aggregates stabilized in an inert nanocrystal matrix. *ACS Nano*, 2(3):600–606, 2008.
- [12] Octavi E. Semonin, Joseph M. Luther, and Matthew C. Beard. Quantum dots for next-generation photovoltaics. *Materials Today*, 15(11):508 – 515, 2012.
- [13] Varun K A Sreenivasan, Andrei V Zvyagin, and Ewa M Goldys. Luminescent nanoparticles and their applications in the life sciences. *Journal of Physics: Condensed Matter*, 25(19):194101, 2013.
- [14] Dmitri V. Talapin, Jong-Soo Lee, Maksym V. Kovalenko, and Elena V. Shevchenko. Prospects of colloidal nanocrystals for electronic and optoelectronic applications. *Chemical Reviews*, 110(1):389–458, 2010.
- [15] Jiang Tang, Kyle W. Kemp, Sjoerd Hoogland, and Edward H. Sargent. Colloidal-quantum-dot photovoltaics using atomic-ligand passivation. *Nature Materials*, 10:765–771, 2011.
- [16] Alexander H. Ip, Susanna M. Thon, Sjoerd Hoogland, and Edward H. Sargent. Hybrid passivated colloidal quantum dot solids. *Nature Nanotechnology*, 7:577–582, 2012.
- [17] Vanmaekelbergh, Daniel, and Peter Liljeroth. Electron-conducting quantum dot solids: novel materials based on colloidal semiconductor nanocrystals. *Chem. Soc. Rev.*, 34:299–312, 2005.
- [18] T. M. Inerbaev, A. E. Masunov, S. I. Khondaker, A. Dobrinescu, A. V. Plamada, and Y. J. Kawazoe. Quantum chemistry of quantum dots: Effects of ligands and oxidation. *The Journal of Chemical Physics*, 131(4), 2009.

- [19] Adam J. Morris-Cohen, Micha Malicki, Mark D. Peterson, John W. J. Slavin, and Emily A. Weiss. Chemical, structural, and quantitative analysis of the ligand shells of colloidal quantum dots. *Chemistry of Materials*, 25(8):1155–1165, 2013.
- [20] Clive R. Bealing, William J. Baumgardner, Joshua J. Choi, Tobias Hanrath, and Richard G. Hennig. Predicting nanocrystal shape through consideration of surface-ligand interactions. *ACS Nano*, 6(3):2118–2127, 2012.
- [21] E. V. Shevchenko, D. V. Talapin, N. A. Kotov, S. O’Brien, and C. B. Murray. Structural diversity in binary nanoparticle superlattices. *Nature*, 439:55–59, 2006.
- [22] Jonas Nyvold Pedersen, Benny Lassen, Andreas Wacker, and Matthias H. Hettler. Coherent transport through an interacting double quantum dot: Beyond sequential tunneling. *Phys. Rev. B*, 75:235314, Jun 2007.
- [23] A. J. Nozik, M. C. Beard, J. M. Luther, M. Law, R. J. Ellingson, and J. C. Johnson. Semiconductor quantum dots and quantum dot arrays and applications of multiple exciton generation to third-generation photovoltaic solar cells. *Chemical Reviews*, 110(11):6873–6890, 2010.
- [24] D. Aaron R. Barkhouse, Ratan Debnath, Illan J. Kramer, David Zhitomirsky, Andras G. Pattantyus-Abraham, Larissa Levina, Lioz Etgar, Michael Gretzel, and Edward H. Sargent. Depleted bulk heterojunction colloidal quantum dot photovoltaics. *Advanced Materials*, 23(28):3134–3138, 2011.
- [25] Prashant V. Kamat. Quantum dot solar cells. semiconductor nanocrystals as light harvesters. *The Journal of Physical Chemistry C*, 112(48):18737–18753, 2008.
- [26] K.-S. Cho, E. K. Lee, W.-J. Joo, E. Jang, T.-H. Kim, S. J. Lee, S. J. Kwon, J. Y. Han, B.-K. Kim, B. L. Choi, and J. M. Kim. High-performance crosslinked colloidal quantum-dot light-emitting diodes. *Nat. Photonics*, 3:341–345, 2009.
- [27] J. M. Caruge, J. E.; Halpert, V. Wood, V. Bulovic, and M. G. Bawendi. Colloidal quantum-dot light-emitting diodes with metal-oxide charge transport layers. *Nat. Photonics*, 2:247 – 250, 2008.
- [28] H. S. Borges, L. Sanz, J. M. Villas-Bôas, and A. M. Alcalde. Robust states in semiconductor quantum dot molecules. *Phys. Rev. B*, 81:075322, Feb 2010.

- [29] Miguel Ibáñez Berganza, Alberto Petri, and Pietro Coletti. Dynamic metastability in the two-dimensional potts ferromagnet. *Phys. Rev. E*, 89:052115, May 2014.
- [30] E. A. Stinaff, M. Scheibner, A. S. Bracker, I. V. Ponomarev, V. L. Korenev, M. E. Ware, M. F. Doty, T. L. Reinecke, and D. Gammon. Optical signatures of coupled quantum dots. *Science*, 311(5761):636–639, 2006.
- [31] Danny Kim, Samuel G. Carter, Alex Greulich, Allan S. Bracker, and Daniel Gammon. Ultrafast optical control of entanglement between two quantum-dot spins. *Nature Physics*, 7(3):229, 2011/03//print.
- [32] Dmitri V. Talapin and Christopher B. Murray. Pbse nanocrystal solids for n- and p-channel thin film field-effect transistors. *Science*, 310(5745):86–89, 2005.
- [33] Frederik Hetsch, Ni Zhao, Stephen V. Kershaw, and Andrey L. Rogach. Quantum dot field effect transistors. *Materials Today*, 16(9):312 – 325, 2013.
- [34] Valerio Adinolfi, Illan J. Kramer, Andr J. Labelle, Brandon R. Sutherland, S. Hoogland, and Edward H. Sargent. Photojunction field-effect transistor based on a colloidal quantum dot absorber channel layer. *ACS Nano*, 9(1):356–362, 2015.
- [35] Uri Banin and Oded Millo. Tunneling and optical spectroscopy of semiconductor nanocrystals. *Annual Review of Physical Chemistry*, 54(1):465–492, 2003.
- [36] Oded Millo, David Katz, YunWei Cao, and Uri Banin. Scanning tunneling spectroscopy of inas nanocrystal quantum dots. *Phys. Rev. B*, 61:16773–16777, Jun 2000.
- [37] Peter Liljeroth, Pedro A. Zeijlmans van Emmichoven, Stephen G. Hickey, Horst Weller, Bruno Grandidier, Guy Allan, and Daniël Vanmaekelbergh. Density of states measured by scanning-tunneling spectroscopy sheds new light on the optical transitions in pbse nanocrystals. *Phys. Rev. Lett.*, 95:086801, Aug 2005.
- [38] Peter Liljeroth, Lucian Jdira, Karin Overgaag, Bruno Grandidier, Sylvia Speller, and Daniel Vanmaekelbergh. Can scanning tunnelling spectroscopy measure the density of states of semiconductor quantum dots? *Phys. Chem. Chem. Phys.*, 8:3845–3850, 2006.
- [39] T. H. Nguyen, J. Habinshuti, Y. Justo, R. Gomes, G. Mahieu, S. Godey, J. P. Nys, S. Carrillo, Z. Hens, O. Robbe, S. Turrell, and B. Grandidier. Charge carrier

- identification in tunneling spectroscopy of core-shell nanocrystals. *Phys. Rev. B*, 84:195133, Nov 2011.
- [40] G. A. Grinbom, M. Saraf, C. Saguy, A. C. Bartnik, F. Wise, and E. Lifshitz. Density of states in a single pbse/pbs core-shell quantum dot measured by scanning tunneling spectroscopy. *Phys. Rev. B*, 81:245301, Jun 2010.
- [41] S. Vortman, O. Ben-dor, S. Yochelis, Y. Amit, and Y. Paltiel. Mapping the energy band structure of nanocrystal monolayers under ambient conditions. *The Journal of Physical Chemistry C*, 117(43):22245–22249, 2013.
- [42] B.I. Sklovskij, B.I. Shklovski, and A.L. Efros. *Electronic Properties of Doped Semiconductors*. Springer series in solid-state sciences. Springer London, Limited, 1984.
- [43] Amir Zabet-Khosousi and Al-Amin Dhirani. Charge transport in nanoparticle assemblies. *Chemical Reviews*, 108(10):4072–4124, 2008.
- [44] Dong Yu, Congjun Wang, Brian L. Wehrenberg, and Philippe Guyot-Sionnest. Variable range hopping conduction in semiconductor nanocrystal solids. *Phys. Rev. Lett.*, 92:216802, May 2004.
- [45] Dong Yu, Brian L. Wehrenberg, Praket Jha, Jiasen Ma, and Philippe Guyot-Sionnest. Electronic transport of n-type cdse quantum dot films: Effect of film treatment. *Journal of Applied Physics*, 99(10):–, 2006.
- [46] W. G. van der Wiel, S. De Franceschi, J. M. Elzerman, T. Fujisawa, S. Tarucha, and L. P. Kouwenhoven. Electron transport through double quantum dots. *Rev. Mod. Phys.*, 75:1–22, Dec 2002.
- [47] J. Fransson. Theory of current-voltage asymmetries in double quantum dots. *Phys. Rev. B*, 69:201304, May 2004.
- [48] R. Härtle, G. Cohen, D. R. Reichman, and A. J. Millis. Decoherence and lead-induced interdot coupling in nonequilibrium electron transport through interacting quantum dots: A hierarchical quantum master equation approach. *Phys. Rev. B*, 88:235426, Dec 2013.
- [49] B. Michaelis, C. Emary, and C. W. J. Beenakker. All-electronic coherent population trapping in quantum dots. *EPL (Europhysics Letters)*, 73(5):677, 2006.

-
- [50] P. Schijven and O. Mülken. Avoiding dark states in open quantum systems by tailored initializations. *Phys. Rev. E*, 85:062102, Jun 2012.
- [51] T. Brandes and F. Renzoni. Current switch by coherent trapping of electrons in quantum dots. *Phys. Rev. Lett.*, 85:4148–4151, Nov 2000.
- [52] Clive Emary. Dark states in the magnetotransport through triple quantum dots. *Phys. Rev. B*, 76:245319, Dec 2007.
- [53] I. Weymann, B. R. Buřka, and J. Barnaś. Dark states in transport through triple quantum dots: The role of cotunneling. *Phys. Rev. B*, 83:195302, May 2011.
- [54] C Emary. Dark-states in multi-mode multi-atom jaynes, cummings systems. *Journal of Physics B: Atomic, Molecular and Optical Physics*, 46(22):224008, 2013.
- [55] Jonas Nyvold Pedersen, Benny Lassen, Andreas Wacker, and Matthias H. Hettler. Coherent transport through an interacting double quantum dot: Beyond sequential tunneling. *Phys. Rev. B*, 75:235314, Jun 2007.
- [56] Roni Pozner, Efrat Lifshitz, and Uri Peskin. Negative differential resistance probe for interdot interactions in a double quantum dot array. *The Journal of Physical Chemistry Letters*, 6(9):1521–1528, 2015.
- [57] C. Livermore, C. H. Crouch, R. M. Westervelt, K. L. Campman, and A. C. Gossard. The coulomb blockade in coupled quantum dots. *Science*, 274(5291):1332–1335, 1996.
- [58] K. A. Matveev, L. I. Glazman, and H. U. Baranger. Coulomb blockade of tunneling through a double quantum dot. *Phys. Rev. B*, 54:5637–5646, Aug 1996.
- [59] S. Sapmaz, P. Jarillo-Herrero, Ya. M. Blanter, C. Dekker, and H. S. J. van der Zant. Tunneling in suspended carbon nanotubes assisted by longitudinal phonons. *Phys. Rev. Lett.*, 96:026801, Jan 2006.
- [60] Renaud Leturcq, Christoph Stampfer, Kevin Inderbitzin, Lukas Durrer, Christofer Hierold, Eros Mariani, Maximilian G. Schultz, Felix von Oppen, and Klaus Ensslin. Franck-CONDON blockade in suspended carbon nanotube quantum dots. *Nat Phys*, 5(5):327 – 331, 2009.

- [61] Bent Weber, , TanY. H. Matthias, Suddhasatta Mahapatra, Thomas F. Watson, Hoon Ryu, Rajib Rahman, HollenbergLloyd C. L., Gerhard Klimeck, and Michelle Y Simmons. Spin blockade and exchange in coulomb-confined silicon double quantum dots. *Nature Nano*, 9(6):430–435, 2014.
- [62] Jesús Iñarrea, Gloria Platero, and Allan H. MacDonald. Electronic transport through a double quantum dot in the spin-blockade regime: Theoretical models. *Phys. Rev. B*, 76:085329, Aug 2007.
- [63] S. Amaha, W. Izumida, T. Hatano, S. Tarucha, K. Kono, and K. Ono. Spin blockade in a double quantum dot containing three electrons. *Phys. Rev. B*, 89:085302, Feb 2014.
- [64] M. Grobis. *Kondo Effect in Mesoscopic Quantum Dot*. Handbook of Magnetism and Advanced Magnetic Materials. Wiley, 2007.
- [65] A M Chang and J C Chen. The kondo effect in coupled-quantum dots. *Reports on Progress in Physics*, 72(9):096501, 2009.
- [66] Sara M. Cronenwett, Tjerk H. Oosterkamp, and Leo P. Kouwenhoven. A tunable kondo effect in quantum dots. *Science*, 281(5376):540–544, 1998.
- [67] L.I. Glazman and M. Pustilnik. Coulomb blockade and kondo effect in quantum dots. In R. Fazio, V.F. Gantmakher, and Y. Imry, editors, *New Directions in Mesoscopic Physics (Towards Nanoscience)*, volume 125 of *NATO Science Series*, pages 93–115. Springer Netherlands, 2003.
- [68] Roni Pozner, Efrat Lifshitz, and Uri Peskin. Charge transport-induced recoil and dissociation in double quantum dots. *Nano Letters*, 14(11):6244–6249, 2014.
- [69] Uri Peskin. An introduction to the formulation of steady-state transport through molecular junctions. *Journal of Physics B: Atomic, Molecular and Optical Physics*, 43(15):153001, 2010.
- [70] H.P. Breuer and F. Petruccione. *The Theory of Open Quantum Systems*. Oxford University Press, 2002.
- [71] A. Nitzan. *Chemical Dynamics in Condensed Phases : Relaxation, Transfer and Reactions in Condensed Molecular Systems: Relaxation, Transfer and Reactions in Condensed Molecular Systems*. Oxford Graduate Texts. OUP Oxford, 2006.

-
- [72] W. Attila Szabo and W. Neil S Ostlund. *Modern quantum chemistry: introduction to advanced electronic structure theory*. Courier Corporation, 1989.
- [73] F. R. Waugh, M. J. Berry, D. J. Mar, R. M. Westervelt, K. L. Campman, and A. C. Gossard. Single-electron charging in double and triple quantum dots with tunable coupling. *Phys. Rev. Lett.*, 75:705–708, Jul 1995.
- [74] Hugo E. Romero and Marija Drndic. Coulomb blockade and hopping conduction in pbse quantum dots. *Phys. Rev. Lett.*, 95:156801, Oct 2005.
- [75] Roman Vaxenburg and Efrat Lifshitz. Alloy and heterostructure architectures as promising tools for controlling electronic properties of semiconductor quantum dots. *Phys. Rev. B*, 85:075304, Feb 2012.
- [76] A.L. Éfros, D.J. Lockwood, and L. Tsybeskov. *Semiconductor Nanocrystals: From Basic Principles to Applications*. Nanostructure Science and Technology. Springer, 2003.
- [77] R. Härtle, G. Cohen, D. R. Reichman, and A. J. Millis. Decoherence and lead-induced interdot coupling in nonequilibrium electron transport through interacting quantum dots: A hierarchical quantum master equation approach. *Phys. Rev. B*, 88:235426, Dec 2013.

נמצא כי האפקט המכני תלוי במידת האסימטריה וכן במיקום של מגע המיקרוסקופ (הנקודה הקוונטית אליה הוא מצומד).

בנוסף נמצאה הופעה של אפקט לא לינארי, התנגדות דיפרנציאלית שלילית (NDR) ייחודית, המיוחסת להתאבכות הורסת בעת העברת מטען מצמד הנקודות הקוונטיות אל האלקטרודה שעל פני השטח. ההתאבכות ההורסת נגמרת בשל טעינה של אורביטל בלתי-קושר אשר בתורו יוצר חסימה של תנועת אלקטרונים דרך צמד הנקודות הקוונטיות בשל כוחות קולון דוחים ועמו ירידה חדה ואיפוס של הזרם הנמדד. האפקט הלא לינארי יכול לספק מידע על האינטראקציה האלקטרונית בין שתי הנקודות הקוונטיות הסמוכות על ידי מדידה של אות ה-NDR.

לבסוף מוצג רעיון חדשני של התקן זיכרון בלתי נדיף ננו-אלקטרו-מכאני אשר משלב אשכול של שלוש נקודות קוונטיות. פעולת ההתקן מבוססת על תנועה של נקודה קוונטית צפה (FQD) אשר ממוקמת בין שתי נקודות קוונטיות קשורות (BQD). יכולת התנועה המכנית של הנקודה הצפה משמשת למעבר בין שתי מצבי פעולה יציבים, מצב "ON" ומצב "OFF". הכוחות המכניים האפקטיביים בין הנקודות הקוונטיות, אשר מושרים על ידי השרשראות המולקולריות, בין הנקודות הקשורות והנקודה הצפה, משרתים להחזקת הנקודה הצפה במקום בכל מצב יציב תחת אפס מתח. בהתחשב בפרמטרים מיקרוסקופיים מציאותיים, הטיפול התיאורטי שלנו של האשכול חושף את המאפיינים של ההתקן. התכונות האלקטרוניות הניתנות לכוונון של הנקודות הקוונטיות וכן היכולת לביצוע מניפולציות על השרשראות המולקולריות אשר מקיפות את הנקודות הקוונטיות הן המפתח למימוש התקן העובד כהלכה. לסיום, תדירות הפעולה של התקן זה מוערכת להיות גבוהה יותר בהשוואה להתקני זיכרון בלתי נדיפים נוכחיים (התקני פלאש) ובנוסף להתקן יש פוטנציאל להציג מספר יתרונות מרכזיים אחרים, בכלל זה אפס דליפת זרם במצב יציב, אפס היסטריזיס (חֶשֶׁל) וכן יכולת אופטימיזציה של מתח המיתוג והיחס בין זרמי ה-ON וה-OFF.

תקציר

נקודות קוונטיות קולואידיות (CQDs) הינן מבנים ננומטרים חופשיים, המוקפים בשרשראות מולקולריות אורגניות (ligands), עם מאפיינים אלקטרוניים הניתנים לכוונון על ידי שינויים כימיים וכן שינויי גודל וצורה של הנקודות הקוונטיות עצמן. המאפיינים של נקודה קוונטית בודדת והמידה שבה אינטראקציות חשמליות ומכאניות בין נקודות קוונטיות במערך הן משמעותיות ביחס למאפייני ההולכה הנמדדים הם בעלי חשיבות עליונה. אולם קשה להעריך את האינטראקציות האלה בגלל האופן שבו הם נשלטות על ידי הכימיה של פני השטח ובשל השרשראות המולקולריות המקשרות בין נקודות קוונטיות נפרדות. עד כה רק מחקרים מעטים לקחו בחשבון את המבנה ברמה האטומית של השרשראות המולקולריות וההשפעה שלהם על הכוחות המכאניים בין הנקודות הקוונטיות עדיין לא נלקחה בחשבון עד כה.

בעבודה זו, אנו שוקלים התקן חדש המבוסס על מגע של מיקרוסקופ מנהור סורק (STM) - שתי נקודות קוונטיות מצומדות (DQD) - ומשטח תחתון, לשם מדידת הכוחות האפקטיביים בין הנקודות הקוונטיות אשר מושרים באמצעותן של השרשראות המולקולריות, לשם יצירת תנועה של נקודה קוונטית בודדת בתוך מערך של נקודות קוונטיות וכן לשם חקירת הקישוריות הייחודית בהתקן זה אשר מבוססת על מגע STM אשר מצומד לנקודה קוונטית בודדת בעוד הצימוד אל פני השטח משותף לשני הנקודות הקוונטיות.

הצימוד האלקטרו-מכני בין הנקודות הקוונטיות טופל על ידי התחשבות באופן מפורש בתלות של הביטויים האלקטרוניים על המרחק בין הנקודות הקוונטיות. באופן ספציפי, הצימוד של האלקטרון הבודד (מנהור) ואינטראקציות רבות אלקטרוניים (כוחות Coulomb ו-Exchange) חושבו באופן עקבי עם התגובה המכנית של המרחק בין הנקודות תוך כדי שימוש בניסוח מטריציאלי מצומצם קוונטי-קלאסי (mixed quantum-classical reduced density matrix formulation). ערכים אופייניים של מסות של נקודות קוונטיות והערכים שנבחרו כקבועי הכוח של השרשראות מולקולריות אפשרו לטפל בתנועה המכנית על ידי שימוש במכניקה קלאסית.

הצימוד בין הנקודות הקוונטיות למגעים של מיקרוסקופ המנהור הינו חלש וזאת בהתבסס על ערכים אופייניים של מחסומי מנהור במודלים של STM. בנוסף המגעים שומרים על "קוואזי" צפיפות שיווי משקל, בזמן שמערכת הנקודות הקוונטית הרב-אלקטרונית מתפתחת בהתאם למשוואת Liouville בסדר שני בצימוד למגעים.

התגובה במצב יציב של המערכת למתח המופעל בין המגעים של מיקרוסקופ המנהור נמצאה באמצעות פתרון של המשוואות הדינמיות המצומדות למשוואות אלקטרו-מכאנית תחת האילוץ של אפס מהירות ואפס תאוצה במצב יציב.

הניתוח התיאורטי של מבנה ה-DQD בהתקן חושף בפעם הראשונה יצירה של רתיעה מכנית וכן ניתוק של צמד הנקודות הקוונטיות (מעבר מצמד נקודות קוונטיות לנקודה קוונטית בודדת) אשר מושרה על ידי הפעלת מתח וכן מלווה בשינויים בולטים בזרם. על ידי התחשבות בפרמטרים מיקרוסקופיים מציאותיים. הגישה שלנו מאפשרת מציאת מתאם בין ההופעה של התנועה המכאנית תחת הפעלת מתח עם הכוחות המכניים האפקטיביים שמושרים על ידי השרשראות המולקולריות. הפוטנציאל המכני הקושר בין הנקודות ממודל באמצעות פונקציות פוטנציאלי מורס גנריות עם פרמטרים ששולטים במעבר מצימוד "חלש" ל-"חזק". פוטנציאל המורס מאפשר לשקף את כוחות הדחייה קצרי הטווח וכוחות המשיכה ארוכי הטווח של הכוח המושרה בין הנקודות הקוונטיות בשל השרשראות המולקולריות. מאפיין חשוב נוסף הינו התלות בסימטריה בין הנקודות. הבדל הסימטריה בין הנקודות בא לידי ביטוי באנרגיות LUMO שונות, אותן ניתן להשיג על ידי שימוש בנקודות קוונטיות קולואידיות בעלות גדלים והרכבים כימיים שונים.

המחקר נעשה בהנחייתם של פרופ' אפרת ליפשיץ ופרופ' אורי פסקין בפקולטה לכימיה ע"ש שולך בטכניון.

אני מודה לטכניון על התמיכה הכספית הנדיבה במהלך השתלמותי.

**מידול תופעות המושרות ע"י העברת מטען דרך צמדי
נקודות קוונטיות קולואידיות, ופיתוח גישות חדשות
לאפיון האינטראקציות ביניהן**

חיבור על מחקר לשם מילוי חלקי של הדרישות לקבלת התואר
דוקטור לפילוסופיה

רוני פוזנר

הוגש לסנט הטכניון – מכון טכנולוגי לישראל

ינואר 2016

חיפה

טבת תשע"ו

**מידול תופעות המושרות ע"י העברת מטען דרך צמדי
נקודות קוונטיות קולואידיות, ופיתוח גישות חדשות
לאפיון האינטראקציות ביניהן**

רוני פוזנר